Molecular Basis of Plasticity of Porcine Delta Coronavirus (PDCoV) & Development of Countermeasures Against Infection

Megi Rexhepaj

A dissertation
submitted in partial fulfillment of the
requirements for the degree of

Doctor of Philosophy

University of Washington
2024

Reading Committee:
Justin M. Kollman
Suzanne Hoppins
James B Hurley

Program Authorized to Offer Degree:
Biochemistry

University of Washington

Abstract

Molecular Basis of Plasticity of Porcine Delta Coronavirus (PDCoV) & Development of Countermeasures Against Infection

Megi Rexhepaj

Chair of the Supervisory Committee:

Justin M. Kollman

Biochemistry

Porcine deltacoronavirus (PDCoV) is an enteric pathogen that infects a broad range of mammal and avian species. Viral entry is achieved through the transmembrane spike (S) glycoprotein, specifically the receptor binding domain (RBD), binding to host receptor aminopeptidase N (APN). The S glycoprotein plays a key role in modulating host and tissue tropism, zoonotic transmission, and pathogenesis. The mechanism by which the S glycoprotein binds to a broad range of host receptors is not understood. Given that the S glycoprotein is the main target of antibodies and that neutralizing antibody titers are a correlate of protection against coronaviruses, the development of vaccines and therapeutics focuses intensively on this glycoprotein target. This research describes the molecular basis of binding of the S glycoprotein to host receptors and identifies the neutralizing epitopes on the S glycoproteins providing the first line of protection for a possible future PDCoV epidemic.

Chapter 1: Background

Chapter 2: Molecular basis of binding and plasticity of the emerging PDCoV

Chapter 3: Identification of broadly neutralizing antibodies against PDCoV

Chapter 4: Development of countermeasures against emerging PDCoV

Chapter 1: Background

1.1. Coronaviruses

Coronaviruses (CoVs) are a diverse and vast class of enveloped positive-strand RNA viruses that cause mild to deadly respiratory and enteric diseases in avian and mammalian species. The viruses belong to the family *Coronavirdiae* which consists of two subfamilies *Letovirinae* and *Orthocoronavirinae*. Within the subfamily *Orthocoronavirinae* the viruses are split into four key genera: *Alpha-, Beta-, Gamma-, and Deltacoronavirus*. Viruses from three out of these four genera are known to infect humans: *Alpha-*, *Beta-*, *Deltacoronavirus*. *Alpha*-CoVs, 229E and NL63, along with *Beta-CoVs,* HKU1 and OC43, are endemic in humans and mainly associated with mild respiratory infections (common colds), although some cases lead to severe illness, particularly for children, the elderly and immunocompromised individuals. To date, all three highly pathogenic CoVs belong to the *Beta*-CoVs, namely SARS-CoV-1, MERS-CoV and SARS-CoV-2, causing a range from mild to severe illness leading to death. *Delta*-CoVs (DCoV), are enteric viruses that primarily infect porcine and wild birds causing diarrhea, vomiting, dehydration, and morbidity in piglets. In 2022, the first reported detection of DCoV, was found to infect children in Haiti causing undifferentiated febrile illness (samples were collected between 2014-2015). Interestingly, genomic analysis of the human DCoV strains in the three children clustered with independent PDCoV strains traced to US and Chinese origins, suggesting multiple zoonotic introduction events. The last member, *Gamma*-CoVs, are to date the only non-human pathogenic CoVs restricted to infecting only avian species and are responsible for causing a significant loss in poultry across the globe (Figure 1.1.1A) [1-15].

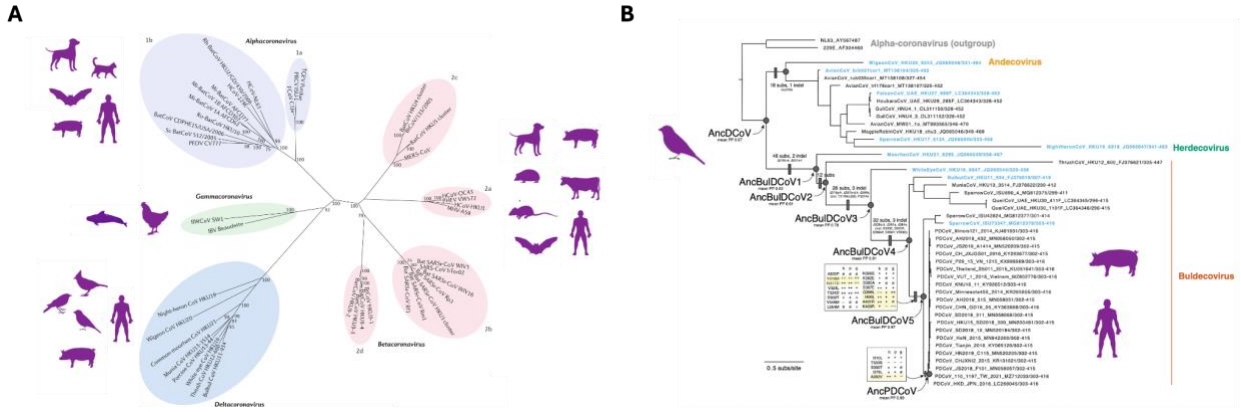

Figure 1.1.1. A, Four genera of the *Orthocoronavirinae* subfamily **B,** Phylogenetic tree of the DCoV genus

1.2. Delta-Coronaviruses

The DCoV genus is not well characterized and the origin of PDCoV is unknown. Phylogenetic analysis of DCoVs suggests that the virus closely matches with sparrow DCoV (SpDCoV) with >96% amino acid sequence identity using pairwise genome analysis suggesting cross-species transmission from birds to mammals (Figure 1.1.1B). In the late 2000s, the virus was identified in Hong Kong China in porcine and quickly spread and devasted the swine populations throughout the world. Interestingly, PDCoV continues to spread and evolve in porcine, with spillover into humans, as are the avian DCoVs. The most recent finding was pigeon DCoV detected in live poultry in the Shandong Province, China between 2022-2023. Sequence analysis of the S glycoprotein of pigeon DCoV indicates a high sequence similarity to the three human-origin PDCoV strains (88%) suggesting that the avian DCoVs could have the ability to infect mammals[16].

1.3. Viral entry and fusion

Viral entry is mediated through the S glycoprotein, a type I transmembrane viral fusion protein that decorates the viral envelope (Figure 1.3.1A). The S glycoprotein consists of a homotrimer with two subunits; N terminal S_1 subunit that binds the host receptor and C terminal S_2 subunit that contains the fusion machinery. The S_1 subunit is composed of two domains, the N-terminal domain (NTD) and the RBD. The S_2 subunit is composed of a helical bundle that makes up the S_2 core, the fusion peptide which inserts itself in the membrane, and the connector domain (Figure 1.3.1B) [17-20, 35].

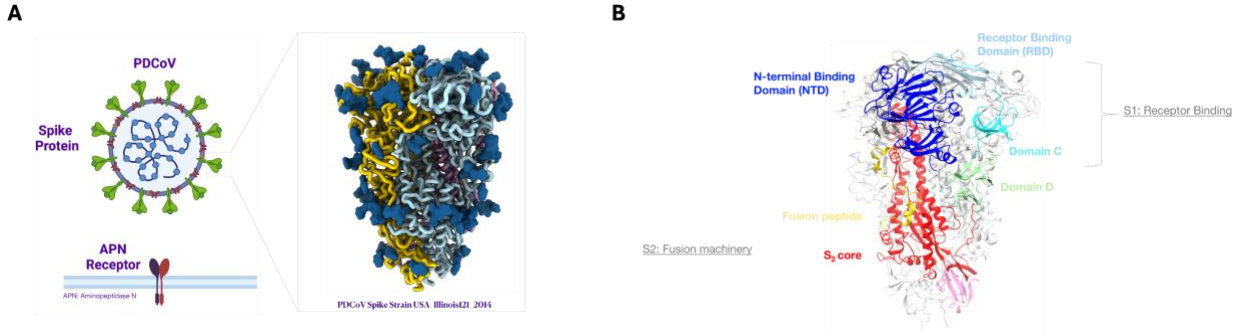

Figure 1.3.1. Spike glycoprotein A, Graphical overview of PDCoV and host APN receptor along with a cryo-EM structure of the S glycoprotein **B,** Structural view of the S glycoprotein and the organization of the domains for one of the homotrimers.

Viral entry is achieved through 1) binding of the RBD to the host APN receptor leading to conformational changes that expose the S_2' cleavage site upstream of the fusion peptide 2) proteolytic cleavage and activation 3) release of the S_1 subunit and liberation of the fusion peptide and S_2 core 4) drastic conformational changes of the S_2 core to form the post-fusion six-helical bundle with the fusion peptide flipped and propelled to the tip of the protein to allow for fusion of the host and viral membrane (Figure 1.3.2) [17-20, 35].

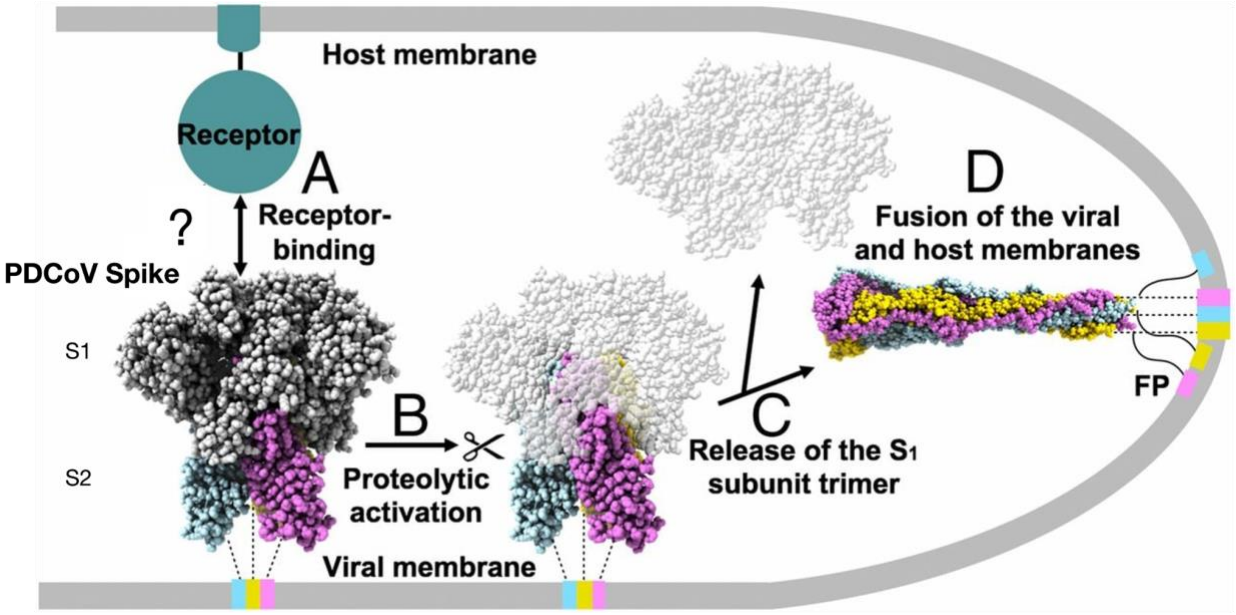

Figure 1.3.2. Schematic representation of CoV viral fusion

1.4. Development of countermeasures against infection

Given that the S glycoprotein is the major surface protein on the virus and key for viral fusion, it is under high selective pressure and a hot spot for mutations to build to escape immune recognition. Amongst the four other structural proteins of PDCoV, nucleocapsid (N), membrane (M), and envelope (E) proteins, the S glycoprotein is highly variable throughout PDCoV strains analyzed from 2004-2020, as the other three are relatively conserved. Despite CoVs all containing an S glycoprotein with a strictly conserved mechanism of fusion, there is a low sequence identity of 27-42% across the four genera (Figure 4). Inhibition of viral fusion through the development of broadly neutralizing antibodies against the fusion peptide led to limited breadth of neutralization across all four genera, as neutralization was only observed for *alpha* and *beta*-CoVs but not for *delta*-CoVs[21-26]. There is a need to develop countermeasures against this novel and newly emerging PDCoV as there are no FDA-approved vaccines or therapeutics for PDCoV nor any *delta*-CoVs.

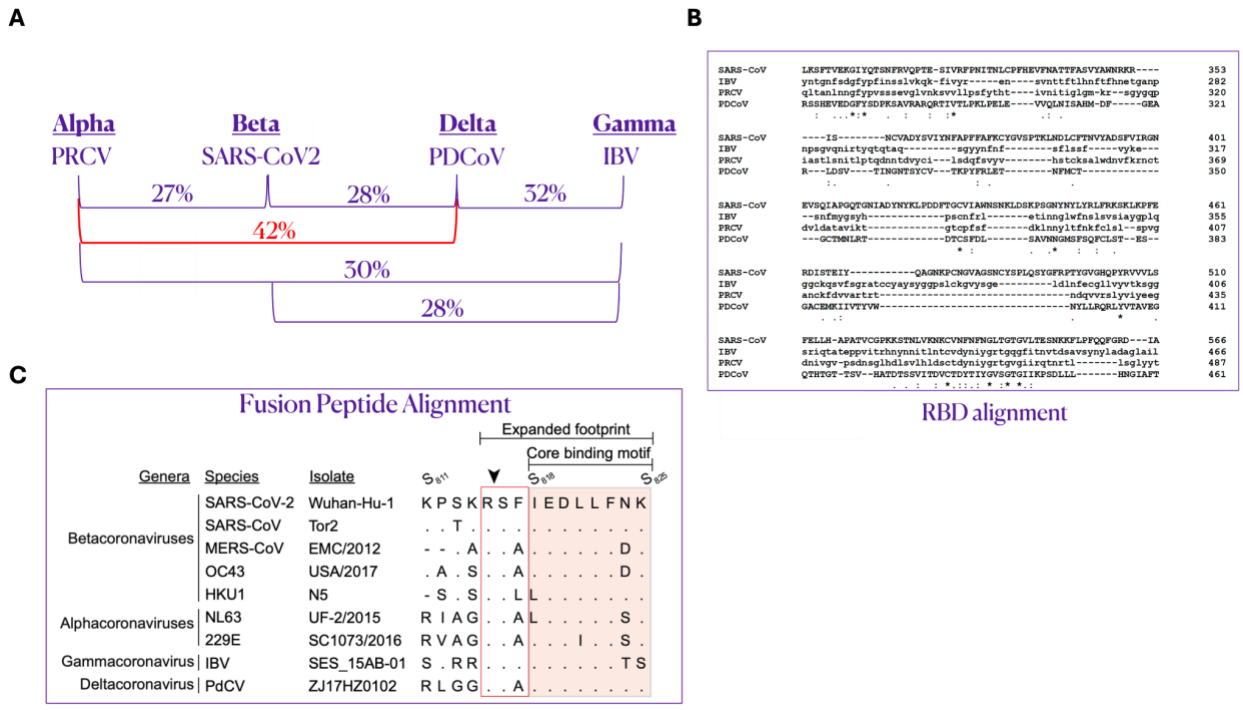

Figure 1.4.1 Analysis of CoV sequence identity A, Sequence identity matrix for the S glycoprotein across the four genera of CoV. **B,** RBD alignment for a representative virus from each of the four genera of CoVs. **C,** S glycoprotein fusion peptide alignment across representative viruses from each of the four genera of CoVs.

Chapter 2: Molecular basis of binding and plasticity of an emerging DCoV

2.1. Abstract

Coronaviruses (CoVs) belong to a diverse family of viruses containing four generas: *Alpha-*, *Beta -*, *Gamma – and Deltacoronavirus*. The four generas infect a wide host range spanning from mammals to birds causing respiratory or enteric disease. The *BetaCoV*, SARS-CoV-2, led to a worldwide pandemic in 2020, claiming the lives of 6,908,554 people. While a significant amount of work has been done on the two primary human infecting *Alpha*CoV and *Beta*CoV, less has been done on the newly emerging porcine *Delta*CoV (PDCoV). The virus was identified in Hong Kong in porcine in the late 2000s and since then has spread throughout the world infecting large masses of swine, leading to death in piglets. In 2022, PDCoV was detected in human children in Haiti causing acute undifferentiated febrile illness. There is no vaccine or treatment against PDCoV or any of the other viruses belonging to *Delta*CoV[1-16]. This study investigates the molecular mechanism of viral entry by the PDCoV Spike glycoprotein coating the surface of the virus. We report the cryo-EM structure of the receptor binding domain (RBD) bound to the host APN receptor and reveal a unique mechanism by which three binding loops are responsible for specificity and tropism. We reveal for the first time that host glycans are utilized by PDCoV to bind and enter host APN orthologs. Furthermore, we go on to demonstrate that the receptor binding interface of this virus is plastic but restricted in mutations.

2.2. Introduction

PDCoV can engage a diverse set of receptors from multiple species. Previous studies have shown the S glycoprotein and specifically the RBD from the S_1 subunit (Figure 1.3.1B) to bind to APN receptors from mammalian and avian origin[15-16]. However, it is not understood how this interaction occurs as there is no biochemical characterization of this interaction nor any structural information. For the goal of designing a vaccine against any new emerging virus understanding the mechanism of viral entry is fundamental to informing how to inhibit this interaction and effectively neutralize the virus. Cryo-EM structure of the apo S glycoprotein at 3.3 Å resolution reveals the fold and architecture but is unable to provide insight into the molecular mechanism of binding of the RBD to the host APN orthologs[15].

Here we report the first binding affinities and viral entry assessment of PDCoV to APN orthologs spanning mammalian and avian species; human (h), porcine (p), galline (g), munia (m), sparrow (s) and bulbul (b). Strikingly, while the virus was originally discovered in porcine, we found that it demonstrated a preference in binding to human and avian APN receptors over porcine APN. Using cryo-electron microscopy (cryo-EM), we determined the structure of PDCoV RBD bound to the host receptor at 2.7 Å and revealed the binding interface that allows for PDCoV to engage the host receptor, APN. Structural analysis of the mammalian and avian PDCoV RBD-APN complexes revealed a conserved mechanism of host engagement for avian and mammalian receptors. Yet, differences were observed in host glycan recognition by PDCoV RBD. By leveraging mutations that alter host APN glycans we demonstrate through binding and viral entry assays that host glycans play an important role in viral recognition.

Given that the receptor binding interface is essential for the virus to enter, disruption of this interface would be detrimental to the virus. We sought to systematically determine how mutations at this interface would impact binding, as this would aid efforts in understanding viral evolution and guide the design of an ideal vaccine candidate for PDCoV. Through quantitative deep mutational scanning (DMS) we evaluated the effect of all possible single amino acid substitutions spanning the entire 100 amino acid receptor binding interface using a yeast-displayed RBD platform. From this screen, we discovered that most of the mutations were detrimental to the virus and would be unlikely to occur naturally. However, we surprisingly found three sites that when mutated led to enhanced binding and viral entry to APN orthologs.

2.3. Porcine delta-coronavirus engages a diverse set of APN receptor orthologs

We sought to investigate the molecular mechanism of PDCoV receptor engagement by performing binding, entry analysis, and structural characterization of PDCoV and key representative host species: galline, human and porcine. Biolayer interferometry (BLI) was performed to determine the affinity of PDCoV RBD to APN orthologs. PDCoV RBD had a higher affinity for the avian receptors; gAPN, mAPN, bAPN (exception for sAPN) and mammalian hAPN but not detectable binding to pAPN (Figure 2.3.1A, Table 2.3.1). While binding of RBD to pAPN was not detected through BLI, it was reported by Ji W. et al. 2022 Nature Communications using surface plasmon resonance (SPR) with a Kd to be 44mM. This trend was recapitulated in a cell-based entry assay with Vesicular Stomatitis Virus (VSV) pseudotyped with PDCoV S in Hek293-T cells transfected with hAPN, pAPN, gAPN, mAPN, sAPN, and bAPN receptors. We observed the avian receptors gAPN, mAPn, bAPN (except sAPN) and mammalian hAPN supported efficient entry whereas limited entry was detected for pAPN (Figure 2.3.1B). Western blot analysis of APN expression in Hek293T demonstrates that the observed viral entry is not due to a lack of or differences in host receptor expression post transfection (Figure 2.3.1C). This was a surprising discovery as PDCoV primarily circulates in porcine with sparse spillover cases in humans. However, it is not surprising to observe high affinity and viral entry supported by avian APN receptors as PDCoV originated from avian DCoVs (Figure 1.1.1).

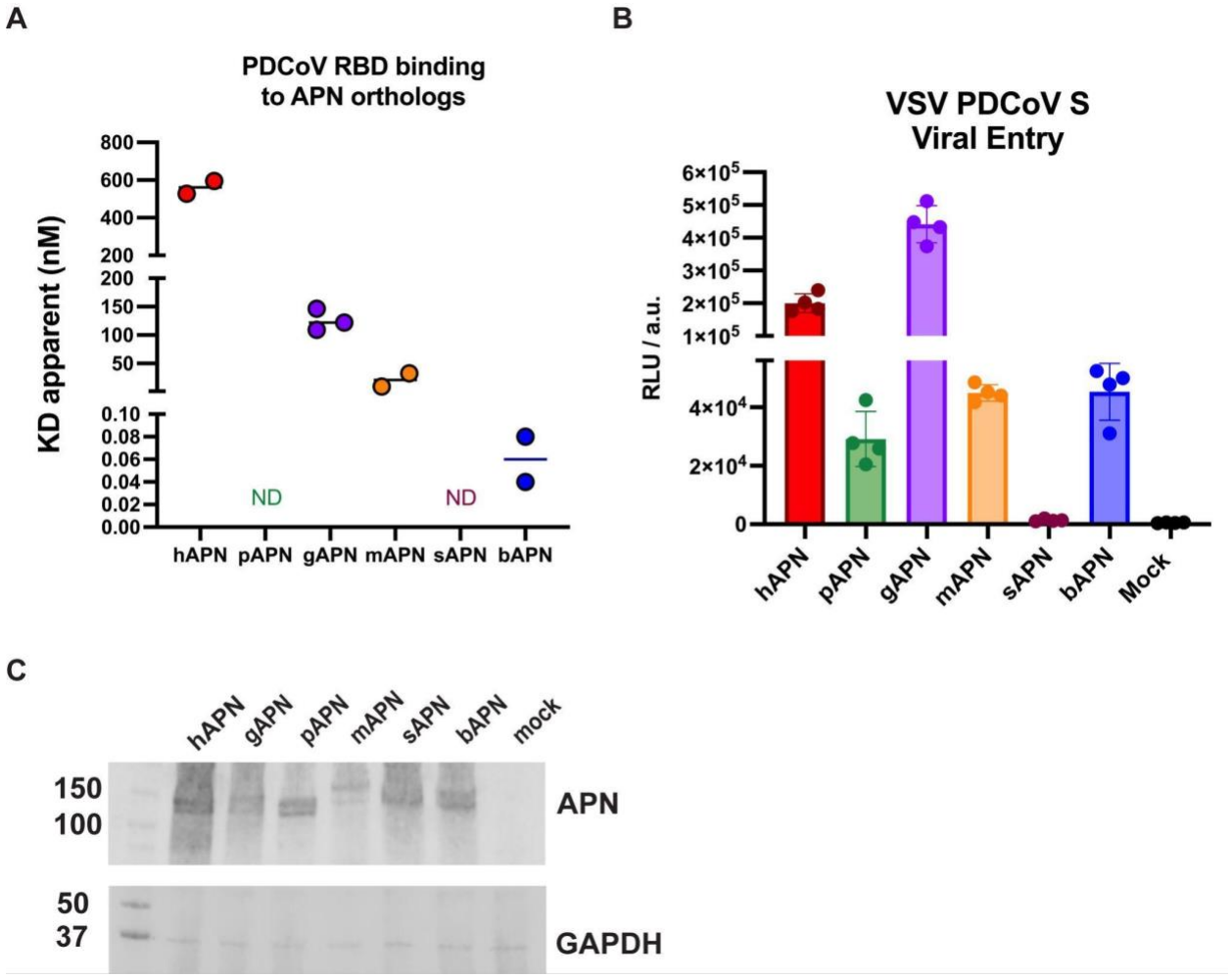

Figure 2.3.1: PDCoV engagement of diverse receptors A, Binding affinities using biolayer interferometry (BLI) of PDCoV RBD binding to APN receptor orthologs from human (hAPN red), porcine (pAPN green), galline (gAPN purple), munia (mAPN orange), sparrow (sAPN maroon) and bulbul (bAPN blue). Bars correspond to geometric means of biological replicates of purified APN receptors n=2. **B,** Entry of VSV pseudotyped with PDCoV S_{IL121_2014} in Hek293-T cells transfected with APN receptors from human, porcine, galline, munia, sparrow and bulbul. Bars correspond to geometric means of biological replicates of pseudovirus n=3. **C,** Western blot of APN and GAPDH expression in Hek293-T cell lysates transfected with APN receptors from human, porcine, galline, munia, sparrow and bulbul.

		KD (M)	KD Error	ka (1/Ms)	ka Error	kdis (1/s)	kdis Error
human APN	n=1	5.95E-07	8.69E-09	8.34E+04	1.19E+03	4.96E-03	1.52E-05
	n=2	5.28E-07	1.10E-09	3.40E+03	6.10E+00	1.80E-03	1.88E-06
porcine APN	n=1	N/A					
	n=2	N/A					
gAPN APN	n=1	1.22E-07	3.52E-10	2.11E+04	5.78E+01	2.58E-03	2.38E-06
	n=2	1.09E-07	2.68E-10	2.04E+04	4.16E+01	2.23E-03	3.04E-06
	n=3	1.47E-07	7.91E-10	1.42E+04	7.36E+01	2.09E-03	3.23E-06
munia APN	n=1	9.19E-09	3.95E-10	3.93E+03	1.42E+01	3.61E-05	1.55E-06
	n=2	3.26E-08	1.38E-10	7.71E+03	1.35E+01	2.52E-04	9.71E-07
sparrow APN	n=1	N/A					
	n=2	N/A					
bulbul APN	n=1	4.21E-11	N/A	5.43E+03	2.74E+01	2.29E-07	N/A
	n=2	7.94E-11		1.78E+03	1.63E+01	1.41E-07	

Table 2.3.1. Table of the KDs, association (K_a) and dissociation rate constants (K_{dis}) for duplicate lots of PDCoV RBD_{IL121_2014} binding to APN orthologs human, porcine, galline, munia, sparrow and bulbul.

2.4. The molecular basis of receptor binding of PDCoV

To understand the molecular basis for high binding affinity and efficient utilization of gAPN, as compared to hAPN and pAPN, we determined the cryo-EM structure of the PDCoV RBD bound to gAPN at 2.4 Å resolution. The structure reveals that the RBD contains three key loops (1-3) that are involved in binding to the host gAPN receptor. Loops 1 and 3 are buried within the pockets of the gAPN receptor, suggesting a mechanism by which the virus may protect and shield the receptor-binding loops from the harsh conditions of the intestine and the immune system (Figure 2.4.1A).

In loop 1, RBD residues D317, E320 and R322 are the drivers of specificity as they form hydrogen bonds and salt bridges with gAPN residues K382, Y372, E429, W432. In addition, RBD residue F318 nicely stacks against gAPN residue Y319 (Figure 2.4.1B).

Loop 2 of the RBD is smaller and points away from the binding site. Interestingly, the exposed region of the loop is held together by a disulfide bond at C349-C352 - possibly to protect this loop from the host environment. We do observe two key specific interactions contributed by loop 2, R357 to gAPN residue N741 and glycan N742.

In loop 3, a series of backbone-to-backbone interactions dominate this interface. The RBD backbone ranging from Y398, L399, L400 interacts with the backbone gAPN (A745, I746, P747), through a hydrogen bond network. Side chain to backbone interactions occur with the amide on RBD-W396 forming a hydrogen bond with the backbone of gAPN-A375, the amide from RBD-N397 forming a hydrogen bond with the backbone of gAPN-T744, the backbone amide from RBD L400 interacting the hydroxyl from gAPN-S748. There is one side chain specific interaction RBD

R401 which forms a hydrogen bond with gAPN-S748. Loop 3 provides an extensive hydrogen bond network through backbone-to-backbone interactions possibly affording the RBD the ability to bind a diverse set of host receptors.

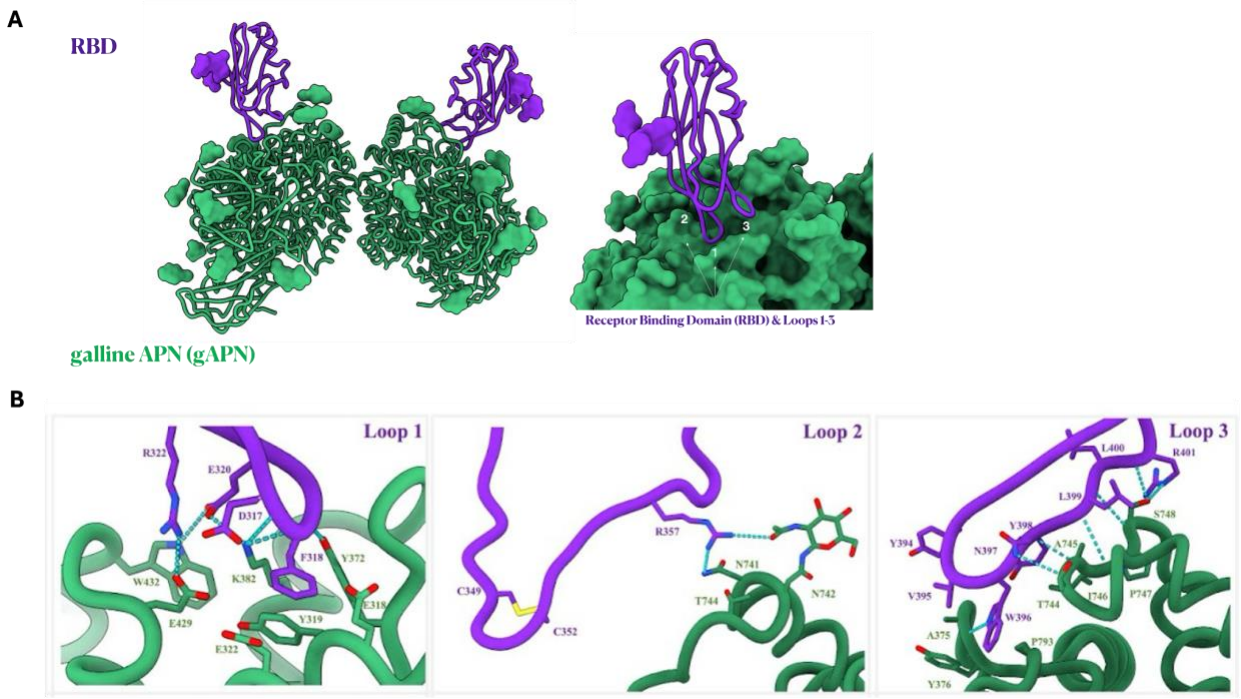

Figure 2.4.1. The molecular mechanism of binding of PDCoV RBD to gAPN A, Cryo-EM structure of PDCoV RBD (purple) bound to host receptor gAPN (green) using the three binding loops at the tip of the RBD (labeled in white as 1-3) **B,** Receptor binding interface of PDCoV RBD and gAPN throughout loops 1-3. Key interactions of each loop are demonstrated with hydrogen bonds shown as dashed blue lines.

Structural comparison of the PDCoV RBD-gAPN complex to PDCoV RBD-hAPN and PDCoV RBD-pAPN complex reveals that the RBD maintains the same conformation across species (Figure 2.4.2A-C). The cryo-EM structure of PDCoV RBD | gAPN does reveal the presence of the second glycan on the RBD and an improved resolution of the RBD at the distal ends of the binding interface (Figure 2.4.2A-C). Neither of the two glycans present on the RBD interact with the receptors, as their location is distant from the receptor binding interface. In contrast, other coronaviruses such as CCoV HuPN 2018 contain one glycan near the receptor binding domain interface and as such make contact with human APN (1). In PDCoV these two RBD glycans likely serve as a shield of the RBD from host proteases and immune recognition.

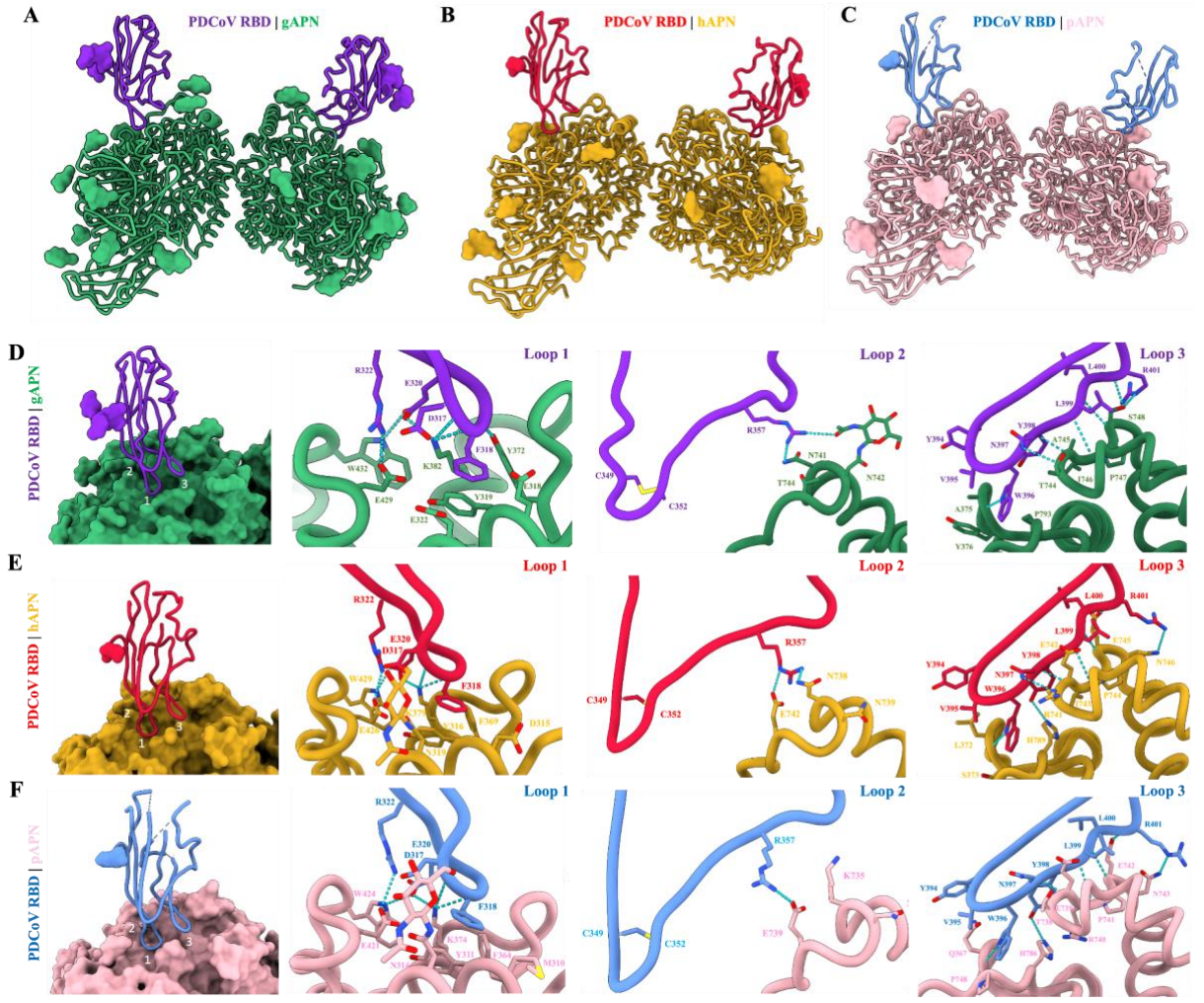

Figure 2.4.2: Molecular basis of binding of PDCoV RBD to APN orthologs. **A,** Ribbon diagram of the galline APN (gAPN) bound PDCoV RBD_{IL121_2014} cryo-EM structure at 2.4 Å resolution. PDCoV RBD_{IL121_2014} is rendered in purple and gAPN is colored in green. **B,** Ribbon diagram of the human APN (hAPN) bound PDCoV RBD_{IL121_2014} x-ray structure at 3.1 Å resolution. PDCoV RBD_{IL121_2014} is rendered in red and hAPN is colored in gold. **C,** Ribbon diagram of the porcine APN (pAPN) bound PDCoV RBD_{IL121_2014} x-ray structure at 2.7 Å resolution. PDCoV RBD_{IL121_2014} is rendered in blue and pAPN is colored in pink. **D-F,** Zoomed-in views of the interface between PDCoV RBD_{IL121_2014} loop 1, 2, 3 and the receptor APN orthologs gAPN, hAPN, and pAPN. Selected hydrogen bonds and salt bridges are shown as blue dashed lines.

Interestingly, we see a highly conserved receptor-binding interface across the three species consisting of the three binding loops 1-3. Loop 1 serves as the main driver of specificity, with loop 2 contributing minimal contacts, and loop 3 serving as a non-specific backbone scanner affording the RBD the tropism in host receptor utilization. Structural analysis of all three orthologs suggests

possible reasons that explain the difference in affinities and viral entry across the orthologs. In loop 1, gAPN contains Y372 rather than F369 hAPN, F364 pAPN providing an additional hydrogen bond that is not present in the equivalent APNs. Interestingly, in loop 1 hAPN and pAPN contain a bulky glycan (N319 , N314) that is not present in gAPN which contains E322. This glycan does not form hydrogen bonds and instead could be serving as a gatekeeper and perturbing the on/off rate of RBD binding. In loop 2, gAPN R357 forms a hydrogen bond with the glycan at N742 which is lacking in hAPN and pAPN as they do not contain a glycan at that position. In loop 2, pAPN has one less contact than either hAPN and gAPN, as K735 sits in this position. In loop 3, there are no notable differences across the orthologs further alluding to the hypothesis that this loop can be used to engage a wide range of receptors if the side chains of the APN receptor are not bulky which would lead to clashes and disruption of the backbone-backbone interface (Figure 2.4.2D-F).

2.5. Host receptors glycans influence binding and viral entry of PDCoV

While the glycans on PDCoV RBD do not play a role in binding, host receptor glycans appear to play a role. Glycosylation patterns across the three receptor APN orthologs are not uniformly shared and specifically two glycans stood out for being near the receptor RBD loop 1 and RBD loop 2 (Figure 2.5.1A).

We noticed that hAPN and pAPN contain a glycan at position N319, N314 near RBD loop 1 which we hypothesized could disrupt engagement of the RBD loop 1 with the neighboring host receptor. To determine if the glycans disrupt binding we attempted to induce hAPN/pAPN receptor glycan mimicry in gAPN and introduced the substitution gAPN E322N. Viral entry of PDCoV S VSV into HEK293T target cells transiently transfected with gAPN E322N substitution led to reduced viral entry (Figure 2.5.1D). Furthermore, removal of the glycan in hAPN through a N319A substitution led to enhanced binding to PDCoV RBD and viral entry of PDCoV S VSV into HEK293T target cells transiently transfected with hAPN harboring hAPN N319A substitution (Figure 2.5.1B). Strikingly, removal of the glycan in pAPN through a N314A substitution led to detectable PDCoV RBD using BLI and enhanced viral entry of PDCoV S VSV into HEK293T target cells transiently transfected with hAPN harboring hAPN N314A substitution (Figure 2.5.1C). A glycan at this position appears to disrupt the on/off rate of RBD binding and viral entry.

The second glycan of interest is uniquely positioned to interact with loop 2 of RBD however, only gAPN and pAPN share this exact glycan location; human APN contains a glycan upstream at N735 position rather than at N738 (2.5.1A). This shift would displace the glycan further into the back end of loop 2, placing the current N735 within 8-10 Å from the neighboring residues on the RBD. To test our hypothesis that this glycan plays a role in binding we created a gAPN glycan N742A and performed binding and viral entry analysis of this substitution. We observed attenuated binding and viral entry of gAPN without a glycan (Figure 2.5.1E). Introduction of the equivalent

N741 from gAPN into hAPN led to enhanced binding and viral entry (Figure 2.5.1F). Furthermore, removal of pAPN K735A substitution leads to increased viral entry for pAPN as K735 appears to disrupt interaction of RBD R357 with the glycan (Figure 2.5.1G).

A

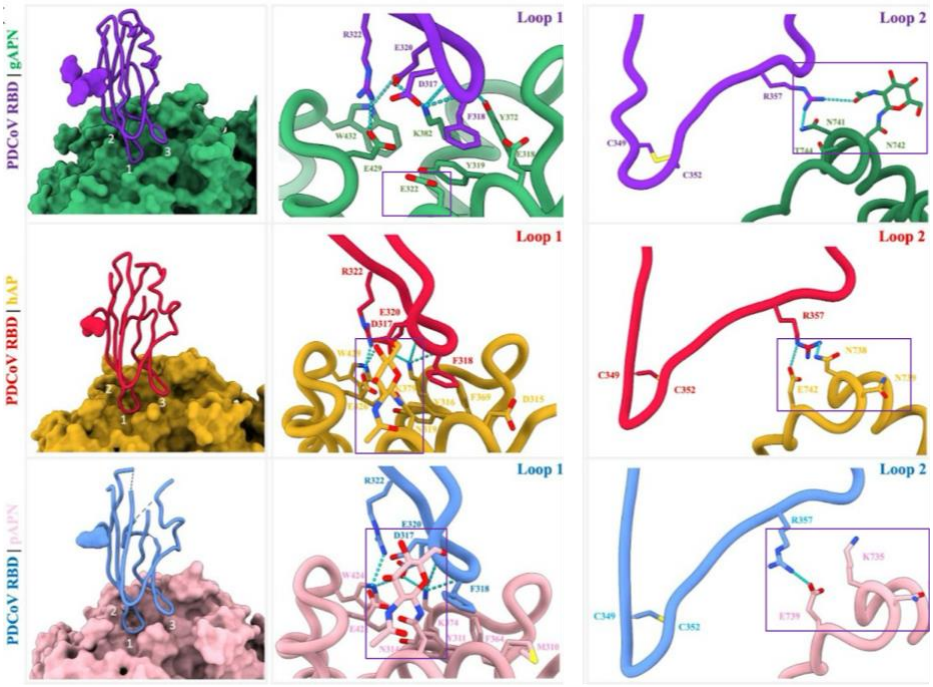

B

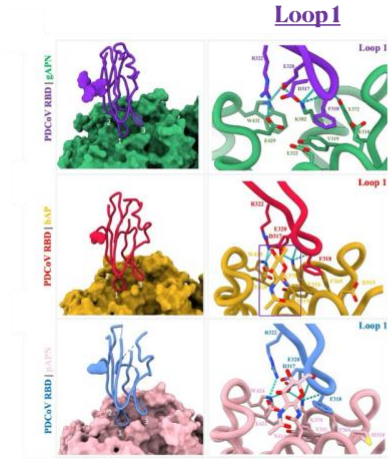

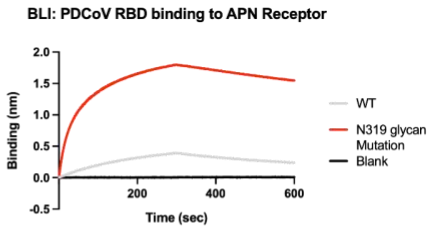

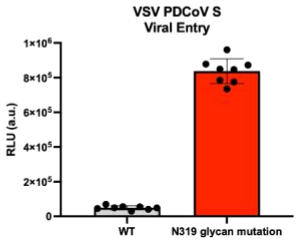

C

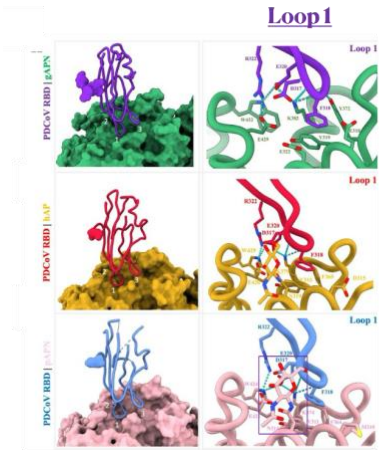
Loop1
PDCoV RBD | gAPN
PDCoV RBD | hAP
PDCoV RBD | hAPN
Loop 1

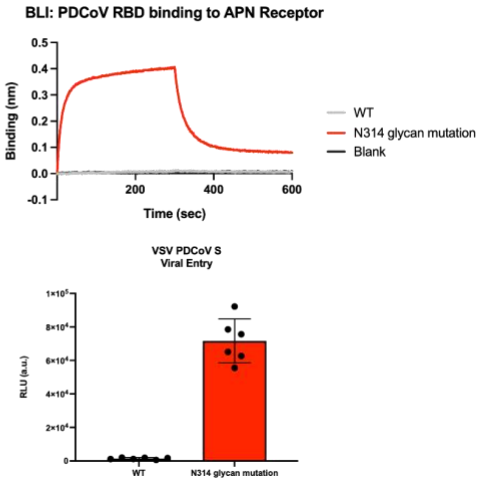
BLI: PDCoV RBD binding to APN Receptor
Binding (nm)
Time (sec)
WT
N314 glycan mutation
Blank
VSV PDCoV S
Viral Entry
RLU (a.u.)
WT
N314 glycan mutation

D

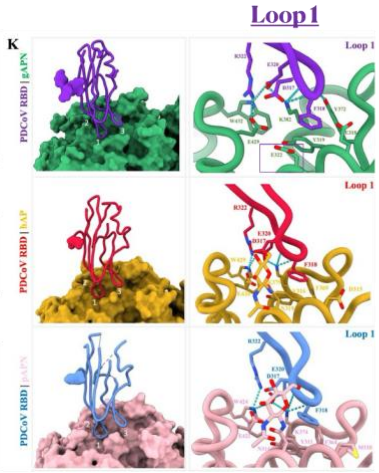
Loop1
K
PDCoV RBD | gAPN
PDCoV RBD | hAP
PDCoV RBD | hAPN
Loop 1

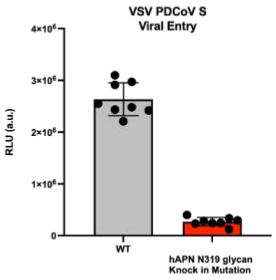
VSV PDCoV S
Viral Entry
RLU (a.u.)
WT
hAPN N319 glycan
Knock in Mutation

E

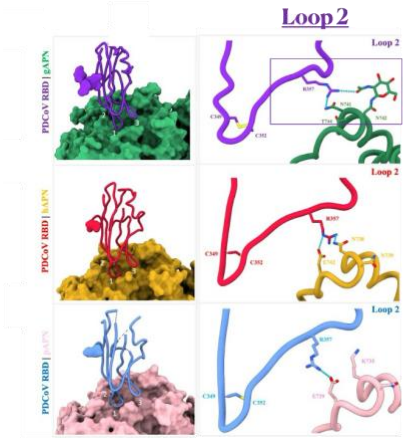
Loop2
PDCoV RBD | gAPN
PDCoV RBD | hAPN
PDCoV RBD | hAPN
Loop 2

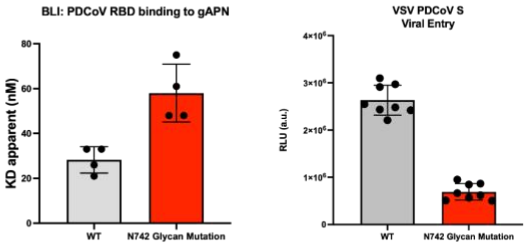
BLI: PDCoV RBD binding to gAPN
KD apparent (nM)
WT
N742 Glycan Mutation
VSV PDCoV S
Viral Entry
RLU (a.u.)
WT
N742 Glycan Mutation

F

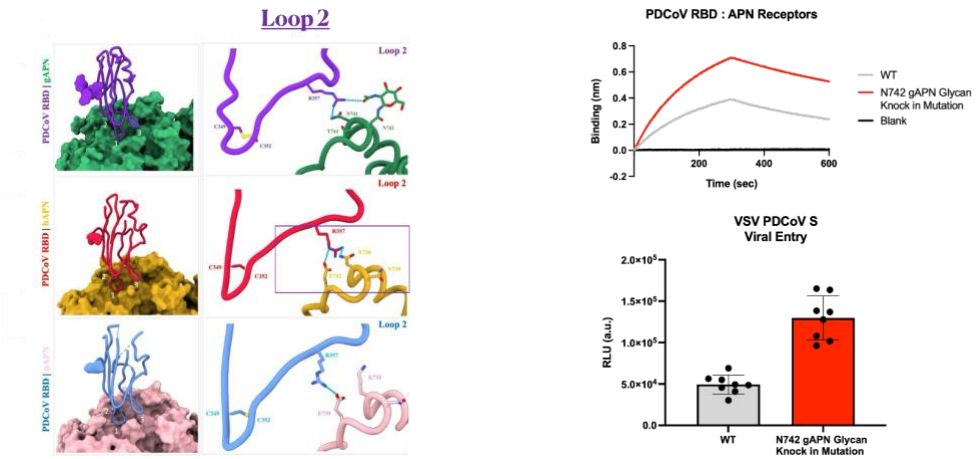

G

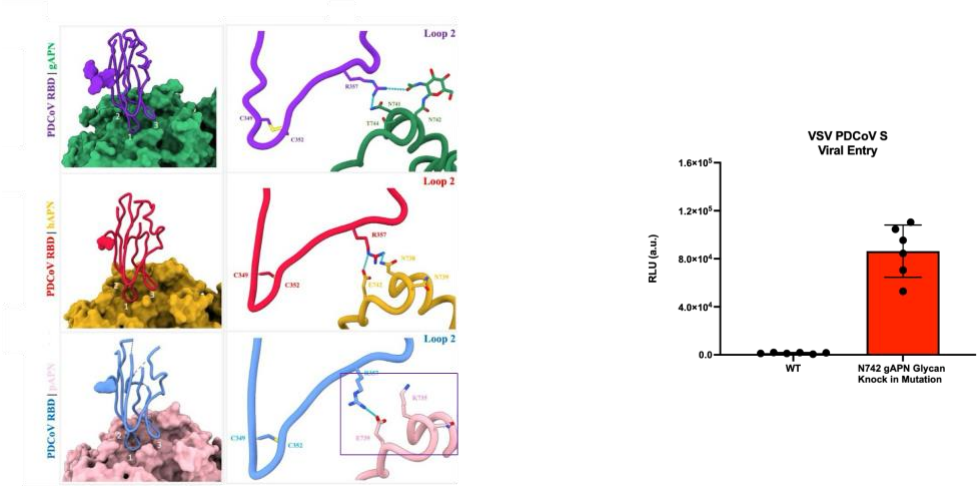

Figure 2.5.1: Host receptor glycans play a role in PDCoV viral entry and binding. A, Ribbon diagram of PDCoV RBD bound to gAPN, hAPN and pAPN highlighting the host glycans near RBD loop 1 and RBD loop 2. **B,** Binding analysis of PDCoV RBD to hAPN N319A glycan substitution using BLI. Viral entry of PDCoV S VSV into HEK293T target cells transiently transfected with hAPN T321A glycan substitution removing the N319 glycan. **C,** Binding analysis of PDCoV RBD to pAPN N314A glycan substitution using BLI. Viral entry of PDCoV S VSV into HEK293T target cells transiently transfected with pAPN T316A glycan substitution removing the pAPN N314 glycan. **D,** Viral entry of PDCoV S VSV into HEK293T target cells transiently transfected with gAPN E322N substitution adding a glycan at E322 and mimicking hAPN N319 and pAPN N314 glycan position. **E,** Binding analysis of PDCoV RBD to gAPN N742A glycan substitution using BLI. Viral entry of PDCoV S VSV into HEK293T target cells transiently transfected with gAPN T744A substitution removing the N742 glycan. **F,** Binding analysis using BLI of PDCoV RBD to hAPN N735T/R741T substitutions that add a glycan mimicking the gAPN N742 glycan position. Viral entry of PDCoV S VSV into HEK293T target cells transiently

transfected with hAPN N735T/R741T substitutions that add in a glycan mimicking gAPN N742 glycan position. **G,** Viral entry of PDCoV S VSV into HEK293T target cells transiently transfected with pAPN K735A substitution that removes the perturbing lysine that allows for glycan at N736 to interact with R357.

2.6. Deep mutational scanning of the PDCoV receptor binding domain identifies substitutions altering APN receptor ortholog usage

We sought to systematically determine how mutations at this interface would impact binding, as this would aid efforts in understanding viral evolution and guide the design of an ideal vaccine candidate for PDCoV. We used a quantitative deep mutational scanning (DMS) approach to evaluate the functional impact of all possible single amino acid substitutions spanning the entire PDCoV RBD on galline, human, and porcine APN-binding affinity. We created a duplicate mutant library of these substitutions and cloned this library into a yeast-surface display platform. Surface expression of the pooled yeast mutant RBD library was induced, bound to the three APN orthologs and subjected to high-throughput fluorescence-activated cell sorting sequencing (FACS-seq). A full concentration gradient was tested for gAPN, yielding an estimate of $\log_{10}$(Ka) for each substitution and delta $\log_{10}$Ka for each mutation over wild type. Due to the poor affinity of PDCoV RBD to hAPN and pAPN, only one concentration at 1μM of APN was feasible and the mean fluorescence intensity (MFI) for each mutant were obtained and delta MFI were estimated over wild type. Surprisingly, in contrast to SARS-CoV-2 RBD, PDCoV RBD is limited in its capacity to sample a vast fraction of substitutions, as the majority of the mutations are detrimental to binding for all three APN orthologs (Figure 2.6.1A-C) (4).

However, we found a subset of substitutions at the RBD-APN receptor interface that had an enhancing effect on binding to APN orthologs. Favorable RBD substitutions for all APNs: Y394R/H, V395W/R. Favorable RBD mutations for hAPN: G319WF, E320TF, L399QY. Favorable RBD mutations for pAPN: K389G, Y398TWI. Favorable RBD mutations for gAPN: R357WY, K389Q, R403K. These mutations are found across the three binding loops of RBD. Furthermore, we determined if the DMS of PDCoV RBD could predict the effect in binding to APN orthologos of naturally occurring PDCoV variants. We took a subset of circulating variants and calculated the fold change over wild type for each of the mutations observed in that variant (Figure 2.6.1D). Only four out of the nineteen naturally occurring PDCoV variants HKD JPN 2016, 110_1197_TW, HKU15_SD2018 and Thailand_S5011_2015 contained RBD mutations that are expected to enhance binding to APN orthologs, as the majority of the mutations are expected to dampen binding.

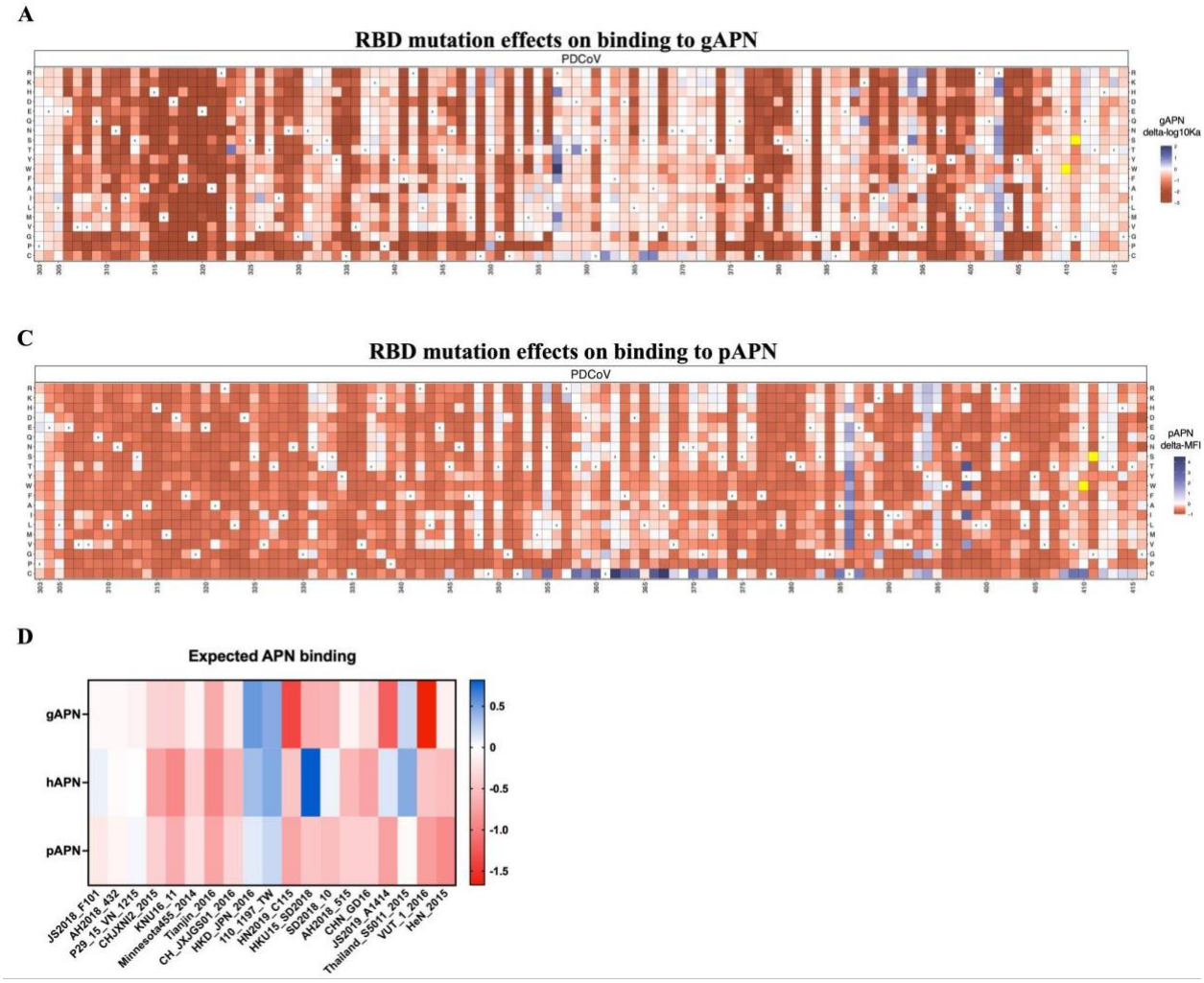

Figure 2.6.1: PDCoV RBD Deep mutational scan against galline, human and porcine APN mutation A, Heatmap of PDCoV RBD mutation effects on binding to galline APN with delta-log 10 Ka plotted in red for perturbed binding and blue for enhanced binding **B,** Heatmap of PDCoV RBD mutation effects on binding to human APN with delta mean fluorescence intensity (MFI) plotted in red for perturbed binding and blue for enhanced binding **C,** Heatmap of PDCoV RBD mutation effects on binding to porcine APN with delta-MFI are plotted in red for perturbed binding and blue for enhanced binding 4 **D,** Heatmap of PDCoV RBD isolates and the expected binding affinities to galline, human and porcine APN with perturbed binding indicated in red and enhanced binding in blue.

2.7. PDCoV RBD-APN interface mutations lead to enhanced binding and entry to APN orthologs

We next determined binding kinetics of the RBD mutations and variants to APN orthologos using biolayer interferometry (BLI). We expressed and purified individual RBD components and

acquired affinity constants (Kd) to gAPN, hAPN and pAPN (Figure 3 A-C, S3). From an initial starting point of 19 possible enhancing mutations from the deep mutational screen, we honed in on three: R357W/Y in loop 2, L399Q and R401N in loop 3. The R357W/Y mutation leads to a ~ thirty-fold increase in affinity for gAPN that is driven by the k_{off} rate (Figure 2.7.1, 2.7.2). Interestingly, R357W dampens binding to hAPN so that no binding can be detected by BLI; while R357Y retains similar binding to hAPN as WT (Figure 2.7.1B). R357W/Y has no effect on binding to pAPN that could be measured using BLI (Figure 2.7.1C). This gAPN specific preference by R357W/Y could be accounted for by the ability to maintain the hydrogen bond with N741 (Figure 2.7.1D). In contrast, hAPN and pAPN would lose an important salt bridge between R357 to E742/E739 (respectively) that can't be gained back from any glycan interaction since hAPN has no glycan at N738 and pAPN has K735 that can provide steric hindrance to interactions with the glycan at N736.

In loop 3, we previously argued that the major force holding this loop together are non-residue and receptor specific hydrogen bond backbone interactions. The mutation L399Q morphs loop 3 into a human and porcine receptor specific recognition loop (Figure 2.7.1A-C). L399Q has a drastic effect on binding with a fifty-five fold increase in affinity over WT to hAPN and detectable binding to pAPN. This could be due to the gain of a hydrogen bond by L399Q in hAPN with E742 and E739 in pAPN (Figure 2.7.1E), while for gAPN there is no equivalent negatively charged residue to form a hydrogen bond. Last, R401N was found to be the all encompassing substitution, as it enhances binding kinetics to all three APN orthologs (Figure 2.7.1A-C). This could be driven by R401N gaining a more favorable hydrogen bond with gAPN S748, while forming a new salt bridge with hAPN E745 and pAPN E742 (Figure 2.7.1F). From the four PDCoV isolates expected to have enhancing binding we found only one, PDCoV variant HKU15_SD2018 (abbreviated as MIN for M354I/I391V/N397K), to have enhanced binding to hAPN and pAPN (Figure 2.7.1B-C) with a five fold increase in affinity to hAPN. The MIN variant contains one mutation in loop 2, M354I which may impact stability but not influence binding, and two mutations in loop 3, where we see N397 involved in hydrogen bonding and I391 serving as a hydrophobic packing residue. Substitution of N397K could lead to the formation of a salt bridge with hAPN E742 and pAPN E73, and a hydrogen bond with hAPN R741. In gAPN there is no glutamate at the equivalent position as hAPN and pAPN (Figure 2.7.1F).

Inspired by the most recent observations of epistasis occurring in SARS-CoV-2 leading to an accelerated selection of highly infectious variants, we wanted to ask what impact combining mutations would have on affinity. We combined loop 3 enhancing hAPN and pAPN specific mutation L399Q and the all encompassing enhancing mutation R401N. The double mutant leads to enhanced binding of five fold for pAPN as compared to the individual point mutations (Figure 2.7.1C). While for hAPN it maintains the drastic affinity gain to WT but it does not improve binding past L399Q as a single point mutation (Figure 2.7.1B).

Furthermore, the addition of R357W/Y onto the loop 3 double mutant L399Q-R401N to make the triple mutants does not lead to combined enhanced binding (Figure 2.7.1A-C). For gAPN that could be explained by the positive interactions seen from substitution of R357W/Y which then is dampened by the addition of disfavored amino acids at loop 3. In a similar manner, the positive effect by L399Q-R401N was dampened by the disfavored substitution of R357W/Y in loop 2. In pAPN, it was not evident what effect R357W/Y had, since no binding can be detected for both wild type and mutant, however, we can reason to conclude that it was not a favorable interaction from the structural analysis and by the data that the enhanced binding seen from L399Q-R401N is now lost.

Next, we evaluated the effect of the DMS mutants using VSV pseudotyped with S glycoprotein on Hek293-T transfected with APN orthologs, hAPN, gAPN and pAPN. PDCoV S harboring the R357W/Y mutation led to enhanced viral entry across all APN orthologs. While PDCoV S harboring R401N and L399Q led to enhanced viral entry only with hAPN and pAPN receptor orthologs. PDCoV S harboring double and triple mutant outcompeted single mutants in fold entry over WT suggesting a possible synergistic mechanism of these residues (Figure 2.7.3). To address if the observed viral entry of PDCoV S harboring these DMS mutants is due to the inherent binding affinity and conformational changes induced by the mutations and not protein expression, a western blot was performed to detect the levels of PDCoV S on the surface of the VSV. We observe similar levels of PDCoV S across all PDCoV harboring DMS mutants as compared to wild type (Figure 2.7.3D).

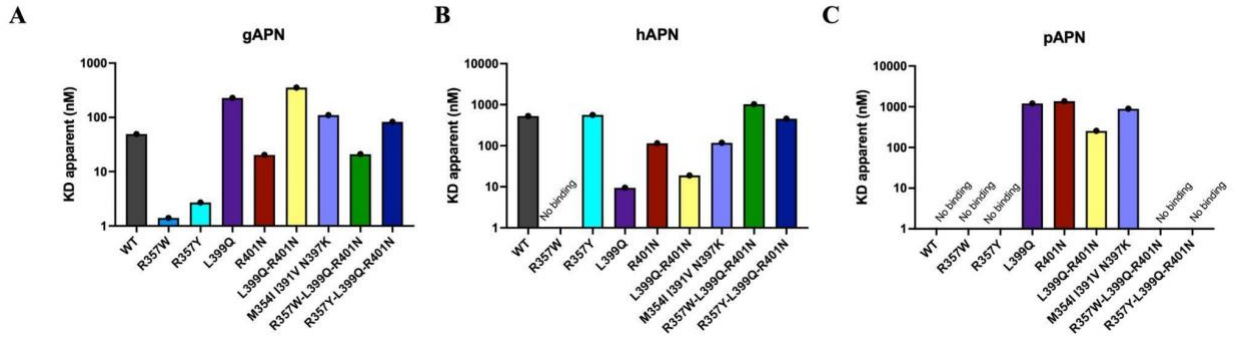

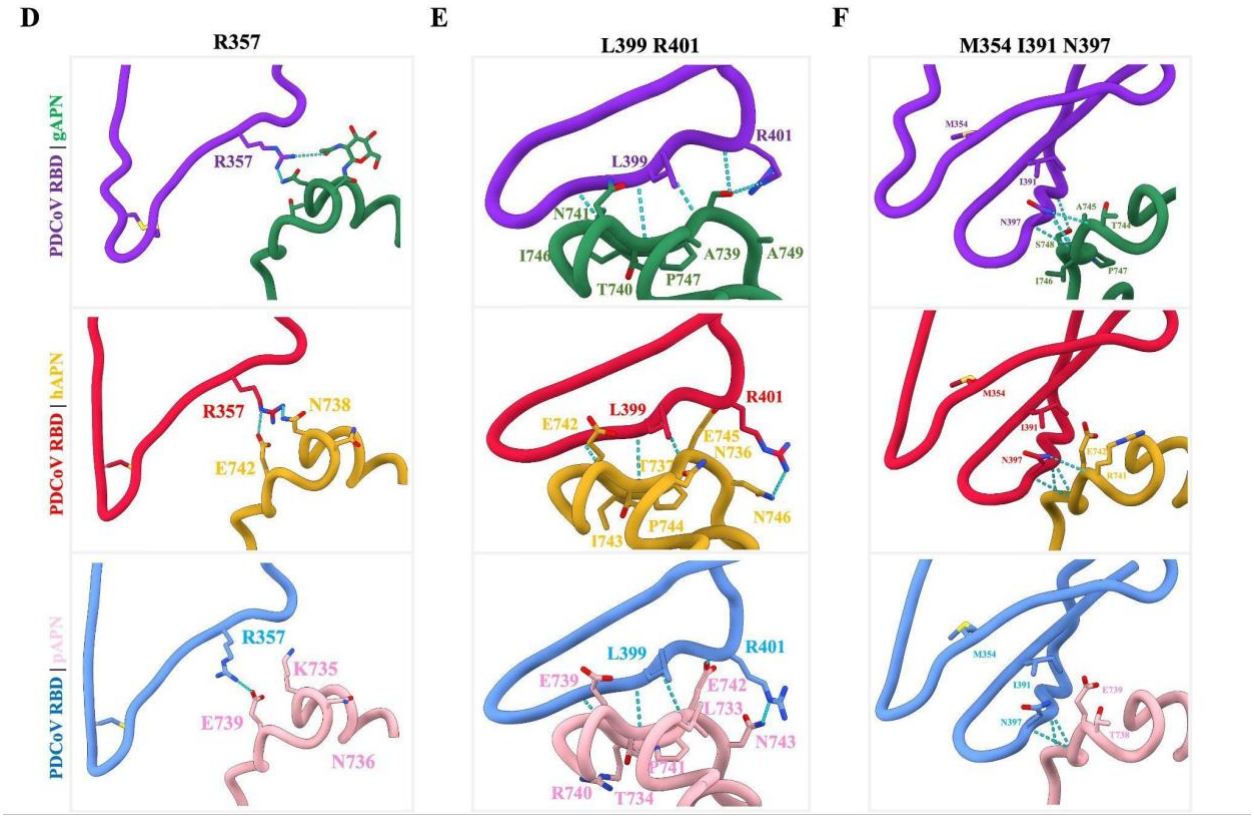

Figure 2.7.1: Binding kinetics of PDCoV RBD-APN interface mutations **A-C,** Dissociation constants (Kd) using BLI of RBD wild type (WT), DMS single point mutations (R357W-Y, L399Q, R401N), DMS double point mutant (L399Q/R401N), DMS triple point mutants (R357W-Y/L399Q/R401N) and PDCoV variant HKU15_SD2018 (abbreviated as MIN for M354I/I391V/N397K) against APN orthologs **D-F,** Structural analysis of the binding interactions for the RBD DMS mutants and MIN variant to APN orthologs**.**

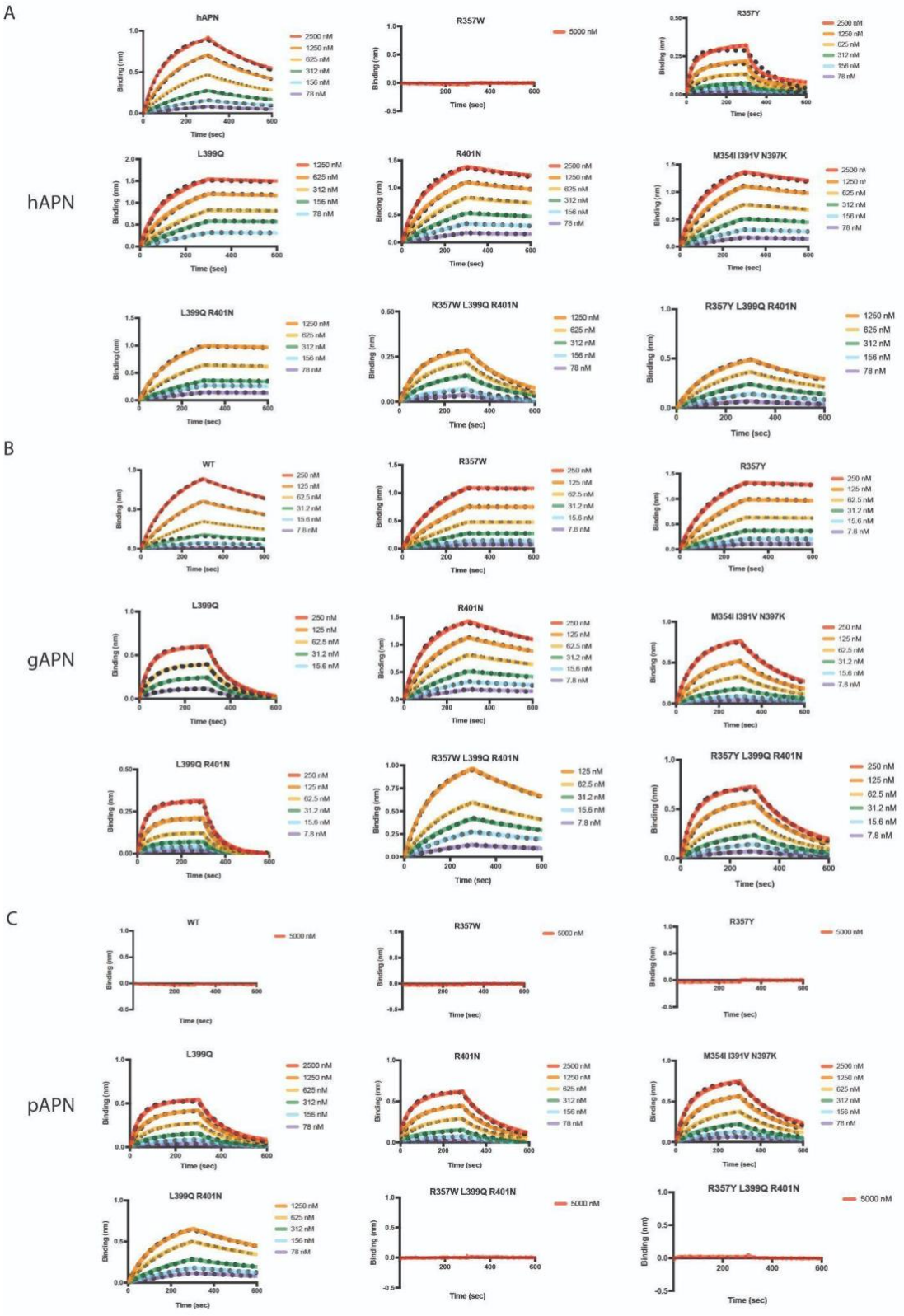
A
hAPN
hAPN
B
gAPN
C
pAPN
WT
R357W
R357Y
L399Q
R401N
M354I I391V N397K
L399Q R401N
R357W L399Q R401N
R357Y L399Q R401N
Binding (nm)
Time (sec)
2500 nM
1250 nM
625 nM
312 nM
156 nM
78 nM
5000 nM
250 nM
125 nM
62.5 nM
31.2 nM
15.6 nM
7.8 nM

Figure 2.7.2: Binding curves and fits for PDCoV RBD to h, g, pAPN receptor

A

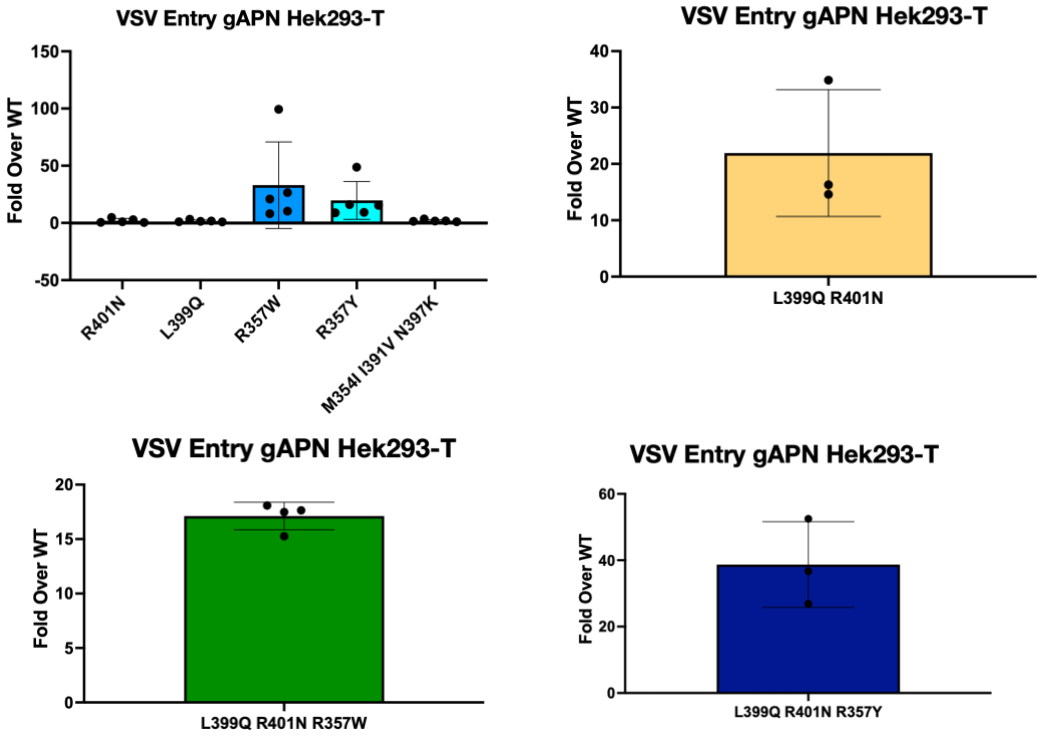

B

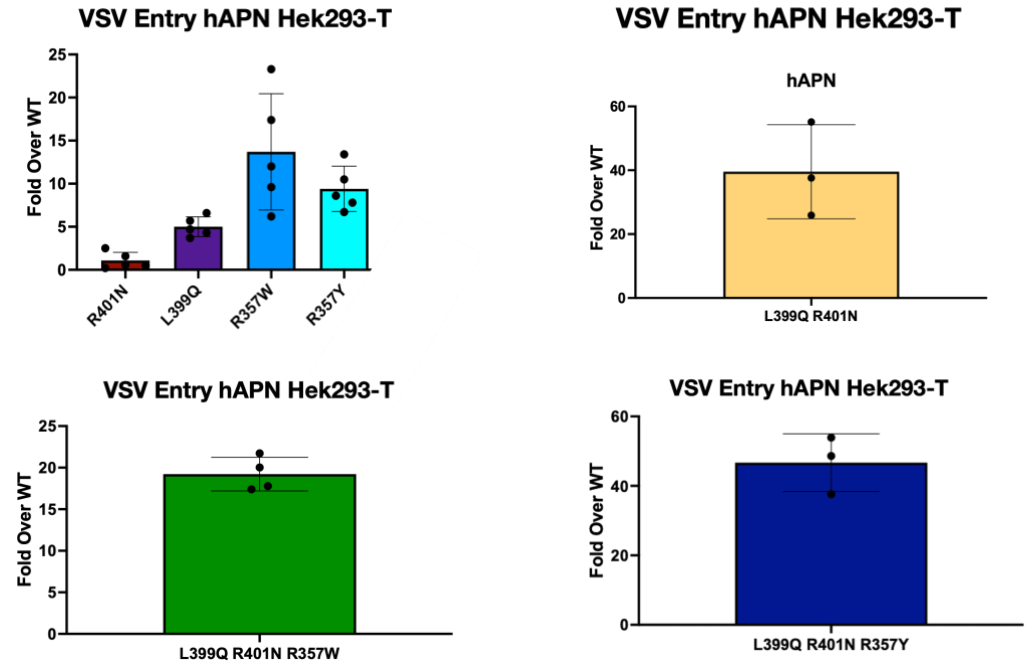

C

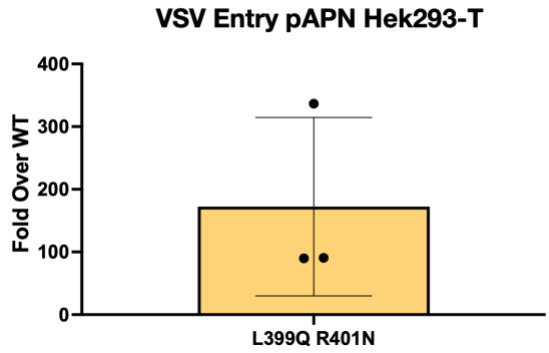
VSV Entry pAPN Hek293-T
Fold Over WT
400
300
200
100
0
L399Q R401N

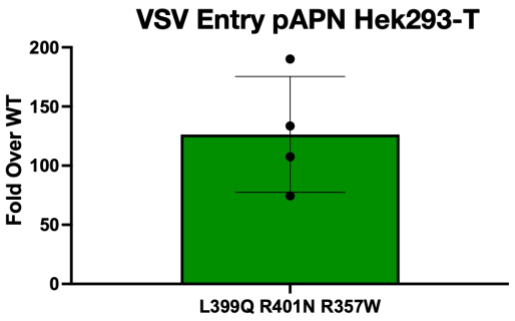
VSV Entry pAPN Hek293-T
Fold Over WT
200
150
100
50
0
L399Q R401N R357W

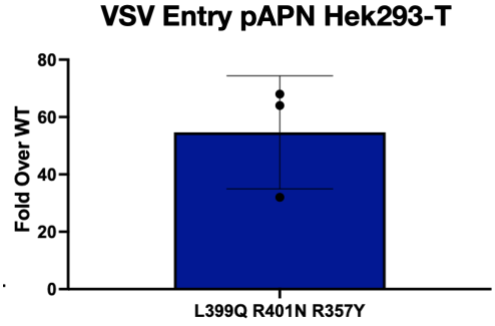
VSV Entry pAPN Hek293-T
Fold Over WT
80
60
40
20
0
L399Q R401N R357Y

D

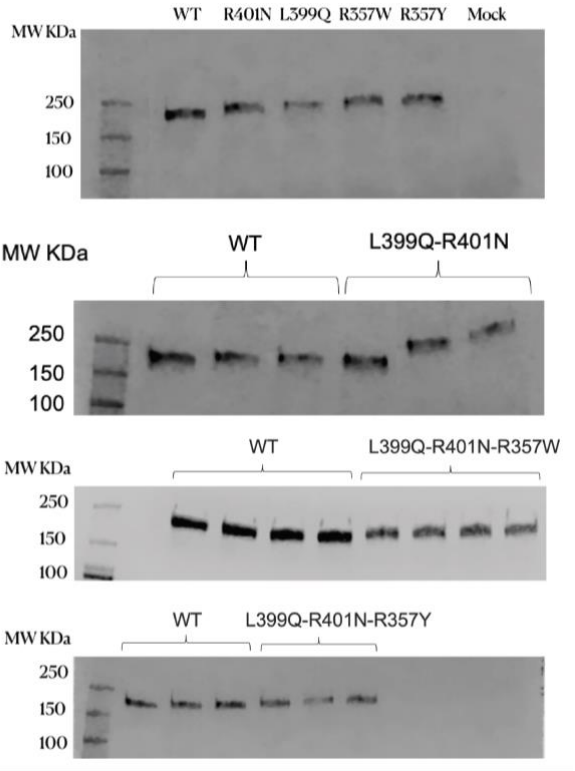
WT R401N L399Q R357W R357Y Mock
MW KDa
250
150
100
MW KDa
WT
L399Q-R401N
250
150
100
WT
L399Q-R401N-R357W
MW KDa
250
150
100
WT
L399Q-R401N-R357Y
MW KDa
250
150
100

Figure 2.7.3. PDCoV DMS mutants lead to enhanced viral entry. A, VSV viral entry with PDCoV S DMS mutations in Hek293-T transfected with gAPN. **B,** VSV viral entry with PDCoV S DMS mutations in Hek293-T transfected with hAPN. **C,** VSV viral entry with PDCoV S DMS mutations in Hek293-T transfected with pAPN. **D,** Western blot analysis of PDCoV Spike on VSV for WT and DMS mutations

2.8. Characterization of PDCoV Spike harboring deep mutational mutants

Gain of function mutations are of high concern as they pose a threat to human and animal health. The three residues R357, L399, R401 identified through DMS were of major interest to us as they led to enhanced binding and viral entry. In order to determine how these mutations impacted the conformation and stability of the spike, the ectodomain of the spike harboring these mutations were expressed and tested. We observed the expression of PDCoV S protein harboring DMS mutations L399Q, R401N along with the naturally circulating M354I-I391V-N397K. Surprisingly, we found limited expression of PDCoV S protein harboring DMS mutations R357W/Y (Figure 2.8.1).

Further, to determine the conformation changes these mutations have on the spike negative stain microscopy and 2D classification was performed. What we observed the PDCoV S L399Q, R401N and M354I-I391V-N397K do not drastically impact the state of S protein as we see one class of the spike protein. In contrast, for PDCoV S harboring R357W/Y we start seeing different classes of spike protein reminiscent of what appears to be cleavage of the Spike protein into S1 and S2 (Figure 2.8.2). It is possible that these mutations cause drastic changes in how the spike protein packs at the S1 domain leading to opening and thereby instability and cleavage of the spike protein. Structural analysis of these residues provides some insight into the possible ways in which these mutations could impact the packing and conformation of the RBD in context of the spike trimer (Figure 2.8.3). R357W/Y which in the context of the RBD did not bind APN orthologs when present on the spike protein we hypothesize leads to opening of the spike thereby leading to enhanced viral entry across all APN orthologs with no specificity. Further studies are needed to support this hypothesis.

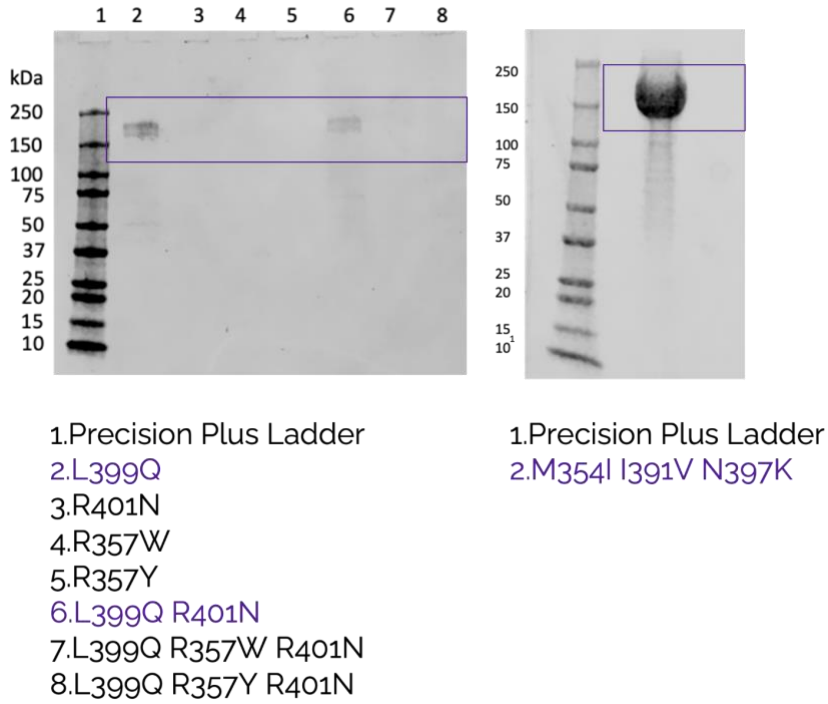

Figure 2.8.1. PDCoV S DMS mutants glycoprotein expression

Figure 2.8.2. PDCoV S DMS mutants negative stain and 2D Classification

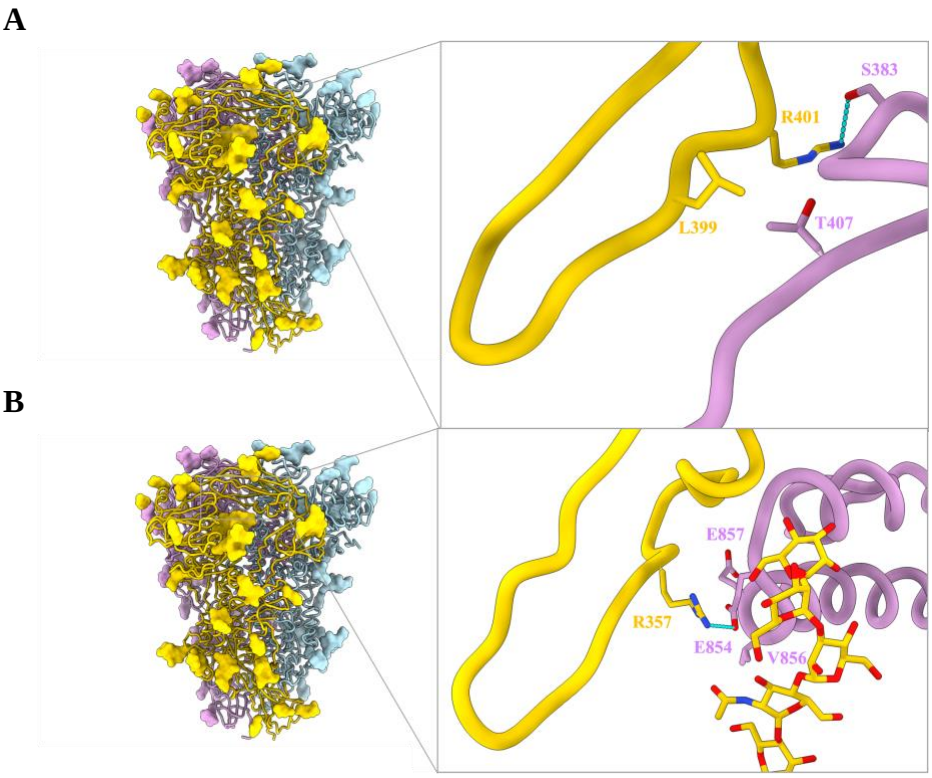

Figure 2.8.3. Structural view of PDCoV S harboring DMS mutation sites. A, Structure of PDCoV S trimer (blue, gold, and pink) and a zoom in view of residues L399, and R401 with side chains shown as sticks. Intramolecular hydrogen bond interactions between the PDCoV S R401 from one monomer and S383 from a second monomer are shown as blue dashed lines. **B,** Structure of PDCoV S trimer and a zoom in view of residue R357 from one monomer forming a salt bridge with E854 from a second monomer shown as blue dashed lines.

2.9. Discussion

The RBD of PDCoV is under high selective pressure as the main driver of viral entry. Lessons from SARS-CoV-2 have demonstrated the mutational landscape at the RBD-host receptor interface to be tolerant of substitutions, resulting in a plethora of circulating and highly infectious variants with accumulating mutations that can escape immune surveillance (3, 4). In light of our structural analysis, we observed a high level of conservation among mammalian and avian receptor binding by PDCoV RBD loops 1-3. We wanted to understand the extent of plasticity of the RBD binding loops in order to predict the rise of future variants that could evade antibody-mediated viral neutralization. We found through DMS favorable enhancing mutations that could be beneficial to the virus and potentially arise through natural selection to lead to a more infectious variant of PDCoV. This merits the development of countermeasures against PDCoV circulating variants and possible escape variants.

2.10. Methods

Production of recombinant PDCoV S glycoproteins

The PDCoV S glycoprotein ectodomains were cloned into pcDNA3.1+ plasmid by GenScript with the host N-terminal signal peptide sequence, C-terminal foldon domain, thrombin cleavage sequence, short linker of GSG, AVI tag and 8 x His tag. The DNA constructs were expanded using DH5α cells and purified using Qiagen MegaPrep Kit. Protein was expressed using ExpiFectamine 293 Transfection Kit (Thermo Fisher Scientific). Expi293F cells were grown at 37℃ with 8% CO_2 to 3E6 cells and transfected with 100µg of DNA. Cell culture supernatants were harvested four days post-transfection. Protein was purified using HisTrap^{Tm} High Performance column (Cytiva). Protein was bound to HisTrap resin in 50mM Tris-HCl, 150mM NaCl, 10mM Imidazole at pH 8.0. Unbound proteins were washed in 10 column volumes of 50mM Tris-HCl, 150mM NaCl, 10mM Imidazole at pH 8.0. Eluted with 50mM Tris, 150mM NaCl, 250 mM Imidazole at pH 8.0. The eluted S protein was concentrated using Amicon Ultra-15 Centrifugal Filter Unit (100kDa) and buffer exchanged into 50mM Tris, 150mM NaCl pH 8.0. Endotoxin levels were assessed using Charles River Limulus Amebocyte Lysate (LAL) cartridges. Proteins were snap frozen in liquid nitrogen and stored at -80℃.

Production of recombinant PDCoV RBDs

The PDCoV RBDs spanning residues 303-415 were cloned into pcDNA3.1+ plasmid by GenScript with an N-terminal mu-phosphatase signal peptide sequence and C-terminal short linker GSG, AVI tag and 8 x His tag. The DNA constructs were expanded using DH5α cells and purified using Qiagen MegaPrep Kit. Protein was expressed using ExpiFectamine 293 Transfection Kit (Thermo Fisher Scientific). Expi293F cells were grown at 37℃ with 8% CO_2 to 3E6 cells and transfected with 100 µg of DNA. Cell culture supernatants were harvested four days post-transfection. Protein was purified using HisTrap^{Tm} High Performance column (Cytiva). Protein was bound to HisTrap resin in 50mM Tris-HCl, 150mM NaCl, 10mM Imidazole at pH 8.0. Unbound proteins were washed in 10 column volumes of 50mM Tris-HCl, 150mM NaCl, 10mM Imidazole at pH 8.0. Eluted with 50mM Tris-HCl, 150mM NaCl, 250 mM Imidazole at pH 8.0. The eluted RBD was concentrated using Amicon Ultra-15 Centrifugal Filter Unit (10 kDa) and buffer exchanged into 50mM Tris, 150mM NaCl pH 8.0 and further purified using size exclusion chromatography Superdex 200 10/300. Endotoxin levels were assessed using Charles River Limulus Amebocyte Lysate (LAL) cartridges. Proteins were snap frozen in liquid nitrogen and stored at -80℃.

Production of recombinant APN ectodomain

The APN ectodomains were cloned into pcDNA3.1+ plasmid by GenScript with an N-terminal mu-phosphatase signal peptide sequence and C-terminal short linker GGS, thrombin cleavage site,

human Fc fragment. The DNA constructs were expanded using DH5α cells and purified using Qiagen MegaPrep Kit. Protein was expressed using ExpiFectamine 293 Transfection Kit (Thermo Fisher Scientific). Expi293F cells were grown at 37℃ with 8% CO_2 to 3E6 cells and transfected with 100 µg of DNA. Cell culture supernatants were harvested four days post-transfection. Protein was purified using HighTrap Protein A column (Cytiva). Protein was bound to resin in 50mM Tris-HCl, 150mM NaCl pH 8.0. Unbound proteins were washed in 10 column volumes of 50mM Tris-HCl, 150mM NaCl at pH 8.0. Eluted with 0.1 M Citric Acid (pH 3.0) and neutralized with 1 M Tris-HCl (pH 9.0). The eluted APN was buffer exchanged into 50mM Tris, 150mM NaCl pH 8.0 and further purified using size exclusion chromatography Superdex 200 Increase 10/300 GL. Protein was concentrated using the Amicon Ultra-15 Centrifugal Filter Unit (100 kDa). Proteins were snap frozen in liquid nitrogen and stored at -80℃.

Production of VSV pseudoviruses

PDCoV S glycoprotein constructs containing a C-terminal deletion of 21 residues to improve exportation to the membrane followed by a Flag tag were cloned into pcDNA3.1+ by GenScript. HEK293T cells were seeded at 16E6 cells in 100 mm dishes (Corning) poly-D-Lysine coated. Cells were transfected with 24 µg of DNA and 60 µL of Lipofectamine 2000 (Thermo Fisher Scientific) in Opti-MEM transfection medium. Post 5 hour incubation DMEM containing 20% FBS and 2% PenStrep was added to the cells. After 21 hours at 37 °C with 5% CO_2 the cells are washed 1x with DMEM and infected with VSV (G∗ΔG-luciferase) in DMEM for 2 hours. The cells are washed 2x with DMEM and anti-VSV G antibody (I1-mouse hybridoma supernatant diluted 1:40 in DMEM, ATCC CRL-2700) is added and incubated for 24 hours at 37 °C with 5% CO_2. Pseudovirus is harvested and collected by centrifugation at 3,000xg for 10 min. Supernatant containing the pseudovirus is filtered using a 0.45 µm syringe filter and concentrated 5x prior to storage at -80°C. Mock VSV pseudoviruses were prepared as above but without S glycoprotein transfection.

Western Blot Analysis of VSV pseudoviruses

Western blot analysis was performed to determine the levels of S glycoprotein for each of the VSV pseudoviruses. 30 µL of virus is obtained and mixed with 10 µL of 4x LDS sample reducing buffer. Samples were boiled at 95 °C for 5 minutes and spun down. 35 µL of final mixture was run on 4-20% Mini-Protean TGX precast protein gel at 150 Volts for 45 minutes. Proteins were transferred using Trans-Blot Turbo Mini 0.2 µm PVDF Transfer Packs and membranes were incubated with Intercept (TBS) Blocking Buffer (Licor) for 1 hour at room temperature. Anti-Fusion peptide antibody at 1 µg/ml was diluted in Intercept (TBS) Antibody Diluent Buffer (Licor) and incubated at 4°C overnight. The following day membranes were washed with TBST 3x with 5-minute incubations at room temperature. Anti-human Fc (Jackson ImmunoResearch) was diluted 1:50,000 in Intercept (TBS) Antibody Diluent Buffer (Licor) and membranes were incubated at room

temperature for 1 hour. Membranes were washed with 3x TBST with 5 minute incubations at room temperature. Images were taken using the Licor Odyssey CLx.

Cell entry assays

HEK293T cells were transiently transfected with APN orthologs. APN orthologs with a C-terminal Flag tag were cloned into pcDNA3.1+ by GenScript. HEK293T cells seeded at 16E6 cells in 100 mm dishes coated with poly-D-Lysine and incubated overnight at 37 °C with 5% CO_2. The following day cells were transfected with 8 μg of DNA using 30 μL of Lipofectamine 2000 transfection kit in Opti-MEM. Post 5 hours of incubation with transfection reagent, cells were trypsinized with 0.05% Trypsin EDTA for 3 minutes and neutralized with DMEM with 10% FBS 1% penicillin–streptomycin. 40,000 cells were seeded in 96-well plates (Corning 3610) coated with poly-lysine (Sigma P4707) and allowed to incubate at 37 °C with 5% CO_2. Following day, media was removed and 20 μL of DMEM was added followed by 20 μL of VSV pseudotyped with PDCoV S variants for 2 hours at 37 °C with 5% CO_2. Cells were supplemented with 40 μL of DMEM containing 20% FBS and 2% PenStrep and incubated for 22 hours at 37 °C with 5% CO_2. 40 μL of One-Glo-EX substrate (Promega) was added and cells were incubated at 37 °C for 10 minutes with shaking. Luminescence was read using BioTek Neo2 plate reader. Technical replicates of three were run for three different lots of pseudovirus for each variant. Luciferase units were plotted using Graphpad Prism.

Biolayer interferometry analysis (BLI)

BLI binding assays were performed on an Octet Red (Sartorius) instrument operated at 30°C with shaking (1000 rpm). Nickel-NTA biosensor tips were hydrated in 10 x Kinetics Buffer for 10 minutes at room temperature. PDCoV RBD-His was loaded at 10 μg/ml in 10 x Kinetics Buffer to 1 nm. Loaded tips were dipped into a 10x Kinetics buffer to stabilize and remove any unbound protein for 60 seconds. Loaded RBD tips were dipped into APN orthologs for 360 seconds. Associated APNs bound to the RBD was preceded by a dissociation phase of tips being moved into a 10x kinetics buffer for 360 seconds. $KD_{apparent}$ determination of RBD to APN-Fc was obtained through a concentration series starting at 5 μM and titrated down by two fold down to 39 nM. K_D values were calculated using ForteBio data analysis software where fitting of curves using a 1:1 binding model was used.

Cryo-EM sample preparation and data collection

For gAPN bound PDCoV RBD structure, PDCoV RBD was complexed with gAPN tagless for 1 hour at 4°C. 3ul of complex were directly applied to freshly glow discharged UltrAuFoil 300 1.2/1.3 grids. The Cryo-EM grids were prepared using a Vitrobot Mark IV (Thermo Fisher Scientific) with R 2/2 UltrAuFoil grids and a Chameleon[55] (SPT Labtech) with self-wicking

nanowire Cu R1.2/0.8 holey carbon grids. The grids were blotted with a blot force of -1, 6 second blot time and 10 second wait time before plunge freezing using a vitrobot MarkIV (ThermoFisher Scientific) set at 100% humidity and 4 °C. Data were acquired using an FEI Titan Krios transmission electron microscope operated at 300 kV and equipped with a Gatan K3 direct detector and Gatan Quantum GIF energy filter operated in zero-loss mode with a slit width of 20 eV. Automated data collection was carried out using Leginon at a nominal magnification of 105,000 with a pixel size of 0.835 Å and total exposure dose of 58 e/A. 13,767 micrographs from UltrAuFoil[57] grids and 13,733 micrographs from chameleon grids were collected with a defocus range between -0.2 and -3.0 μm. Each movie was fractionated in 100 frames of 40 ms each.

Cryo-EM data processing, model building and refinement

The raw movie data sets were processed using motion correction, contrast-transfer function (CTF) parameter estimation, automatic particle picking, and extraction using RELION motion correction, contrast-transfer function (CTF) parameter estimation, particle picking, and extraction using cryoSPARC. Particle images were extracted with a box size of 512 downsampled to 256 pixels and a pixel size of 0.828Å. After two rounds of 2D classification using cryoSPARC, well-defined 465,175 particles were selected and processed through non-uniform refinement (NUR). Particle polishing was performed using RELION. Imported particles were processed once more through NUR. Chimera, ChimeraX and Coot were used to fit atomic models into the cryo-EM maps. Structure was refined and relaxed using Rosetta using sharpened and unsharpened maps and validated using Phenix and Molprobity. Analysis of interface residues was assisted by PISA.

Chapter 3: Identification of broadly neutralizing antibodies against emerging delta-coronaviruses

3.1. Abstract

Porcine deltacoronavirus (PDCoV) spillovers were recently detected in children with acute undifferentiated febrile illness, underscoring recurrent zoonoses of divergent coronaviruses. To date, no vaccines or specific therapeutics are approved for use in humans against PDCoV. To prepare for possible future PDCoV epidemics, we isolated human spike (S)-directed monoclonal antibodies from transgenic mice and found that two of them, designated PD33 and PD41, broadly neutralized a panel of PDCoV variants. Cryo-electron microscopy structures of PD33 and PD41 in complex with the PDCoV receptor-binding domain and S ectodomain trimer provide a blueprint of the epitopes recognized by these mAbs, rationalizing their broad inhibitory activity. We show that both mAbs inhibit PDCoV by competitively interfering with host APN binding to the PDCoV receptor-binding loops, explaining the mechanism of viral neutralization. PD33 and PD41 are candidates for clinical advancement, which could be stockpiled to prepare for possible future PDCoV outbreaks.

3.2. Introduction

Coronaviruses (CoVs) are positive-strand enveloped RNA viruses that cause mild to deadly respiratory and enteric disease in avian and mammalian species. *Alpha*-CoVs, 229E[1] and NL63[2], along with *Beta-CoVs,* HKU1[3] and OC43[4], are endemic in humans and mainly associated with mild respiratory infections (common colds), although some cases lead to severe illness, particularly for children, the elderly and immunocompromised individuals. All three highly pathogenic human CoVs belong to the *Beta*-CoV genus and led to two epidemics, mediated by SARS-CoV-1[5–8] and MERS-CoV[9], and the COVID-19 pandemic caused by SARS-CoV-2[10,11].

CCoV-HuPn-2018 and the closely-related HuCCoV_Z19Haiti, which are canine-feline recombinant alphacoronaviruses, were recently identified in patients with pneumonia or acute respiratory symptoms[12–14]. Porcine delta-coronavirus (PDCoV) was shown to be able to use human APN for cell entry and was recently associated with multiple zoonotic transmission events in children with acute undifferentiated febrile illness[15,16]. These spillovers underscore that more coronaviruses than previously appreciated currently circulate in humans and the zoonotic threats posed by coronaviruses from distinct genera.

The coronavirus spike (S) glycoprotein forms homotrimers anchored in the viral membrane to mediate attachment to host receptors and membrane fusion for initiating infection[17–20]. S plays a key role in modulating host and tissue tropism, zoonotic transmission and pathogenesis[21–23]. Given that S is a main target of antibodies and that neutralizing antibody titers are a correlate of protection

against coronaviruses, development of vaccines and therapeutics focuses intensively on this glycoprotein target[24–28].

Here, we report the isolation of human monoclonal antibodies (mAbs) targeting the PDCoV S receptor-binding domain (RBD) from transgenic mice and show that two of them (PD33 and PD41) broadly neutralize a panel of divergent PDCoV isolates harboring S mutations. Cryo-electron microscopy (cryoEM) analysis of the P33 Fab fragment bound to the PDCoV RBD and of the PD41 Fab bound to a variant PDCoV S trimer provide a blueprint of the interactions mediating recognition and broad neutralization. We demonstrate that both mAbs inhibit APN receptor binding to PDCoV S competitively, explaining their mechanism of broad inhibition. PD33 and PD41 are promising candidates for future clinical advancement individually or as a cocktail for mAb therapy.

3.3. Discovery of broadly neutralizing PDCoV monoclonal antibodies (mAbs)

To identify neutralizing antibodies with therapeutic potential, we immunized Alloy ATX transgenic mice harboring the human immunoglobulin loci encoding for the heavy chain and either the lambda (ATX-GL) or the kappa (ATX-GK) light chain. Two ATX-GL and two ATX-GK mice were immunized alternatively with the PDCoV Illinois strain (IL121_2014) RBD and prefusion-stabilized 2P $PDCoV_{IL121\_2014}$ S for a total of 4 doses (**Figure 3.3.1A**). Mice were sacrificed 8 days after last boost and peripheral blood, spleen and lymph nodes (LN) were collected and cells freshly isolated. $PDCoV_{IL121\_2014}$ RBD-specific memory B cells were selected from immunized mice via fluorescence-assisted cell sorting and VH/VL sequences subsequently retrieved by RT-PCR.

Biolayer interferometry (BLI) and ELISA screening led to the identification of eighteen S-directed mAbs, nine of which binding to the RBD, and all of them were screened for neutralization of a vesicular stomatitis virus (VSV) pseudotyped with $PDCoV_{IL121\_2014}$ S using HEK293T target cells transiently transfected with galline APN (gAPN) (**Figure 3.3.2A-C**). Four mAbs, designated PD17, PD20, PD33 and PD41, had neutralizing activity with half-maximal inhibitory concentrations (IC_{50}) below 1 μg/ml with PD33 and PD41 endowed with the greatest potency (**Figure 3.3.1B and Figure 3.3.2D**). PD33 and PD41 Fab fragments bound with faster on rates and/or slower off rates to the immobilized $PDCoV_{IL121\_2014}$ RBD, relative to PD17 and PD20, with respective binding affinities of ~5 nM and ~30 nM (**Figure 3.3.1C-D, Figure 3.3.3 and Table 3.3.1**). Based on these data, PD33 and PD41 were selected as lead PDCoV S-directed antibodies for further characterization.

To investigate the breadth of neutralization mediated by these mAbs, we evaluated their ability to neutralize a panel of VSV pseudotyped with PDCoV S-related isolates harboring mutations in the RBD in presence of the PD33 and the PD41 mAbs using HEK293T target cells transiently transfected with human APN (hAPN). Our panel also included a VSV pseudotyped with the S

glycoprotein of the PDCoV isolate identified in humans, which harbor the P8A and V550A residue substitutions. We observed that PD33 and PD41 broadly neutralized our panel of pseudoviruses demonstrating their broad neutralizing activity (**Figure 3.3.1E-F and Figure 3.3.4 A-C**).

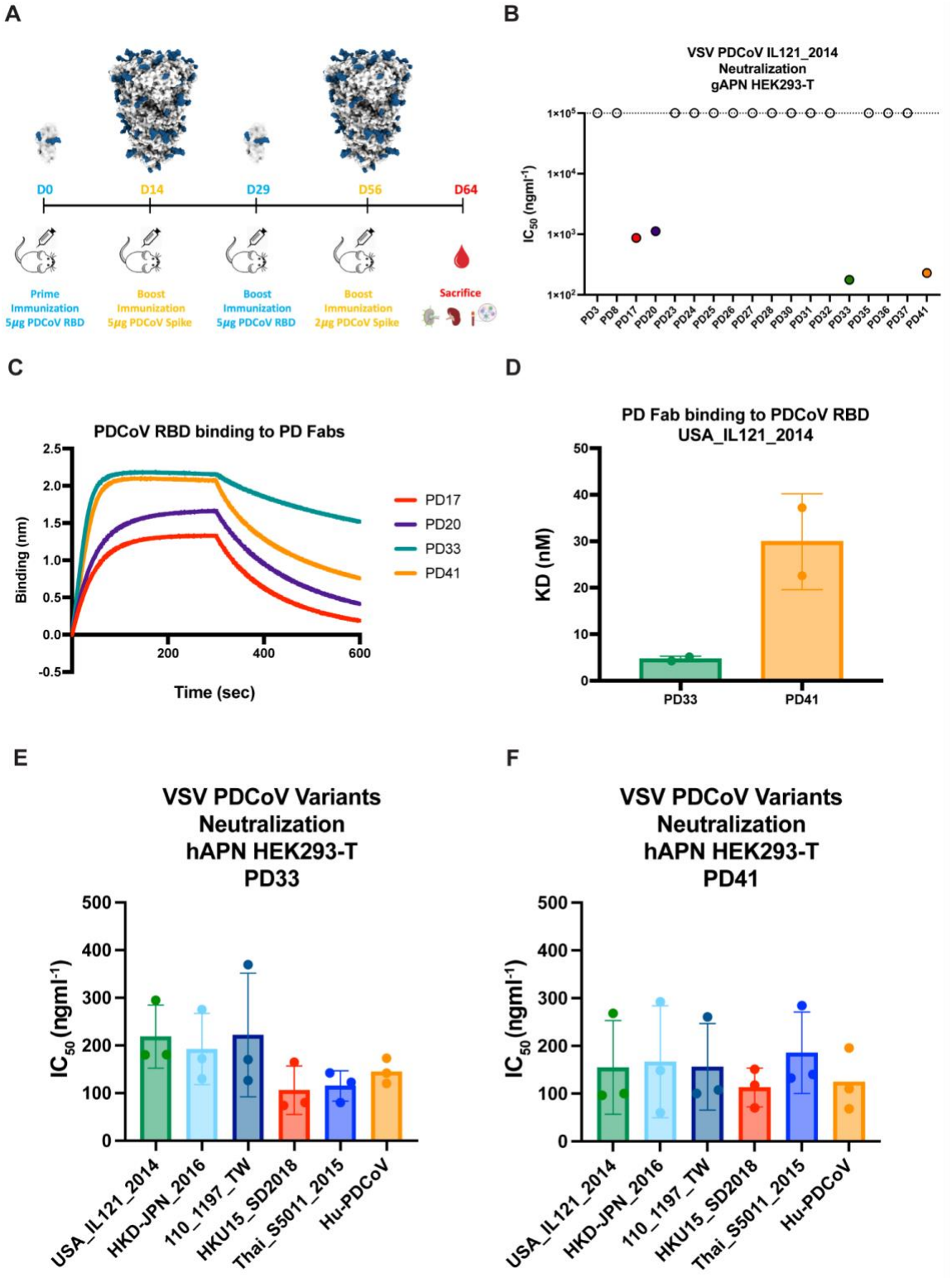

Figure 3.3.1: Discovery and characterization of broadly neutralizing PDCoV monoclonal antibodies (mAbs). A, Immunization study of ATX mice with PDCoV S and RBD. **B,** Screening of isolated mAbs for neutralization of VSV pseudotyped with PDCoV S using HEK293T cells transfected with the galline APN (gAPN) receptor. Four neutralizing antibodies PD17, PD20, PD33 and PD41 were selected for further characterization. **C,** Biolayer interferometry (BLI) analysis of PDCoV $RBD_{USA\_IL121\_2014}$ binding to neutralizing antibodies PD17, PD20, PD33, and PD41 Fab fragments. **D,** Binding affinities of the PD33 and the PD41 Fab to PDCoV $RBD_{USA\_IL121\_2014}$ (dose-response curves are shown in Figure 3.3.2). **E-F,** PD33 (E) and PD41 (F) mAb-mediated neutralization of VSV pseudotyped with PDCoV S variants using HEK293T target cells transfected with human APN (hAPN). The bars correspond to geometric mean titers and each data point is one out of 3 biological replicates, each one using a different batch of pseudovirus.

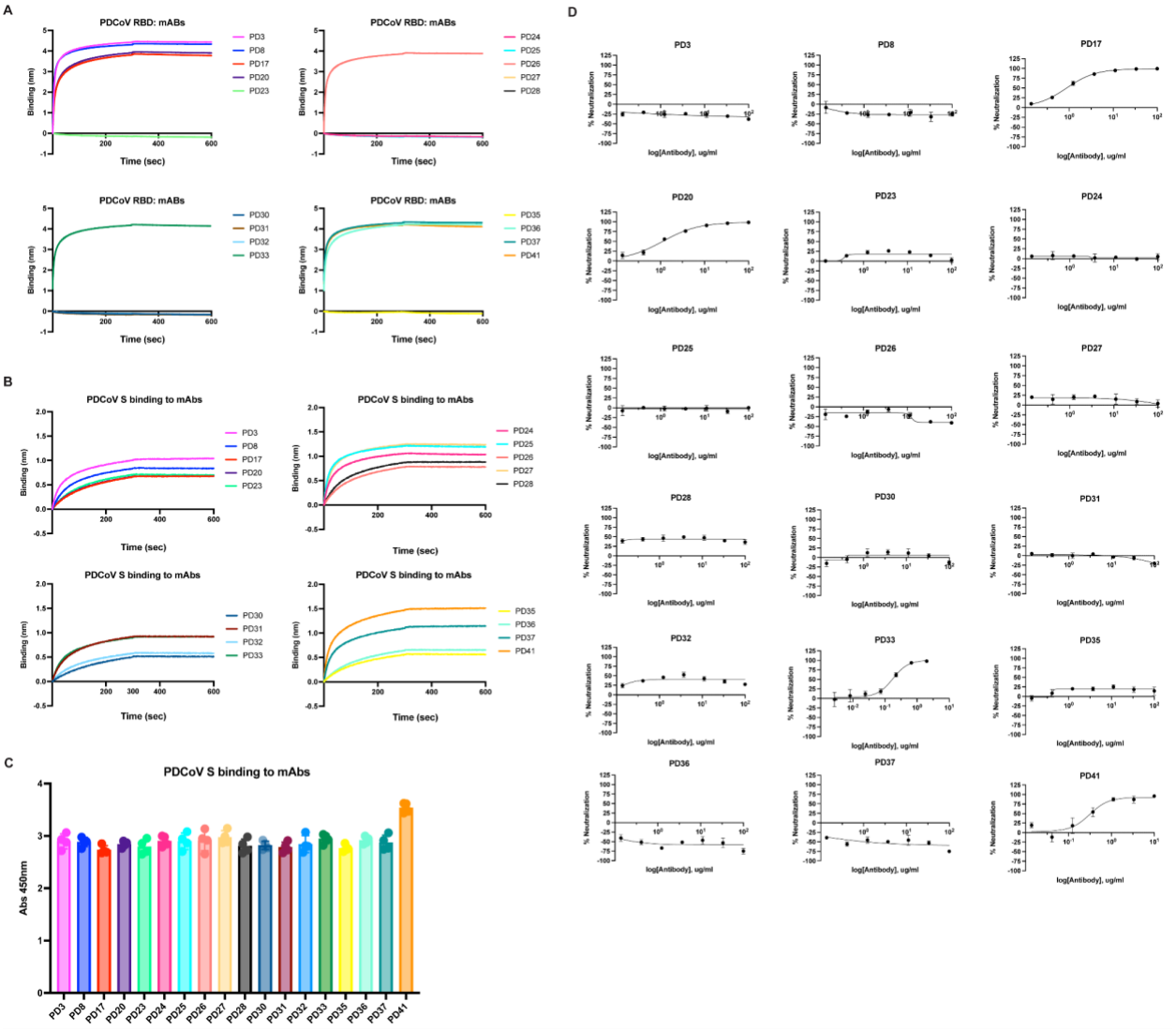

Figure 3.3.2. Screening for binding and neutralization of a panel of human mAbs (PD3, PD8, PD17, PD20, PD23, PD24, PD25, PD26, PD27, PD28, PD30, PD31, PD32, PD33, PD35, PD36,

PD37, PD41) isolated from transgenic mice. A, Screening of isolated mAbs for binding to PDCoV RBD immobilized at the surface of BLI biosensors. **B,** Screening of isolated mAbs immobilized at the surface of BLI biosensors for binding to PDCoV S **C,** Evaluation of binding of the isolated mAbs to PDCoV S measured by ELISA. Each point represents the mean of technical quadruplets. Standard deviations shown as error bars. **D,** Dose-dependent mAb-mediated neutralization of PDCoV S VSV using HEK293T target cells transiently transfected with galline APN (gAPN). Each point represents the mean of technical triplicates. Standard deviations shown as error bars.

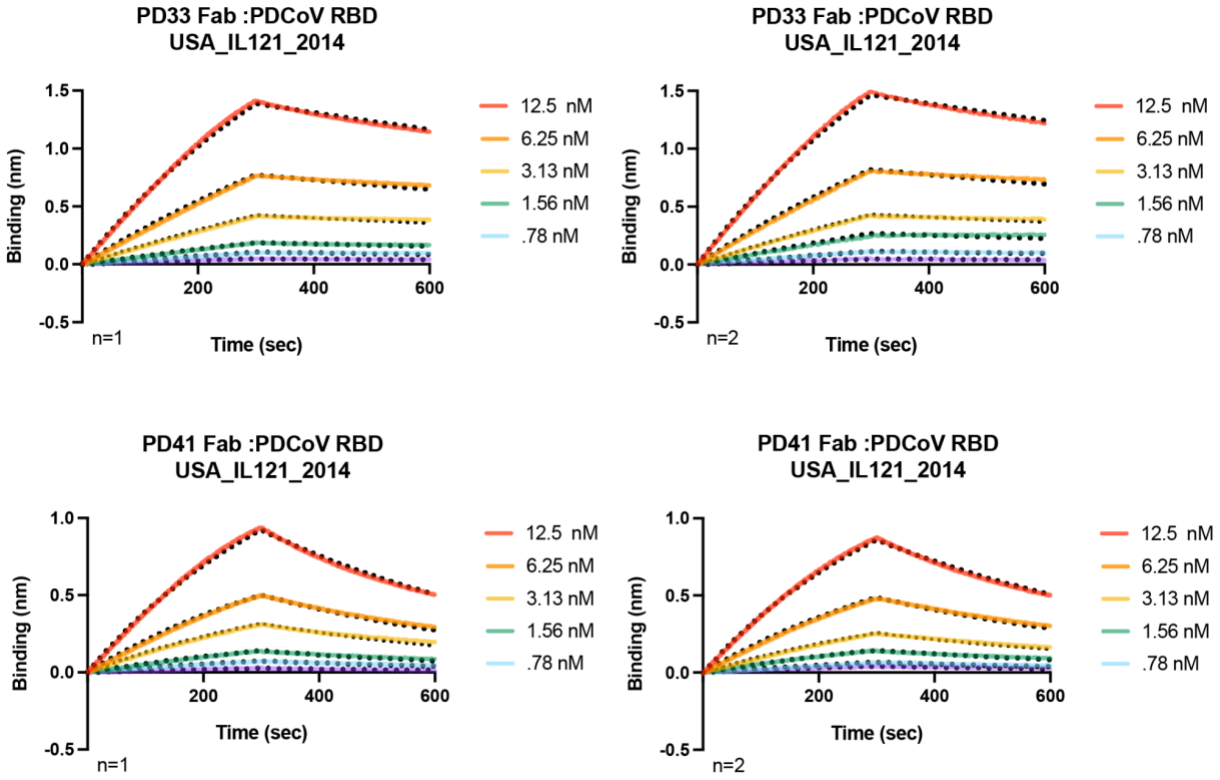

Figure 3.3.3: Kinetics of PD33 and PD41 Fabs binding to PDCoV RBD. BLI analysis of PD33 and PD41 Fab fragments binding to immobilized $PDCoV_{IL121\_2014}$ RBD immobilized onto Ni-NTA tips. Fits to the data are shown as black dotted lines and were used to determine the binding affinity (K_D) of the PD33 and PD41 Fab fragments to PDCoV RBD. Two biological replicates are shown for each Fab.

			K_D (M)	K_D Error	K_a (1/Ms)	K_a Error	K_{dis} (1/s)	K_{dis} Error
PDCoV RBD USA_IL121_2014	PD33	n=1	5.11E-09	4.57E-11	1.15E+05	9.45E+02	5.86E-04	2.05E-06
		n=2	4.36E-09	3.83E-11	1.24E+05	9.80E+02	5.42E-04	2.11E-06
	PD41	n=1	3.72E-08	6.94E-10	5.38E+04	1.00E+03	2.00E-03	2.49E-06
		n=2	2.26E-08	2.60E-10	7.84E+04	8.98E+02	1.77E-03	2.18E-06

Table 3.3.1. Table of the KDs, association (K_a) and dissociation rate constants (K_{dis}) for duplicate lots of PDCoV RBD_{IL121_2014} and Fab fragments of PD33 and PD41.

A

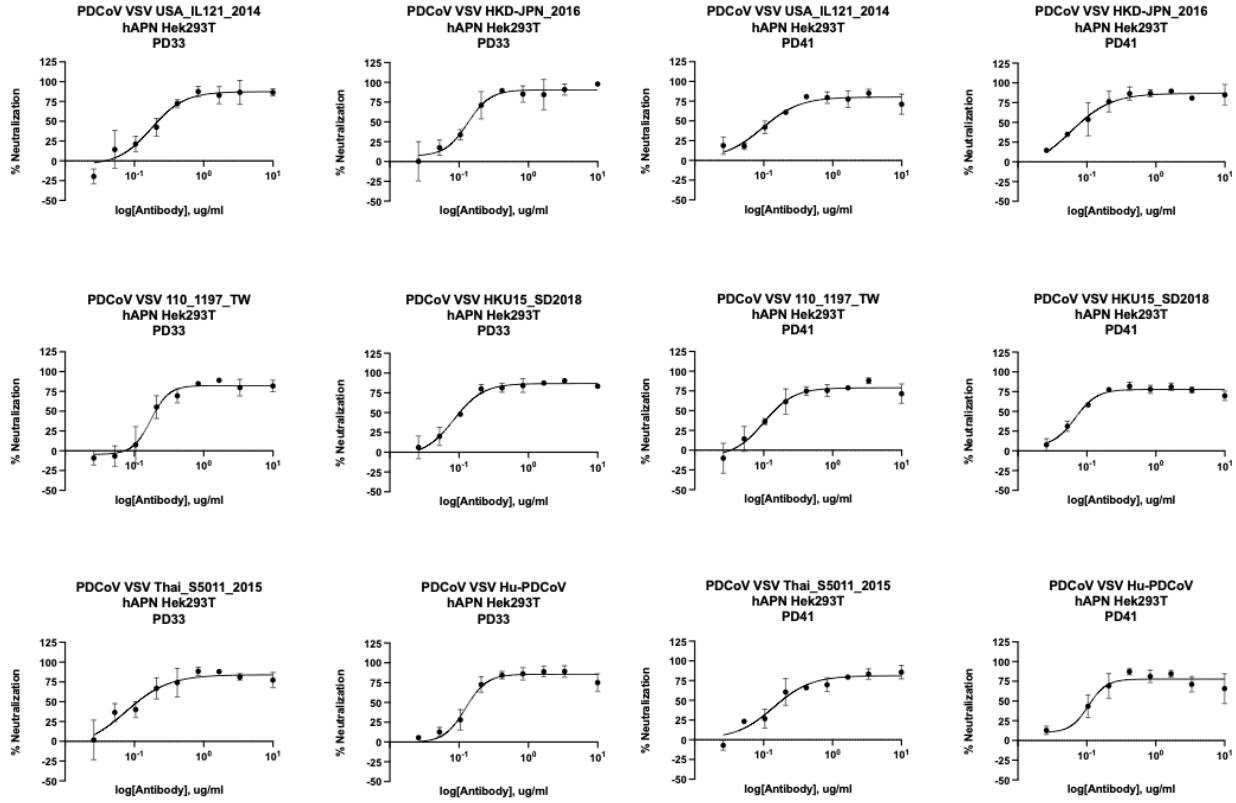

n=1

B

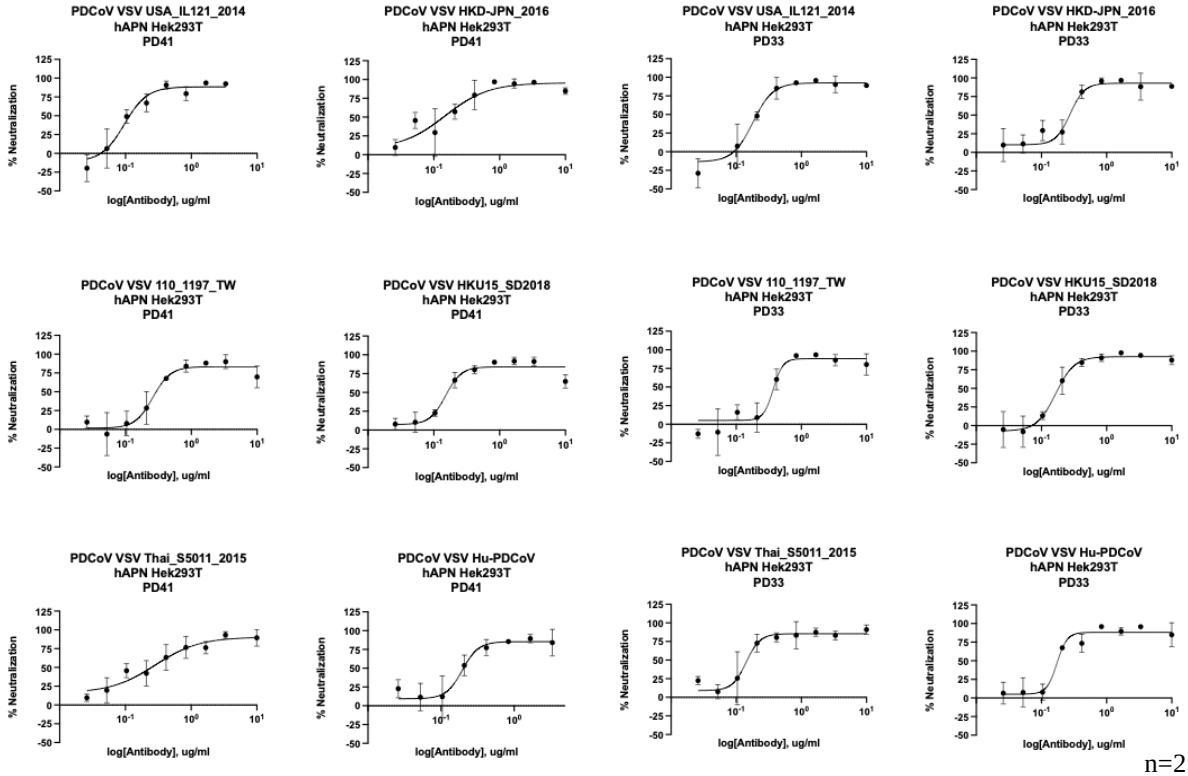
PDCoV VSV USA_IL121_2014 hAPN Hek293T PD41
PDCoV VSV HKD-JPN_2016 hAPN Hek293T PD41
PDCoV VSV USA_IL121_2014 hAPN Hek293T PD33
PDCoV VSV HKD-JPN_2016 hAPN Hek293T PD33
PDCoV VSV 110_1197_TW hAPN Hek293T PD41
PDCoV VSV HKU15_SD2018 hAPN Hek293T PD41
PDCoV VSV 110_1197_TW hAPN Hek293T PD33
PDCoV VSV HKU15_SD2018 hAPN Hek293T PD33
PDCoV VSV Thai_S5011_2015 hAPN Hek293T PD41
PDCoV VSV Hu-PDCoV hAPN Hek293T PD41
PDCoV VSV Thai_S5011_2015 hAPN Hek293T PD33
PDCoV VSV Hu-PDCoV hAPN Hek293T PD33
% Neutralization
log[Antibody], ug/ml

n=2

C.

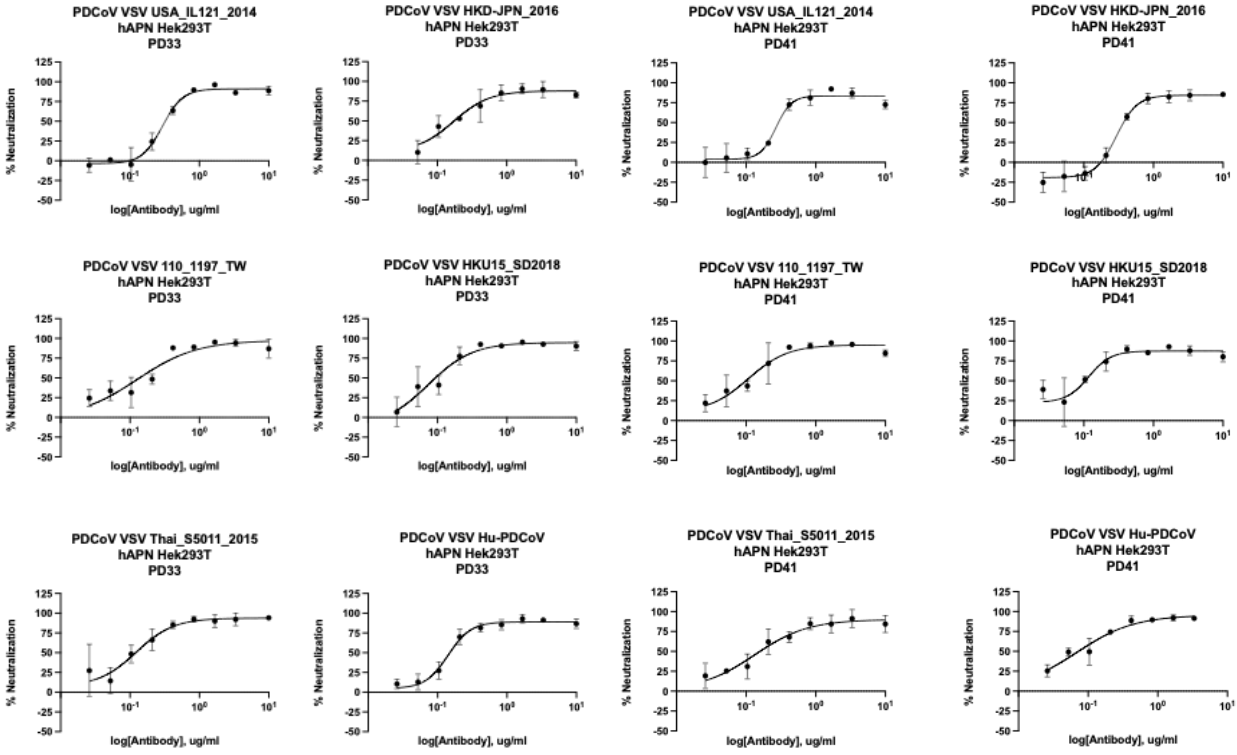
PDCoV VSV USA_IL121_2014 hAPN Hek293T PD33
PDCoV VSV HKD-JPN_2016 hAPN Hek293T PD33
PDCoV VSV USA_IL121_2014 hAPN Hek293T PD41
PDCoV VSV HKD-JPN_2016 hAPN Hek293T PD41
PDCoV VSV 110_1197_TW hAPN Hek293T PD33
PDCoV VSV HKU15_SD2018 hAPN Hek293T PD33
PDCoV VSV 110_1197_TW hAPN Hek293T PD41
PDCoV VSV HKU15_SD2018 hAPN Hek293T PD41
PDCoV VSV Thai_S5011_2015 hAPN Hek293T PD33
PDCoV VSV Hu-PDCoV hAPN Hek293T PD33
PDCoV VSV Thai_S5011_2015 hAPN Hek293T PD41
PDCoV VSV Hu-PDCoV hAPN Hek293T PD41
% Neutralization
log[Antibody], ug/ml

n=3

Figure 3.3.4. Assessment of PD33 and PD41 neutralization breadth. Dose-dependent mAb-mediated neutralization of PDCoV S VSV variants using HEK293T target cells transiently transfected with human APN. **A-C** are three independent runs with 3 different batches of pseudovirus.

3.4. Molecular basis of broad PD33 mAb-mediated neutralization

To understand the mechanism underlying the broadly neutralizing activity of PD33 towards a panel of PDCoV S variants, we characterized a complex between the $PDCoV_{IL121\_2014}$ RBD and the PD33 Fab fragment using cryoEM. To expedite the structural determination process, we opted to use an anti-kappa light chain nanobody recognizing the Fab hinge region and rigidifying it while also augmenting the overall molecular mass[29]. Using this strategy, we determined an asymmetric cryoEM structure at 3.0 Å resolution of this ~80 kDa complex enabling model building and analysis of the contacts mediating Fab binding (**Figure 3.4.1, Figure 3.4.2 and Table 3.4.1**).

PD33 binding leads to burial of an average surface of 830 $Å^2$ at the interface between the epitope and the paratope through hydrogen bonding and shape complementarity involving the PDCoV RBD loops 1 and 3 and the Fab complementary determining loops (CDRs) H1-3, L1 and L3 (**Figure 3.4.1A**). The epitope is dominated by RBD loop 3 which accounts for two thirds of the surface buried at the interface with the PD33 paratope. The PD33 epitope comprises residues 316, 318-322 and 393-401. RBD loop 3 inserts at the interface between PD33 VH and VL through contacts dominated by the $W396_{IL121\_2014}$, $Y398_{IL121\_2014}$ and $R401_{IL121\_2014}$ side chains which are respectively hydrogen bonded to the PD33 VH Y105, W101 and N56 side chains (**Figure 3.4.1B**). Furthermore, the $Y394_{IL121\_2014}$ phenol is hydrogen bonded to the CDRL1 D33 and N35 side chains whereas the CDRL1 Y31 phenol is hydrogen bonded to the $T393_{IL121\_201}$ and $Y394_{IL121\_201}$ backbone carbonyls (**Figure 3.4.1B**). Extensive van der Waals interactions involving loop 3 $Y394_{IL121\_2014}$, $V395_{IL121\_2014}$, $W396_{IL121\_2014}$ and $Y398_{IL121\_2014}$ residues with surrounding CDRH2, CDRH3, CDRL1 and CDRL3 residues further strengthen binding. PD33 CDRH1-3 triangulate RBD loop1 via shape complementarity and hydrogen-bonding of the $F318_{IL121\_2014}$ backbone carbonyl and the CDRH2 T53 side chain hydroxyl as well as the $E320_{IL121\_2014}$ and the CDRH2 S54 side chains (**Figure 3.4.1C**). Strict conservation of epitope residues rationalizes the observed PD33-mediated broad neutralization of PDCoV variants with the $S_{SD2018/300}$ N397K substitution being the sole epitope variability among the strains analyzed (**Figure 3.4.1D**). Given that the RBD residue 397 side chain points away from the binding interface and that its backbone is hydrogen-bonded to the PD33 CDRH2 Y59 side chain hydroxyl, the N397K substitution does not affect recognition or neutralization (**Figures 3.3.1E and 3.4.1B**).

The PD33 epitope comprises residues that are buried and therefore inaccessible in the closed S trimer due to tertiary and quaternary interactions (**Figure 3.4.1D**). As a result, PD33 binding requires RBD opening, as it would be incompatible with the closed RBD conformation. This is

reminiscent of some SARS-CoV-1, SARS-CoV-2 and MERS-CoV antibodies that conformationally select for open RBDs and trigger S_1 shedding and refolding to the postfusion conformation via receptor-functional mimicry[30–34].

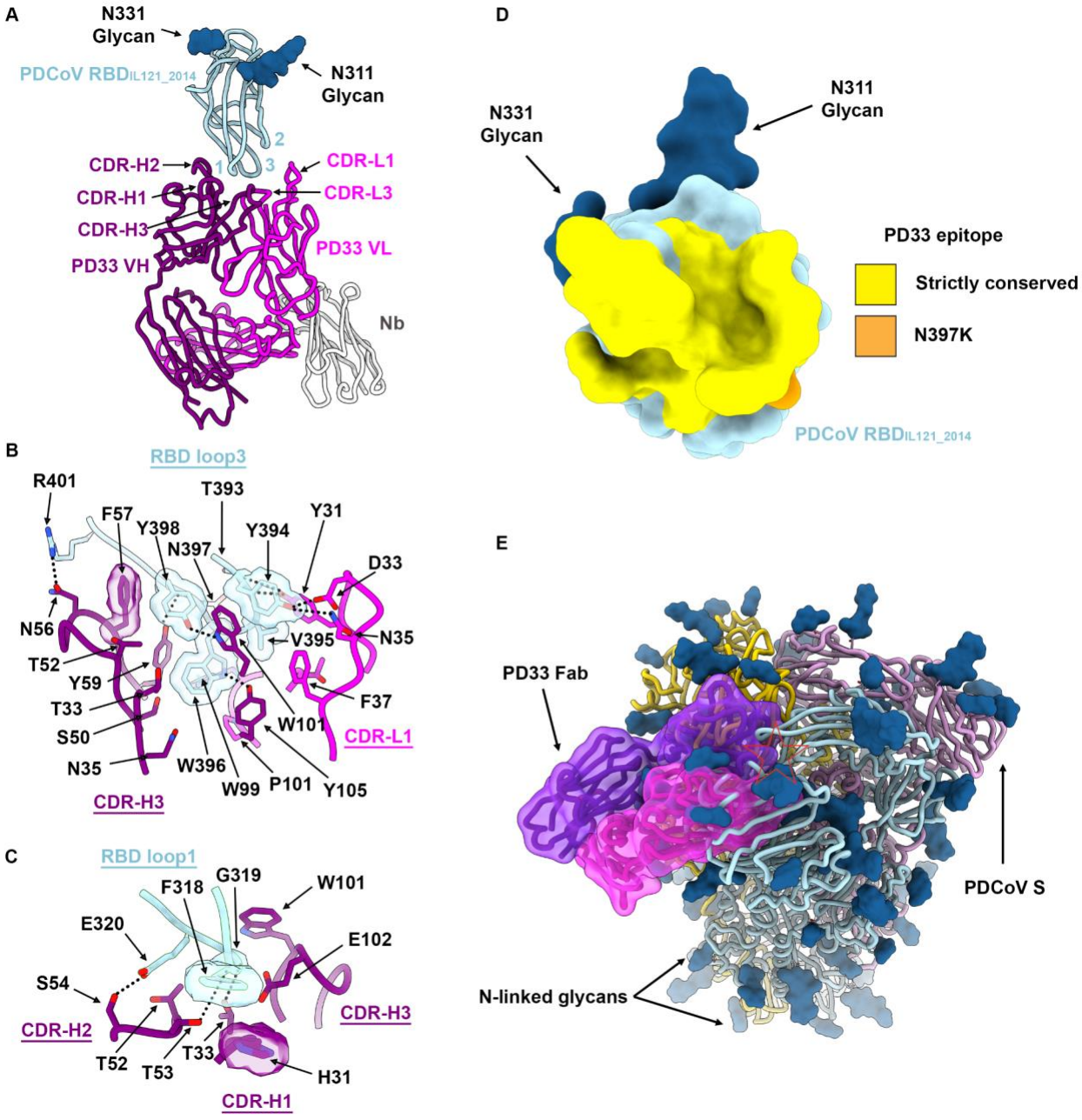

Figure 3.4.1: Molecular basis of broad PD33 mAb-mediated neutralization of PDCoV S variants. A, Ribbon diagram of the PD33 Fab-bound PDCoV RBD_{IL121_2014} cryoEM structure at 3.0Å resolution. PD33 $V_{H\ and}$ V_L are respectively rendered in purple and pink whereas the PDCoV RBD is colored cyan. The kappa light chain nanobody (Nb) used for assisting structural determination is shown in white. The PDCoV receptor-binding loops are annotated 1-3 and the

PD33 complementary determining regions (CDR) for light and heavy chains are annotated CDR-L1, 2, 3 and CHR-H1, 2, 3. N-linked glycans are rendered as blue spheres. **B-C,** Zoomed-in views of the interface between PDCoV RBD_{IL121_2014} loop 3 (B) or loop 1 (C) and the PD33 Fab. Selected hydrogen bonds and salt bridges are shown as black dashed lines. A few side chains are shown in surface representation to highlight shape complementarity. **D,** PD33 epitope conservation across the panel of PDCoV S variants analyzed. Yellow indicates strict residue conservation whereas orange shows the position of the N397K substitution present in $S_{SD2018/300}$. **E,** Superimposition of the PD33-bound PDCoV RBD structure with the PDCoV S ectodomain trimer structure (PDB 6BFU)[35] showing that PD33 could not bind to a closed S trimer due to masking of the receptor-binding loops and resulting steric clashes (red star).

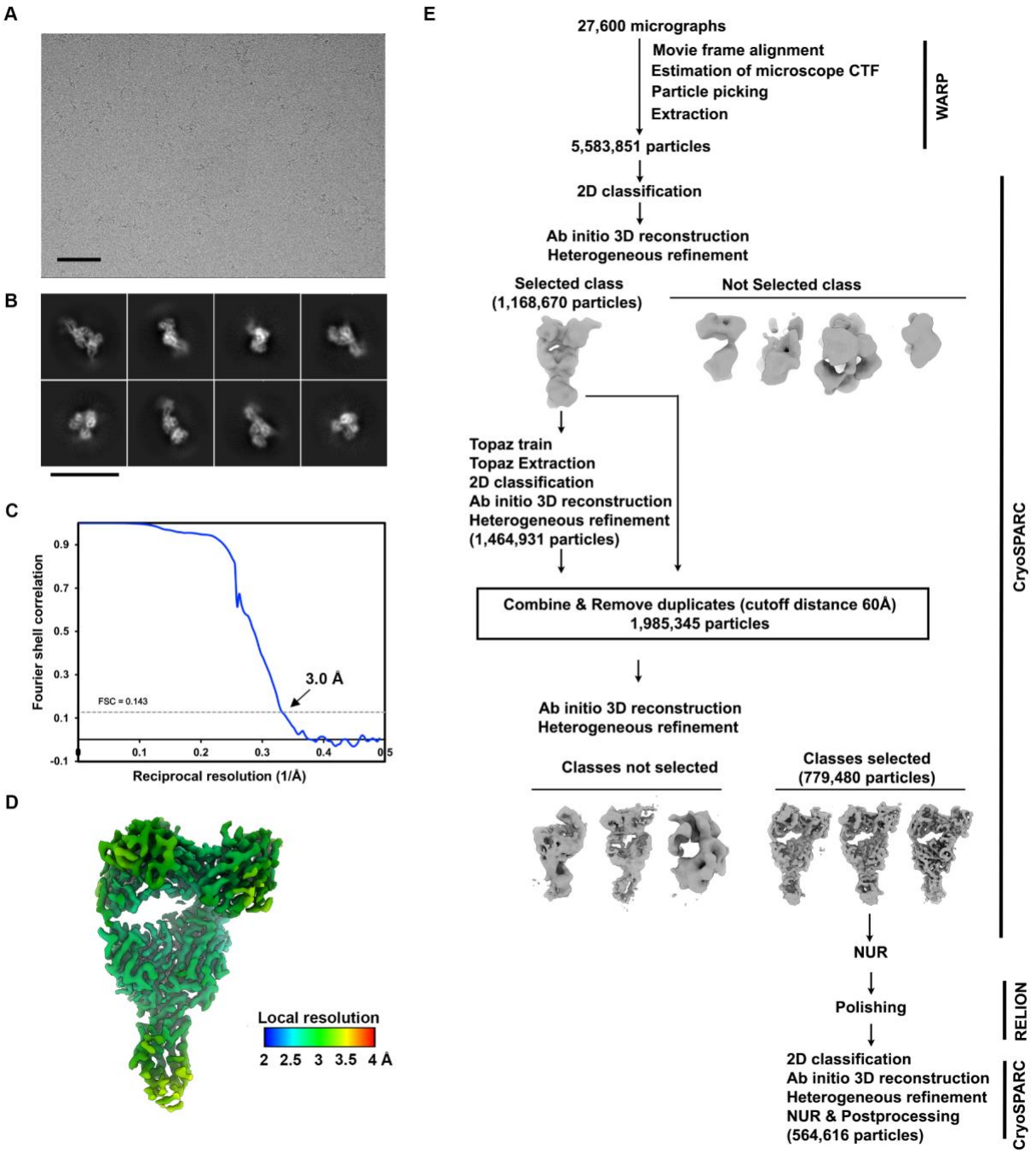

Figure 3.4.2: Cryo-EM data collection and refinement of PDCoV RBD$_{IL2014}$ bound to the PD33 Fab fragment. A, Representative electron micrograph (3.0 µm defocus, scale bar = 100 nm) **B,** 2D class averages (scale bar = 150 Å). **C,** Gold-standard Fourier shell correlation curve for the cryoEM reconstruction. The 0.143 cutoff is indicated with a gray dashed line. **D,** 3D reconstruction of PDCoV RBD bound to PD33 colored by local resolution calculated using CryoSPARC. **E,** Flow chart of the pipeline for processing. CTF: contrast transfer function; NUR: non-uniform refinement.

	PDCoV RBD with PD33	PDCoV Spike SD2018/300 Apo	PDCoV Spike SD2018/300 with one PD41 bound	PDCoV Spike SD2018/300 with PD41 (local refinement)	PDCoV Spike SD2018/300 with two PD41 bound	PDCoV Spike SD2018/300 with three PD41 bound
Data collection and processing						
Magnification	105,000	105,000	105,000	105,000	105,000	105,000
Voltage (kV)	300	300	300	300	300	300
Electron exposure (e^{-}/Å^2)	58	44.5	44.5	44.5	44.5	44.5
Defocus range (μm)	0.2 -3.0	0.8 -1.8	0.8 -1.8	0.8 -1.8	0.8 -1.8	0.8 -1.8
Pixel size (Å)	0.835	0.835	0.835	0.835	0.835	0.835
Symmetry imposed	C1	C3	C1	C1	C1	C1
Final particle images (no.)	564,616	24,642	465,175	465,175	99,272	26,452
Map resolution (Å)	3.0	3.1	2.72	3.0	3.0	3.4
FSC threshold	0.143	0.143	0.143	0.143	0.143	0.143
Map sharpening *B* factor (Å^2)	-139	-55.3	-85	- 87.8	-65.8	-38.8
Validation						
MolProbity score	1.73			0.87		
Clashscore	3.17			0.2		
Poor rotamers (%)	3.41			0		
Ramachandran plot						
Favored (%)	96.60			95.73		
Allowed (%)	99.23			99.39		
Disallowed (%)	0.77			0.61		

Table 3.4.1. CryoEM data collection and refinement statistics.

3.5. Molecular basis of broad PD41 mAb-mediated neutralization

To obtain a detailed understanding of PD41 mAb-mediated neutralization of a large panel of PDCoV-related isolates, we selected a PDCoV variant isolated from South Dakota in 2018 (S_{SD2018}) which harbor three RBD mutations (M354I, I391V, N397K) relative to RBD_{IL121_2014}. S_{SD2018} VSV exhibited the most efficient entry into HEK293T cells transiently transfected with human APN among the 6 isolates tested (**Figure 3.5.1**). Furthermore, the RBD_{SD2018} bound to human APN with a 5-fold greater affinity than that of RBD_{IL121_2014}, due to modulation of off-rates, similar to what has been observed for SARS-CoV-2 variants[36–39].

We characterized the complex between the PD41 Fab fragment and the S_{SD2018} ectodomain trimer using cryoEM and identified four distinct conformational states of the S glycoprotein by 3D classification : (i) class I with all three RBDs closed without any bound Fabs; (ii) class II with one Fab-bound RBD; (iii) class III with two Fab-bound RBDs, (iv) and class IV with three Fab-bound RBDs (**Figure 3.5.2A, Figure 3.5.3 and Table 3.5.1**). To improve the resolvability of the PD41/RBD interface, we used local refinement of class II to obtain a map focused on this region at 3.0Å resolution (**Figure 3.5.3**).

PD41 binding leads to burial of 615 $Å^2$ of the epitope and of the paratope surfaces through contacts involving all six CDR loops and the three PDCoV RBD loops through a combination of hydrogen bonds, salt bridges and shape complementarity (**Figure 3.5.2B)**. CDR H1 and H3 dominate the interface and account for two thirds of the buried surface upon PD41 binding along with most polar interactions. The PD41 epitope comprises residues 313-320, 322, 324, 348, 350-351 and 394. The RBD_{SD2018} inserts loop 1 $F318_{SD2018}$ side chain in a hydrophobic cavity formed at the interface between the PD41 VH and VL domains and its backbone amide group forms hydrogen bonds with the VH V102 backbone carbonyl and with the VH N103 side chain amide (**Figure 3.5.2C)**. Furthermore, RBD_{SD2018} loop 1 residues H315, D317, E320 and D324 form a hydrogen bond and salt bridge network with the CDRH1 Y35, CDRH2 Y54 and Y55, CDRH3 K100 and CDRL3 Y96 and Y99 side chains. Relative to loop 1, RBD loops 2 and 3 make more modest contributions to the epitope through contacts mediated by $T350_{SD2018}$ and $G351_{SD2018}$ as well as $Y394_{SD2018}$, respectively **(Figure 3.5.2D)**. Strict conservation of epitope residues rationalizes the observed PD41-mediated broad neutralization with the $S_{Thailand/S5011/2015}$ M348K and T350R substitutions being the sole epitope variability among the variants analyzed (**Figure 3.5.2E**). Although the M348 side chain points away from the interface with PD41, the T350 side chain is part of the interface and likely accommodated due to retained neutralization of this variant (**Figure 3.5.2D-E**).

The PD41 epitope comprises residues that are masked through tertiary and quaternary interactions in the context of the prefusion closed S trimer[35] and would preclude Fab binding (**Figure 3.5.2F**). As a result, PD41 binding requires structural rearrangements of the S trimer, such as opening of neighboring RBDs (as observed in our cryoEM structures with one and two bound PD41 Fabs) along with relative repositioning of the RBD and the NTD (as is the case in all our PD41 Fab-

bound structures) (**Figure 3.5.2A**). We note the binding geometry of PD41 to RBD places the Fab framework in the path of further NTD and neighboring RBD opening, and though the additional quaternary interactions of PD41 are individually too small to create strong binding, they sum to at least ⅓ of the buried surface area of the primary interface. PD41 might thereby transiently trap a prefusion trimer while ultimately driving S trimer dissociation, particularly when three PD41 Fabs are bound as in our cryoEM class IV.

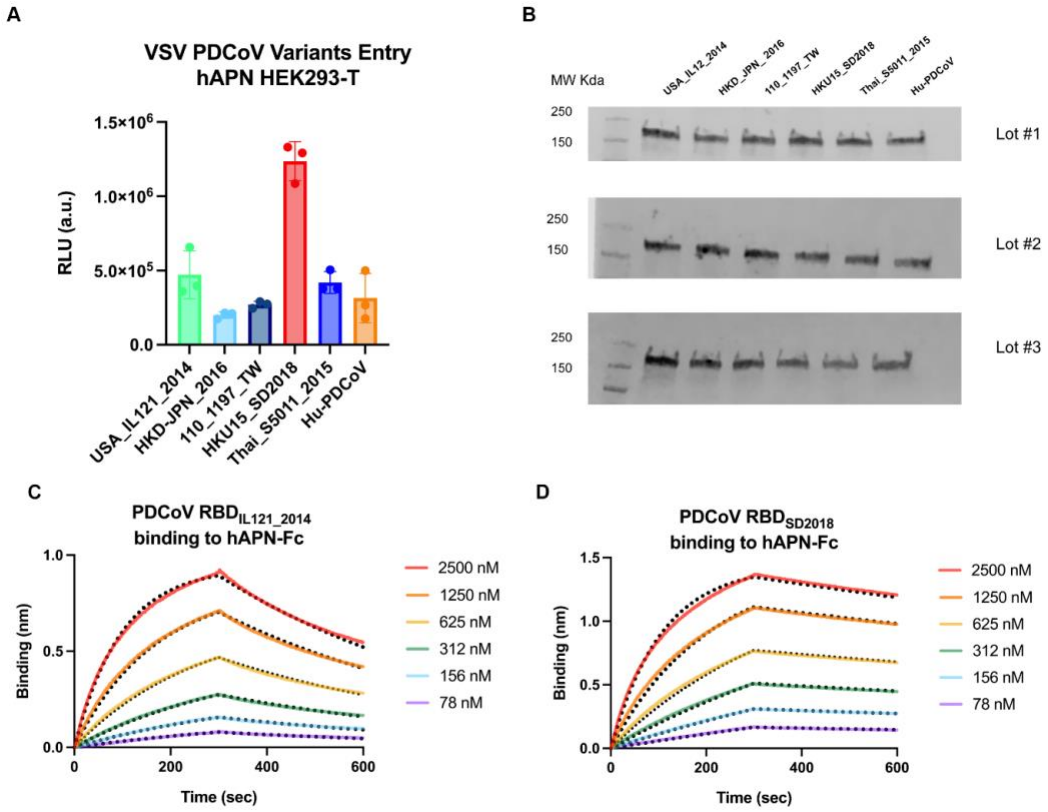

Figure 3.5.1. Functional characterization of PDCoV S variants. A, Entry of PDCoV S VSV variants into HEK293T target cells transiently transfected with human APN. **B,** Western blot quantification of PDCoV S incorporation in VSV pseudotypes for each of the three biological replicates used in panel A. **C-D,** BLI analysis of hAPN-Fc binding to the $PDCoV_{IL121\_2014}$ RBD (left) or to the $PDCoV_{SD\_2018}$ (right) immobilized onto Ni-NTA tips. Fits to the data are shown as black dotted lines and were used to determine the apparent binding affinity ($K_{D,app}$) of hAPN-Fc fragments to the two PDCoV RBDs.

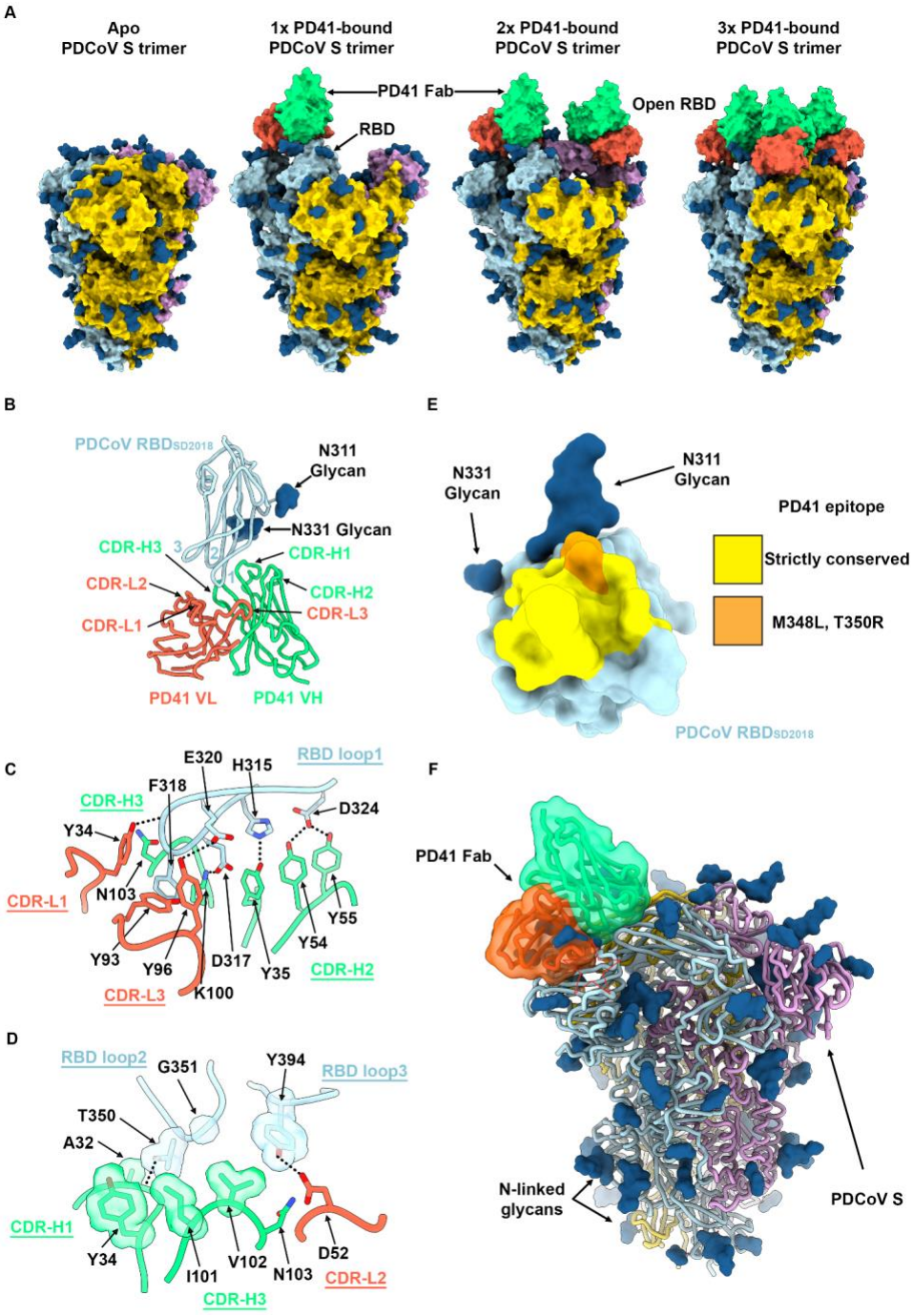

Figure 3.5.2. Molecular basis of broad PD41 mAb-mediated neutralization of PDCoV S variants. A, Surface renderings of the PDCoV S_{SD2018} trimer (gold, cyan and pink) without andwith one, two and three bound PD41 Fabs (green and orange for heavy and light chains, respectively) observed by cryoEM. N-linked glycans are rendered as blue spheres. **B,** Ribbon diagram of the PD41 Fab-bound PDCoV RBD_{SD2018} cryoEM structure at 3.0Å resolution obtained through local refinement of the one PD41-Fab bound S structure. PD41 V_H and V_L are respectively rendered in green and orange whereas the PDCoV RBD is colored cyan. The PDCoV receptor-binding loops are annotated 1-3 and the PD41 complementary determining regions (CDR) for light

and heavy chains are annotated CDR-L1, 2, 3 and CHR-H1, 2, 3. **C-D,** Zoomed-in views of the interface between PDCoV RBD_{SD2018} loop 1 (C) or loops 2 and 3 (D) and the PD41 Fab. Selected hydrogen bonds and salt bridges are shown as black dashed lines. A few side chains are shown in surface representation to highlight shape complementarity. **E,** PD41 epitope conservation across the panel of PDCoV S variants analyzed. Yellow indicates strict residue conservation whereas orange shows the positions of the M348L and T350R substitutions present in $S_{Thailand/S5011/2015}$. **F,** Superimposition of the PD41-bound PDCoV RBD structure with the PDCoV S ectodomain trimer structure (PDB 6BFU)[35] showing that PD41 could not bind to a closed S trimer without structural changes due to masking of the receptor-binding loops and resulting steric clashes (red star).

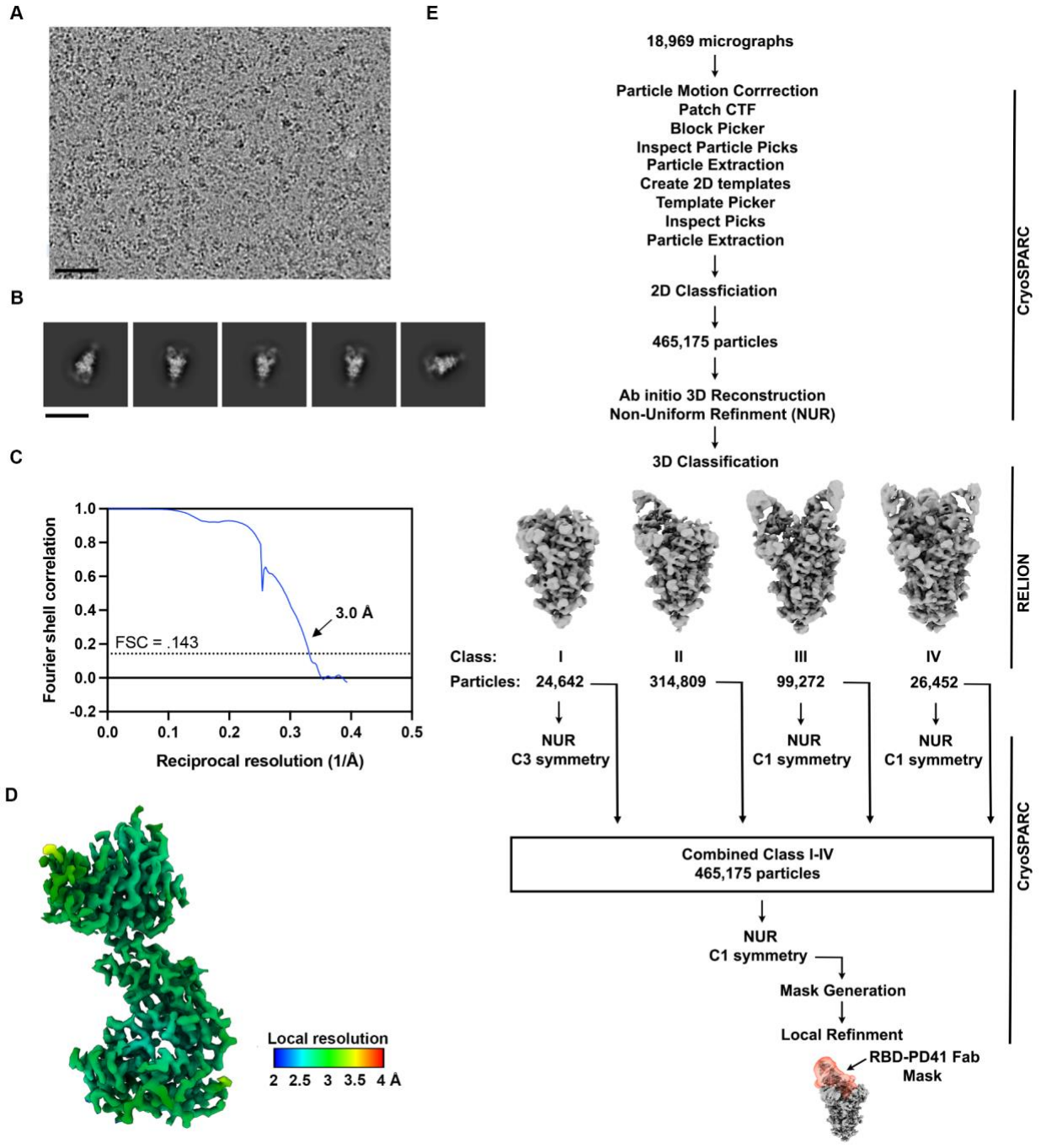

Figure 3.5.3: Cryo-EM data collection and refinement of PDCoV RBD$_{SD2018}$ bound to the PD41 Fab fragment. A, Representative electron micrograph (2.5 µm defocus, scale bar = 100 nm) **B,** 2D class averages (scale bar = 150 Å). **C,** Gold-standard Fourier shell correlation curve for the cryoEM reconstruction. The 0.143 cutoff is indicated with a black dashed line. **D,** 3D reconstruction of PDCoV RBD bound to PD41 colored by local resolution calculated using CryoSPARC. **E,** Flow chart of the pipeline for processing. CTF: contrast transfer function; NUR: non-uniform refinement.

3.6. The PD33 and PD41 mAbs competitively inhibit receptor binding

Given that PD33 and PD41 recognize epitopes mapping to the PDCoV S receptor binding loops, we hypothesized that the two mAbs inhibit APN engagement to the RBD competitively. Superimposition of the human APN-bound PDCoV RBD structure to our cryoEM structures further supported this hypothesis by revealing that APN binding would not be compatible with binding of either of these two mAbs due to major steric incompatibilities despite the different angles of approach of each Fab which recognize overlapping but distinct epitopes (**Figure 3.6.1A-B and Figure 3.6.2)**.

To evaluate the impact of each mAb on APN recognition, we performed a competition experiment to assess APN binding to the PDCoV RBD immobilized at the surface of biolayer interferometry biosensors with or without prior incubation with the PD33 Fab or the PD41 Fab. We found that PD33 or PD41 binding blocked subsequent APN binding to the RBD, thereby confirming the competitive mechanism of inhibition. The reverse experiment, however, revealed that pre-incubation of the immobilized PDCoV RBD with APN did not prevent subsequent Fab binding, suggesting that PD33 and PD41 can displace bound APN, likely due to their higher binding affinity.

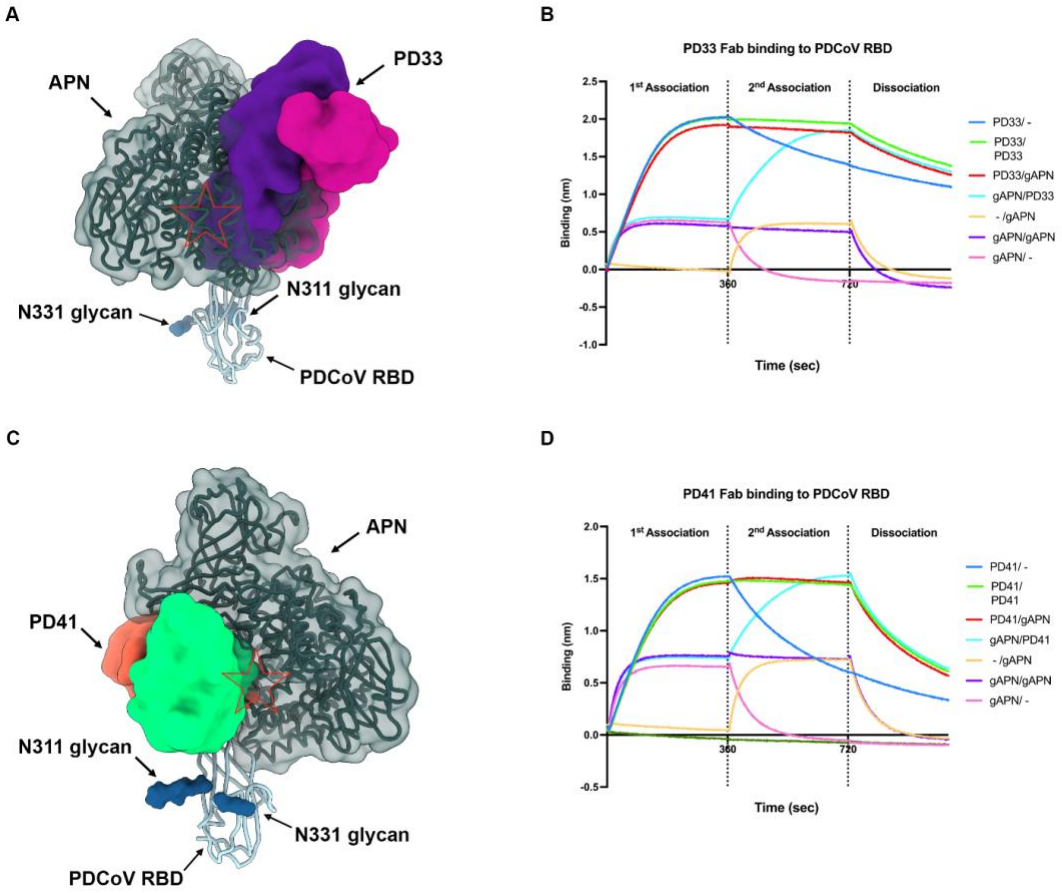

Figure 3.6.1: The PD33 and PD41 mAbs competitively inhibit receptor binding to the PDCoV RBD. A, PD33 (purple and magenta surfaces for the heavy and light chains, respectively) and human APN (hAPN, dark green) recognize overlapping sites on the PDCoV RBD (cyan ribbon). N-linked glycans are rendered as blue surfaces. The red star indicates steric clashes. **B,** BLI analysis of Fab PD33 binding to the PDCoV RBD immobilized on biosensors in the presence and absence of galline APN (gAPN). **C,** PD41 (purple and magenta surfaces for the heavy and light chains, respectively) and hAPN (dark green) recognize overlapping sites on the PDCoV RBD (cyan ribbon). N-linked glycans are rendered as blue surfaces. The red star indicates steric clashes. **D,** BLI analysis of Fab PD41 binding to PDCoV RBD immobilized on biosensors in the presence and absence of gAPN.

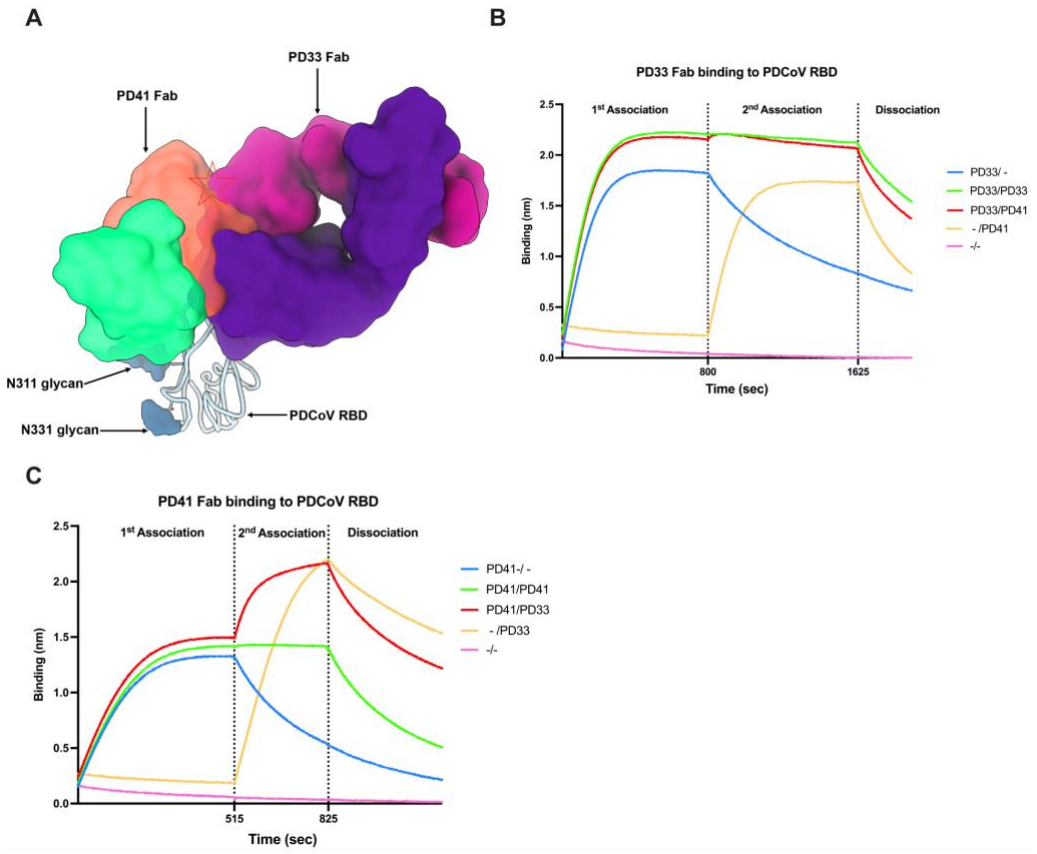

Figure 3.6.2: Superimposition of the PD33-bound PDCoV RBD and of the PD41-bound PDCoV RBD$_{SD2018}$ structures showing recognition of distinct but overlapping epitopes. A, PD33 (purple and magenta surfaces for the heavy and light chains, respectively) and PD41 (green and orange surfaces for the heavy and light chains, respectively) recognize overlapping epitopes on the PDCoV RBD (cyan ribbon). N-linked glycans are rendered as blue surfaces. The red star indicates steric clashes. **B,** BLI analysis of Fab PD33 binding to the PDCoV RBD immobilized on biosensors in the presence and absence of Fab PD41. **C,** BLI analysis of Fab PD41 binding to the PDCoV RBD immobilized on biosensors in the presence and absence of Fab PD33.

3.7. Deep mutational scanning of the PDCoV RBD identifies constrained paths of resistance

To identify paths of possible resistance, we performed deep mutational scanning (DMS) to comprehensively identify mutations that escape binding(Greaney et al. 2020; Starr et al. 2021) of PD33 and PD41, the two other neutralizing mAbs (PD17 and PD20) and two non-neutralizing mAbs (PD3 and PD8). We constructed a site saturation mutagenesis library of the PDCoV Illinois121_2014 RBD in a yeast-display platform for deep mutational scanning(Starr et al. 2020), and identified all mutations that escape binding by each mAb via fluorescence-activated cell sorting (FACS) and deep sequencing (**Figure 3.7.1** and **Figure 3.7.2**). To identify functional constraints, we colored mutations in our escape maps according to orthogonally measured DMS impacts on galline APN (gAPN) receptor-binding avidity.

Our DMS escape profiles for PD33 and PD41 concur with the epitopes defined structurally (**Figures 3.4.1** and **3.5.2**), but highlight the hotspot nature of certain residue interactions within the interface (**Figure 3.7.1A-B**) (Cunningham and Wells 1989; Dingens et al. 2019). Escape from each mAb is focused on sites at the receptor-contact surface: PD33 escape is focused on residues G319 and E320 on RBD loop 1, and Y394, V395, W396, and Y398 on RBD loop 3 whereas PD41 escape is focused on RBD loop 1 residues H315, D317, F318, G319, R322, and D324. For each mAb, most escape mutations led to severe dampening of gAPN-binding affinity, suggesting that they would not be tolerated due to reduced viral fitness. Our DMS escape profiles further support the broad cross-reactivity of PD33 and PD41 as most PDCoV sequence variants are not among the set of amino acid changes that facilitate mAb escape (**Figure 3.7.1C**). The only exception is the PDCoV isolate JS2019_A1414, which may have reduced sensitivity to the PD41 mAb due to the D317A mutation.

Despite targeting overlapping structural epitopes at the receptor-binding interface (**Figure 3.6.1**), PD33 and PD41 DMS escape profiles do not overlap with the exception of substitutions to site G319, which are universally deleterious for receptor-binding affinity (mean 186-fold loss of binding avidity to gAPN dimer, range 51- to 421-fold). The intolerance to mutation at position 319 likely results from steric incompatibility of replacing a glycine by any other residues at the binding interface. Accordingly, G319 is largely conserved across the delta-CoV phylogeny (**Figures 3.7.2c**) including the distant avian viruses MoorhenCoV_HKU21 and SparrowCoV_HKU17. Due to orthogonality of escape profiles despite overlapping structural epitopes, PD33 and PD41 could form a suitable antibody cocktail with enhanced resistance to escape (Greaney et al. 2020).

Comparison of the DMS epitope profiles for PD33 and PD41 to those for PD17, PD20, PD3, and PD8 illustrate a clear relationship between neutralizing potency and the antigenic sites recognized (**Figure 3.7.1A-B**). The potently neutralizing mAbs PD33 and PD41 epitopes map to the receptor-binding loops, that are functionally equivalent to the receptor-binding motif (RBM) of sarbecoviruses and merbecoviruses, directly competing with APN binding to the RBD (**Figure**

3.6.1). Our DMS escape maps show that PD17 and PD20, which also neutralize PDCoV, albeit less potently than PD33 and PD41, recognize epitopes also in the RBM but closer to the RBD equator. The non-neutralizing mAbs PD3 and PD8 bind to the core RBD and their epitopes do not overlap with the APN-binding surface, likely explaining their inability to inhibit PDCoV S pseudoviruses. These data clearly illustrate that receptor interference is a primary mechanism of PDCoV neutralization.

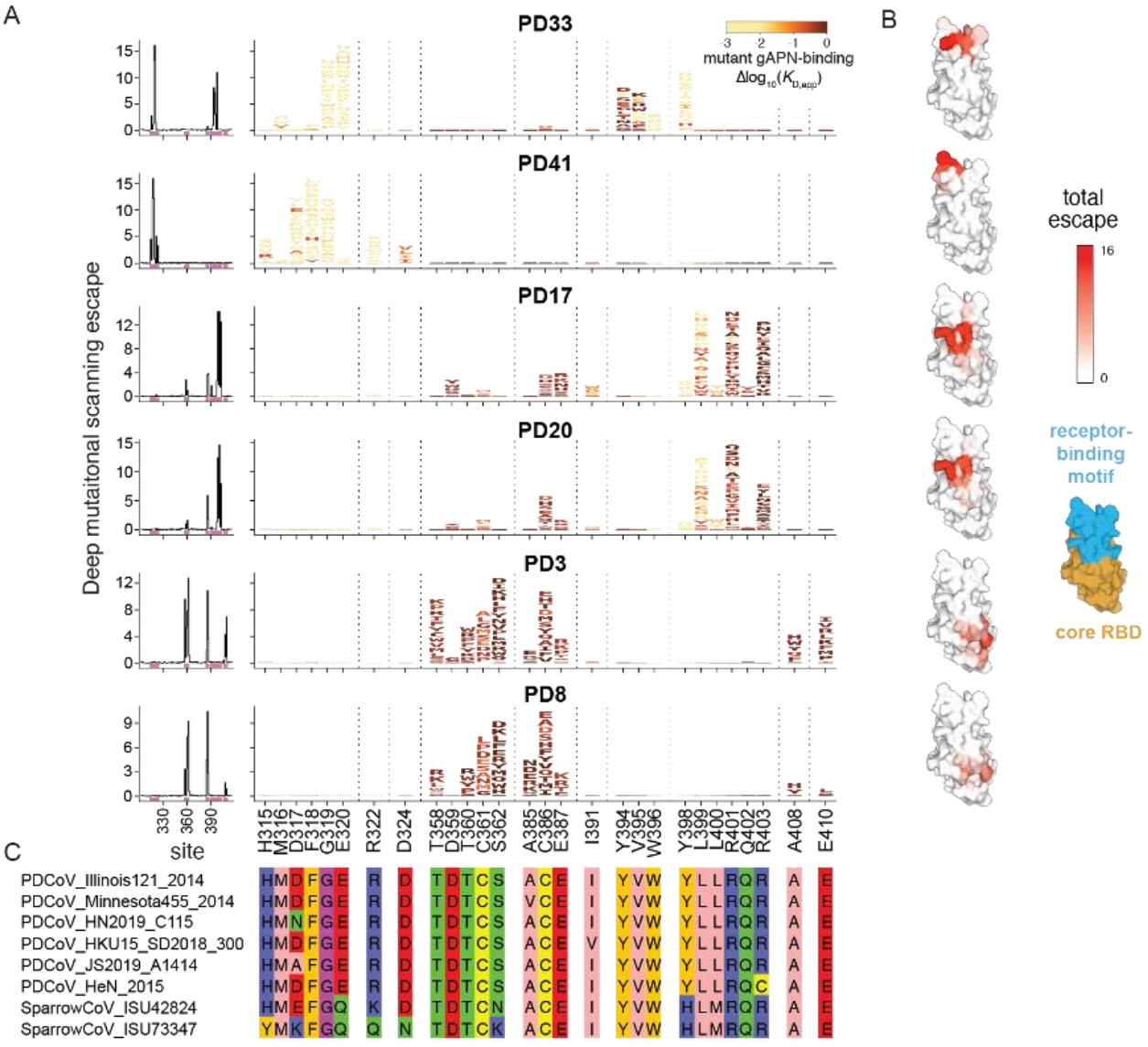

Figure 3.7.1: Prospective mapping of PDCoV escape mutants by deep mutational scanning. A, Comprehensive maps of escape from PDCoV RBD mAbs. For each mAb, lineplots (left) show the total extent of mutational escape from mAb binding for mutations at each site in the RBD. For sites of strong escape (pink bars in lineplot), logoplots at right illustrate the capacity of individual mutations to escape mAb binding, where full-height letters correspond to 10-fold or greater loss

of mAb binding in the DMS assay. Mutations are colored according to their orthogonally measured impacts on gAPN-binding avidity, with increasingly light yellow reflecting increasingly deleterious impacts on receptor binding. See **Figure 3.7.2AB** for further experimental details. **B**, Sitewise escape (y-axis in lineplots in panel A) mapped to the PDCoV RBD structure (PDB 6BFU). Key at right illustrates the receptor-binding motif (blue) versus core RBD in the matched RBD orientation. **C**, Alignment of unique PDCoV sequence isolates at sites illustrated in logoplot. See **Figure 3.7.2C** for full delta-coronavirus alignment at logoplot sites.

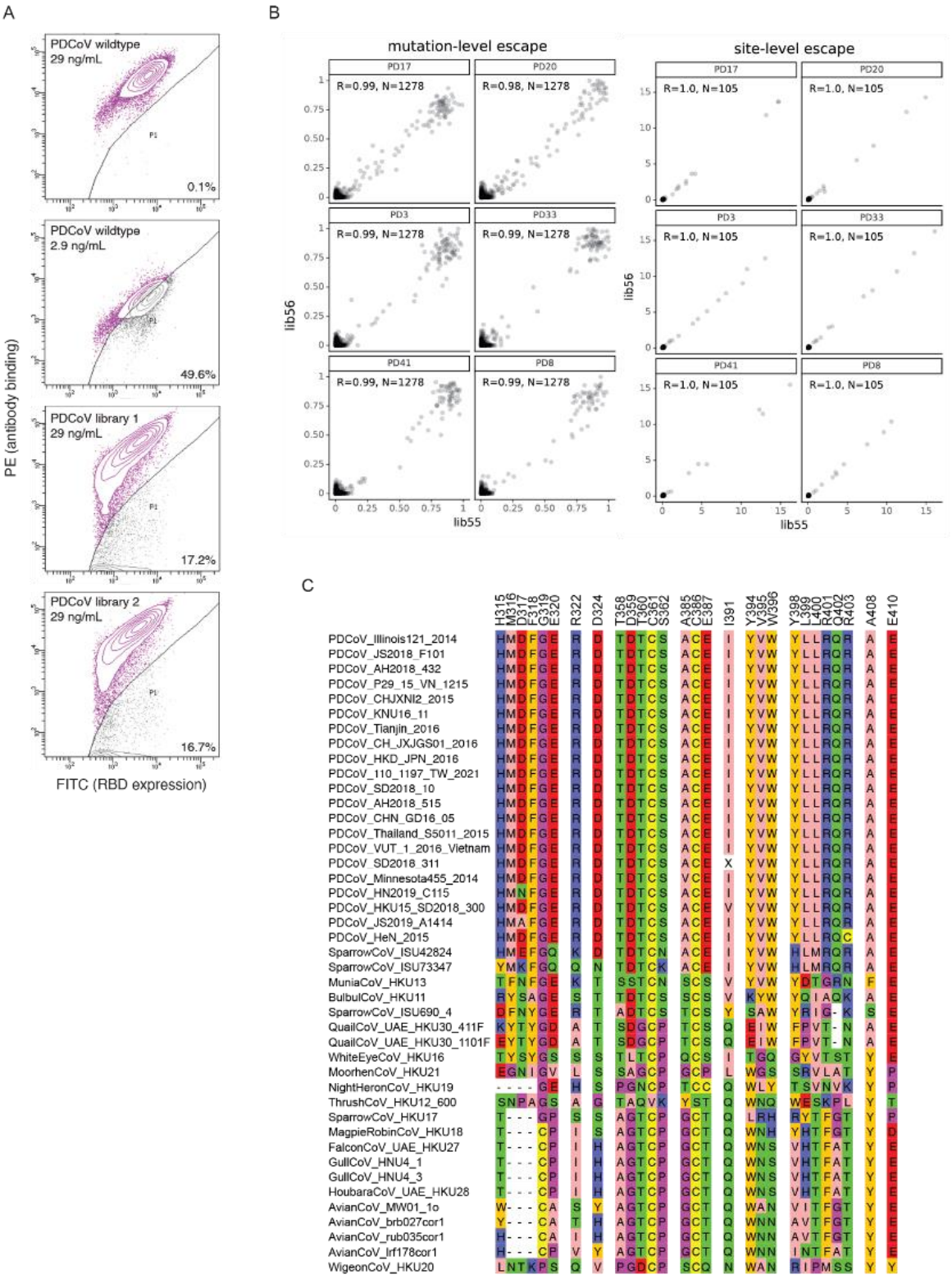

Figure 3.7.2: Experimental details of deep mutational scanning selection of mAb escape mutations. A, Representative FACS gates used to identify mutations that escape mAb binding. For each experiment, an antibody-escape gate was drawn that captures approximately 50% of cells of the wildtype control labeled at 10% of the library selection antibody concentration. The "escape

fraction" generated via sequencing-based counts estimates the fraction of cells of each mutant genotype that fall into this antibody-escape sort bin. **B**, For each mAb, the correlation in the per-mutation escape fraction (left) or the sum of escape fractions of all mutations at a site (right; total escape, the value shown in line plots in Figure 5A). **C**, Full alignment of deltacoronavirus sequences at the sites of strong escape visualized in Figure 5.

3.8. RBD-APN interface enhancing mutations identified by deep mutational screening are neutralized by PD33 and PD41

Deep mutational scanning of the 100 residues spanning the PDCoV RBD interface involved in binding to host receptor APN orthologs (galline, human and porcine) led to the identification of three sites that tolerated substitutions and surprisingly led to enhanced binding and entry to APN orthologs; PDCoV $RBD_{R357W/Y,\ L399Q,\ R401N}$. Mutations arising at the RBD-receptor interface exhibiting enhanced host receptor binding and viral entry can be associated with enhanced viral fitness and immune evasion, as seen with SARS-CoV2 omicron. These variants pose a danger to human and animal health as previous antibodies and vaccines have decreased neutralization potency and impaired ability to provide protection (Kim et al. 2022, Shi et al. 2024, Willet et al. 2022). We sought to determine if PD33 and PD41 mAbs would retain the ability to neutralize PDCoV $RBD_{R357W/Y,\ L399Q,\ R401N}$ mutants. We evaluated their ability to neutralize VSV pseudotyped with PDCoV S-harboring single mutations PDCoV $RBD_{R357W/Y,\ L399Q,\ R401N}$, double mutations PDCoV $RBD_{L399Q\text{-}R401N}$ and triple mutations PDCoV $RBD_{R357W/Y\text{-}L399Q\text{-}R401N}$ in presence of the PD33 and the PD41 mAbs using HEK293T target cells transiently transfected with human APN (hAPN). PD33 and PD41 neutralized all single, double and triple mutants with half-maximal inhibitory concentrations (IC_{50}) below 1 μg/ml, matching the potency of wild type variant PDCoV RBD_{IL121_2014} (**Figure 3.8.1AC**). Structural analysis of the PD33 Fab-bound PDCoV RBD_{IL121_2014} cryoEM structure demonstrates that while PDCoV $RBD_{R357,\ L399,\ R401}$ residues are part of the PD33 epitope only PDCoV RBD_{R401} forms a strong hydrogen bond contact with PD33 CDR-$H2_{N56}$. This hydrogen bond interaction is most likely to be retained in the mutant PDCoV RBD_{R401N} (**Figure 3.8.1B**). Similarly, structural analysis of the PD41 Fab-bound PDCoV RBD_{SD2018} cryoEM structure clearly illuminates the ability of PD41 to neutralize the mutants as PDCoV $RBD_{R357,\ L399,\ R401}$ are not part of the PD41 epitope and do not engage with binding to PD41 Fab (**Figure 3.8.1D**). The synergism of the structural and cell-based data supports that PD33 and PD41 can neutralize and provide protection against PDCoV $RBD_{R357W/Y,\ L399Q,\ R401N}$ mutants if they were to arise in nature. In light of the antibody escape profile of PDCoV **(Figure 3.7.1)**, it appears that PDCoV does not tolerate mutations at the RBD-APN receptor interface, thereby constraining the virus to immune evasion of antibodies such as PD33 and PD41 that target this interface.

A

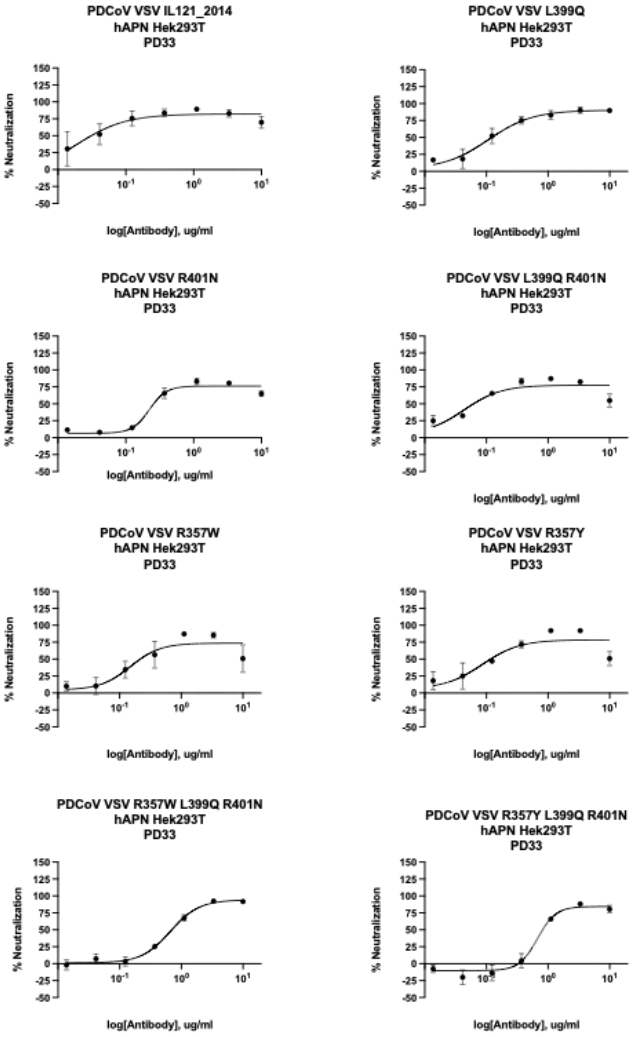
PDCoV VSV IL121_2014
hAPN Hek293T
PD33
PDCoV VSV L399Q
hAPN Hek293T
PD33
PDCoV VSV R401N
hAPN Hek293T
PD33
PDCoV VSV L399Q R401N
hAPN Hek293T
PD33
PDCoV VSV R357W
hAPN Hek293T
PD33
PDCoV VSV R357Y
hAPN Hek293T
PD33
PDCoV VSV R357W L399Q R401N
hAPN Hek293T
PD33
PDCoV VSV R357Y L399Q R401N
hAPN Hek293T
PD33
% Neutralization
log[Antibody], ug/ml

B

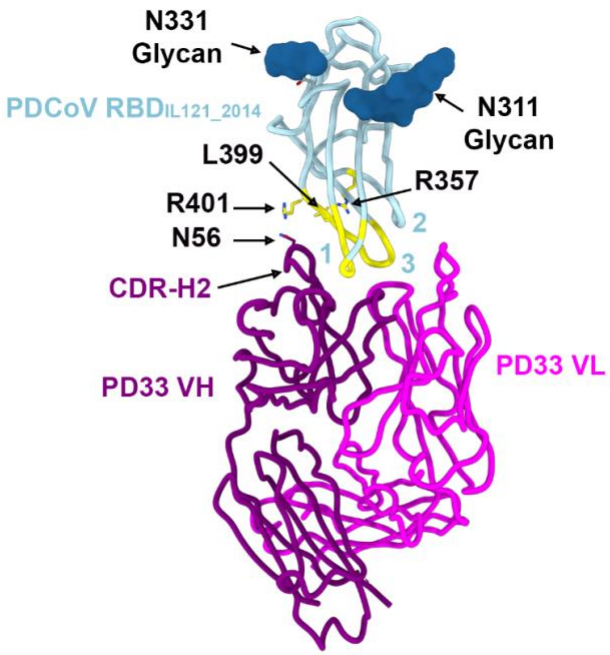
N331
Glycan
PDCoV RBDIL121_2014
N311
Glycan
L399
R357
R401
N56
1
2
3
CDR-H2
PD33 VH
PD33 VL

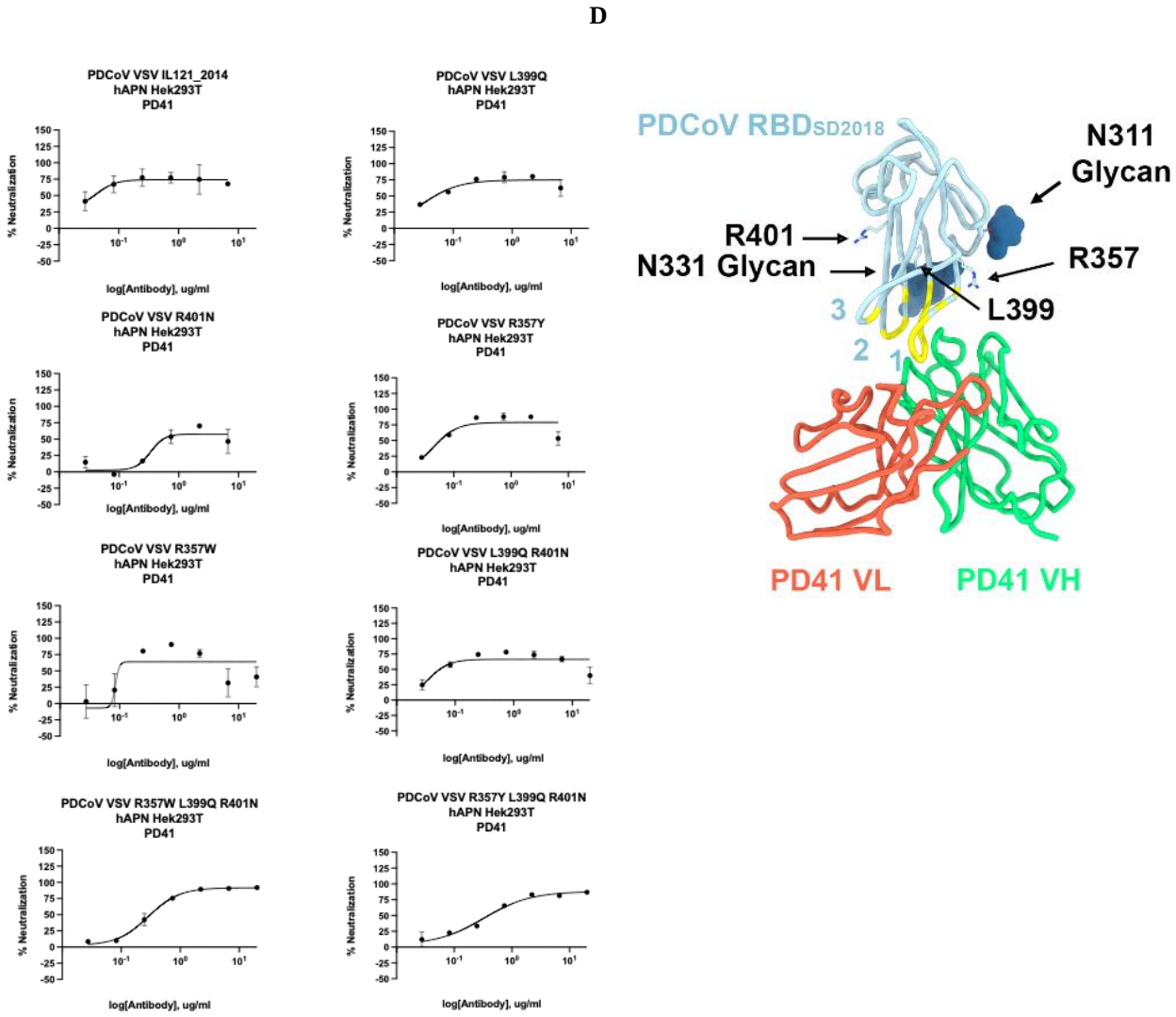

Figure 3.8.1: PD33 and PD41 mAbs neutralize RBD-APN interface enhancing mutations discovered from deep mutational scanning. A, Dose-dependent PD33 mAb-mediated neutralization of PDCoV S VSV mutants using HEK293T target cells transiently transfected with human APN. **B,** Ribbon diagram of the PD33 Fab-bound PDCoV RBD_{IL121_2014} cryoEM structure. PD33 V_H and V_L are respectively rendered in purple and pink whereas the PDCoV RBD is colored cyan. The PDCoV receptor-binding loops are annotated 1-3 and the PD33 complementary determining regions (CDR) for heavy chain annotated as CDR-H2. N-linked glycans are rendered as blue spheres. The PD33 epitope residues on the RBD loops 1 and 3 are highlighted in yellow with the mutants R357, L399, R401 shown as sticks and the corresponding N56 interacting residue on PD33 CDR-H2 shown as stick. **C**, Dose-dependent PD41 mAb-mediated neutralization of PDCoV S VSV mutants using HEK293T target cells transiently transfected with human APN. **D,** Ribbon diagram of the PD41 Fab-bound PDCoV RBD_{SD2018} cryoEM structure PD41 V_H and V_L are respectively rendered in green and orange whereas the PDCoV RBD is colored cyan. The PDCoV receptor-binding loops are annotated 1-3. N-linked glycans are rendered as blue spheres. The PD41

epitope residues on the RBD loops 1, 2 and 3 are highlighted in yellow with the residues R357, L399, R401 shown as sticks. There are no PD41 residues shown as sticks as none interact with R357, L399, R401.

3.9. Discussion

The recently described zoonotic introductions and detection of PDCoV in Haitian children[16] underscores more coronaviruses spillover to humans than previously appreciated. PDCoV belongs to the most recently described delta-coronavirus genus, which was not previously known to comprise human pathogens, for which correlates of protection are poorly understood. Strikingly, only 4 out of 9 RBD-directed mAbs screened in this study had detectable neutralizing activity against the vaccine-matched pseudovirus and the two most potent mAb inhibited receptor-binding competitively. The PDCoV RBD is thus a prime target of humoral immunity which is reminiscent of SARS-CoV-2 RBD-directed antibodies that account for most of the neutralizing activity against vaccine-matched and mismatched viruses upon infection or vaccination[26,40–42]. Future studies will elucidate the role of NTD-directed and fusion machinery-directed antibodies against PDCoV. The broad neutralizing activity of PD33 and PD41 against a panel of PDCoV isolates and mutants identified from deep mutational scanning of the PDCoV RBD suggest that these antibodies would provide some resilience to viral evolution and could be stockpiled for pandemic preparedness. These could be deployed as individual mAb therapies or mAb cocktail given that the epitopes for PD33 and PD41 are not entirely overlapping and together would encompass all key residues involved in host APN binding from RBD loops 1-3.

Although cryoEM structures of the SARS-CoV-1, SARS-CoV-2 and MERS-CoV S trimers revealed the conformational landscape of the RBDs[20,30,43–46], which can adopt open and closed conformations, other S trimers have largely been found in the closed state[13,18,35,47–52]. Recent work, however, showed that α2,8-linked 9-O-acetylated disialosides binding to the HKU1 S NTD induces RBD opening and subsequent binding to the TMPRSS2 receptor[53,54]. These data suggest that other coronavirus S trimers, such as PDCoV S, could possibly open in response to engagement of an attachment factor, thereby allowing binding to an entry receptor and viral entry. This strategy would promote masking of key sites of vulnerabilities (e.g. the receptor-binding motif) from the immune system while ensuring proper spatial and temporal coordination of the conformational changes required to engage the entry receptor and initiate infection[52]. Future identification of the molecular determinants of PDCoV S opening will reveal the cascade of events leading to productive infection, inform tissue and species tropism and guide vaccine design against this emerging pathogen.

3.10. Methods

PDCoV immunization and antibody discovery from Alloy mice

Pre-immune serum was obtained from each mouse a week before immunization. ATX mice were successively immunized with recombinant PDCoV$_{IL121_2014}$ RBD and S diluted (1:1) in Magic Mouse adjuvant (Cat#: CDN-A001E; CD Creative Diagnostics) and injected subcutaneously. On day 0, mice received prime immunization with 5 µg of PDCoV RBD$_{IL121_2014}$ and were boosted on day 14 with 5 µg of PDCoV S$_{IL121_2014}$ ectodomain. On day 29, the mice received 5 µg of PDCoV RBD$_{IL121_2014}$ and on day 56 they received a last boost with 2 µg of PDCoV S$_{IL121_2014}$. On day 64, the mice were sacrificed and peripheral blood, spleen and lymph nodes (LN) were collected and cells freshly isolated. B cells were enriched by positive selection using mouse CD19 microbeads and LS columns (Miltenyi). Enriched B cells were then stained with mouse anti-IgM, anti-IgD, and biotinylated PDCoV S$_{IL121_2014}$ ectodomain labeled with both PE and Alexa-Fluor 647 streptavidin (Life Technologies). Sorted IgG+ memory B cells were seeded at clonal dilution in 384-well plates an a monolayer of feeder mesenchymal cells in the presence of B cell survival factors. Clones positive for antigen binding were then isolated, sequenced and produced recombinantly in transiently transfected CHO cells.

Fab Fragment of monoclonal antibodies for binding and cryo-EM studies

Fab Fragments were generated by taking .5 mg of IgG and digesting with 2 µL of Lys C (NEB#P8109S) at 37℃. Digested product was bound to 500 µL of protein A resin beads (GenScript #L00210) overnight at 4℃ on a rotating shaker. Flow through post binding was collected, purified using size exclusion chromatography Superdex 200 10/300 and concentrated using Amicon Ultra-15 Centrifugal Filter Unit (10kDa). Purified Fab fragments were snap frozen and stored at -80℃.

Production of anti-human kappa light chain nanobody

The pET23b with Anti-human kappa light chain nanobody with a C-terminal 8x His tag (PDB: 7WPD_Z) construct was transformed into *E. coli* BL21(DE3) cells. Overnight culture in Luria-Bertani (LB) media was initiated and incubated at 37 ℃ with shaking. 2L of LB media were inoculated with overnight culture and were induced in the exponential phase (OD600 = 0.6) by adding 1 mM IPTG. The cells were switched to 16 ℃ and grown overnight. Cells were collected by centrifugation for 15 minutes at 3000xg 4℃. Cell pellet was resuspended in 30 mL of cold 50mM Tris, 150mM NaCl, pH 8.0. Mixture was dounce homogenized 10x and sonicated using an Emulsiflex for 4x rounds. Cells were spun at 15,000 x g 4℃ for 30 minutes. Lysate was filtered using a 0.25 µm syringe filter and applied to Talon metal affinity resin (Takara) in 50mM Tris-HCl, 150mM NaCl, 10mM Imidazole at pH 8.0. Unbound proteins were washed in 10 column volumes of 50mM Tris-HCl, 150mM NaCl, 10mM Imidazole at pH 8.0. Eluted with 50mM Tris, 150mM NaCl, 250 mM Imidazole at pH 8.0. The eluted protein was concentrated using Amicon Ultra-15 Centrifugal Filter Unit (10kDa) and buffer exchanged into 50mM Tris, 150mM NaCl pH

8.0 and further purified using size exclusion chromatography Superdex 200 10/300. Nanobody proteins were snap frozen in liquid nitrogen and stored at -80°C.

Production of recombinant PDCoV S glycoprotein

The $PDCoV_{IL121\_2014}$ S glycoprotein ectodomain (Genbank KJ481931.1) and SD2018/300 (Genbank KJ481931.1) were cloned into pcDNA3.1+ plasmid by GenScript with the host N-terminal signal peptide sequence, C-terminal foldon domain, thrombin cleavage sequence, short linker of GSG, AVI tag and 8 x His tag. The DNA constructs were expanded using DH5α cells and purified using Qiagen MegaPrep Kit. Protein was expressed using ExpiFectamine 293 Transfection Kit (Thermo Fisher Scientific). Expi293F cells were grown at 37°C with 8% CO_2 to 3E6 cells and transfected with 100µg of DNA. Cell culture supernatants were harvested four days post-transfection. Protein was purified using HisTrap^{Tm} High Performance column (Cytiva). Protein was bound to HisTrap resin in 50mM Tris-HCl, 150mM NaCl, 10mM Imidazole at pH 8.0. Unbound proteins were washed in 10 column volumes of 50mM Tris-HCl, 150mM NaCl, 10mM Imidazole at pH 8.0. Eluted with 50mM Tris, 150mM NaCl, 250 mM Imidazole at pH 8.0. The eluted S protein was concentrated using Amicon Ultra-15 Centrifugal Filter Unit (100kDa) and buffer exchanged into 50mM Tris, 150mM NaCl pH 8.0. Endotoxin levels were assessed using Charles River Limulus Amebocyte Lysate (LAL) cartridges. Proteins were snap frozen in liquid nitrogen and stored at -80°C.

Production of recombinant PDCoV RBD

The $PDCoV_{IL121\_2014}$ RBD (Genbank KJ481931.1) and SD2018/300 (Genbank KJ481931.1) spanning residues 303-415 were cloned into pcDNA3.1+ plasmid by GenScript with an N-terminal mu-phosphatase signal peptide sequence and C-terminal short linker GSG, AVI tag and 8 x His tag. The DNA constructs were expanded using DH5α cells and purified using Qiagen MegaPrep Kit. Protein was expressed using ExpiFectamine 293 Transfection Kit (Thermo Fisher Scientific). Expi293F cells were grown at 37°C with 8% CO_2 to 3E6 cells and transfected with 100 µg of DNA. Cell culture supernatants were harvested four days post-transfection. Protein was purified using HisTrap^{Tm} High Performance column (Cytiva). Protein was bound to HisTrap resin in 50mM Tris-HCl, 150mM NaCl, 10mM Imidazole at pH 8.0. Unbound proteins were washed in 10 column volumes of 50mM Tris-HCl, 150mM NaCl, 10mM Imidazole at pH 8.0. Eluted with 50mM Tris-HCl, 150mM NaCl, 250 mM Imidazole at pH 8.0. The eluted RBD was concentrated using Amicon Ultra-15 Centrifugal Filter Unit (10 kDa) and buffer exchanged into 50mM Tris, 150mM NaCl pH 8.0 and further purified using size exclusion chromatography Superdex 200 10/300. Endotoxin levels were assessed using Charles River Limulus Amebocyte Lysate (LAL) cartridges. Proteins were snap frozen in liquid nitrogen and stored at -80°C.

Production of recombinant APN ectodomain

The APN ectodomain from galline (Genbank ACZ95799.1) and human residues 66-967 was cloned into pcDNA3.1+ plasmid by GenScript with an N-terminal mu-phosphatase signal peptide sequence and C-terminal short linker GGS, thrombin cleavage site, human Fc fragment. The DNA constructs were expanded using DH5α cells and purified using Qiagen MegaPrep Kit. Protein was expressed using ExpiFectamine 293 Transfection Kit (Thermo Fisher Scientific). Expi293F cells were grown at 37℃ with 8% CO_2 to 3E6 cells and transfected with 100 µg of DNA. Cell culture supernatants were harvested four days post-transfection. Protein was purified using HighTrap Protein A column (Cytiva). Protein was bound to resin in 50mM Tris-HCl, 150mM NaCl pH 8.0. Unbound proteins were washed in 10 column volumes of 50mM Tris-HCl, 150mM NaCl at pH 8.0. Eluted with 0.1 M Citric Acid (pH 3.0) and neutralized with 1 M Tris-HCl (pH 9.0). The eluted APN was buffer exchanged into 50mM Tris, 150mM NaCl pH 8.0 and further purified using size exclusion chromatography Superdex 200 Increase 10/300 GL. Protein was concentrated using the Amicon Ultra-15 Centrifugal Filter Unit (100 kDa). Proteins were snap frozen in liquid nitrogen and stored at -80℃.

Production of VSV pseudoviruses

PDCoV S glycoprotein constructs containing a C-terminal deletion of 21 residues to improve exportation to the membrane followed by a Flag tag were cloned into pcDNA3.1+ by GenScript. HEK293T cells were seeded at 16E6 cells in 100 mm dishes (Corning) poly-D-Lysine coated. Cells were transfected with 24 µg of DNA and 60 µL of Lipofectamine 2000 (Thermo Fisher Scientific) in Opti-MEM transfection medium. Post 5 hour incubation DMEM containing 20% FBS and 2% PenStrep was added to the cells. After 21 hours at 37 °C with 5% CO_2 the cells are washed 1x with DMEM and infected with VSV (G∗ΔG-luciferase) in DMEM for 2 hours. The cells are washed 2x with DMEM and anti-VSV G antibody (I1-mouse hybridoma supernatant diluted 1:40 in DMEM, ATCC CRL-2700) is added and incubated for 24 hours at 37 °C with 5% CO_2. Pseudovirus is harvested and collected by centrifugation at 3,000xg for 10 min. Supernatant containing the pseudovirus is filtered using a 0.45 µm syringe filter and concentrated 5x prior to storage at -80°C. Mock VSV pseudoviruses were prepared as above but without S glycoprotein transfection.

Western Blot Analysis of VSV pseudoviruses

Western blot analysis was performed to determine the levels of S glycoprotein for each of the VSV pseudoviruses. 30 µL of virus is obtained and mixed with 10 µL of 4x LDS sample reducing buffer. Samples were boiled at 95 °C for 5 minutes and spun down. 35 µL of final mixture was run on 4-20% Mini-Protean TGX precast protein gel at 150 Volts for 45 minutes. Proteins were transferred using Trans-Blot Turbo Mini 0.2 µm PVDF Transfer Packs and membranes were incubated with

Intercept (TBS) Blocking Buffer (Licor) for 1 hour at room temperature. Anti-Fusion peptide antibody at 1 μg/ml was diluted in Intercept (TBS) Antibody Diluent Buffer (Licor) and incubated at 4°C overnight. The following day membranes were washed with TBST 3x with 5-minute incubations at room temperature. Anti-human Fc (Jackson ImmunoResearch) was diluted 1:50,000 in Intercept (TBS) Antibody Diluent Buffer (Licor) and membranes were incubated at room temperature for 1 hour. Membranes were washed with 3x TBST with 5 minute incubations at room temperature. Images were taken using the Licor Odyssey CLx.

Cell entry assays

HEK293T cells were transiently transfected with human APN (hAPN). hAPN with a C-terminal Flag tag was cloned into pcDNA3.1+ by GenScript. HEK293T cells seeded at 16E6 cells in 100 mm dishes coated with poly-D-Lysine and incubated overnight at 37 °C with 5% CO_2. The following day cells were transfected with 8 μg of DNA using 30 μL of Lipofectamine 2000 transfection kit in Opti-MEM. Post 5 hours of incubation with transfection reagent, cells were trypsinized with 0.05% Trypsin EDTA for 3 minutes and neutralized with DMEM with 10% FBS 1% penicillin–streptomycin. 40,000 cells were seeded in 96-well plates (Corning 3610) coated with poly-lysine (Sigma P4707) and allowed to incubate at 37 °C with 5% CO_2. Following day, media was removed and 20 μL of DMEM was added followed by 20 μL of VSV pseudotyped with PDCoV S variants for 2 hours at 37 °C with 5% CO_2. Cells were supplemented with 40 μL of DMEM containing 20% FBS and 2% PenStrep and incubated for 22 hours at 37 °C with 5% CO_2. 40 μL of One-Glo-EX substrate (Promega) was added and cells were incubated at 37 °C for 10 minutes with shaking. Luminescence was read using BioTek Neo2 plate reader. Technical replicates of three were run for three different lots of pseudovirus for each variant. Luciferase units were plotted using Graphpad Prism.

Neutralization assays

For mAb neutralization assays against PDCoV S VSV, HEK293T cells were transfected with hAPN as described in the cell entry assay. 40,000 cells/well were seeded into 96-well plates coated with poly-lysine and incubated overnight at 37°C. Antibody titration series was performed in a half-area 96-well plate (Greiner) starting at a 2x concentration of 20 μg/ml and diluting 1:3 with DMEM. Equal volume of pseudovirus was added and incubated at room temperature for 30 minutes and 40 μL was transferred to cells and incubated for 2 hours at 37 °C with 5% CO_2. Cells were supplemented with 40 μL of DMEM with 20% FBS and 2% PenStrep and incubated for 22 hours at 37 °C with 5% CO_2. After 22 hrs, 40 μL of One-Glo-EX substrate (Promega) was added to each well and incubated on a plate shaker in the dark for 5 min before reading the relative luciferase units using a BioTek Neo2 plate reader. Relative luciferase units were used to determine (%) neutralization in Prism (GraphPad). Nonlinear regression curve fit and sigmoidal 4PL where

x is the concentration was run to determine IC50 values for 3 biological replicates of pseudovirus and three technical replicates for each titration series.

Biolayer interferometry analysis (BLI)

BLI binding assays were performed on an Octet Red (Sartorius) instrument operated at 30°C with shaking (1000 rpm). Nickel-NTA biosensor tips were hydrated in 10 x Kinetics Buffer for 10 minutes at room temperature. PDCoV RBD-His was loaded at 10 μg/ml in 10 x Kinetics Buffer to 1 nm. Loaded tips were dipped into a 10x Kinetics buffer to stabilize and remove any unbound protein for 60 seconds. Loaded RBD tips were dipped into 1 μg/ml of Fab fragment for 360 seconds. Associated Fab fragment to the RBD was preceded by a dissociation phase of tips being moved into a 10x kinetics buffer for 360 seconds. K_D determination of PD33 and PD41 Fab to RBD was obtained through a concentration series starting at 25 nM and titrated down by two fold down to 0.39 nM. $KD_{apparent}$ determination of RBD to hAPN-Fc was obtained through a concentration series starting at 5 μM and titrated down by two fold down to 39 nM. K_D values were calculated using ForteBio data analysis software where fitting of curves using a 1:1 binding model was used. For the competition experiment of Fab and gAPN-Fc post loading with RBD, 25nM of Fab was tested against 250nM of gAPN-Fc. For the competition experiment of Fab PD33 and Fab PD41, PDCoV RBD-AVI-Biotinylated was loaded at 2.5 μg/ml in 10 x Kinetics Buffer to 1 nm, 1 μg/ml of associated and bound Fab PD33 was tested against 1.0 μg/ml of Fab PD41 and the opposite was performed where 1 μg/ml of Fab PD41 was tested against 1.0 μg/ml of Fab PD33.

Cryo-EM sample preparation and data collection

For PD33 Fab bound PDCoV RBD structure, 2 μM PDCoV RBD complex with 1 μM PD33 Fab and 1.5 μM anti-human kappa light chain nanobody were prepared by incubation for 1 hour at 4°C. Nanobody was used to stabilize the constant region of the PD33 Fab structure. 3ul of PDCoV RBD/PD33Fab/nanobody complex were directly applied to freshly glow-discharged grids. The Cryo-EM grids were prepared using a Vitrobot Mark IV (Thermo Fisher Scientific) with R 2/2 UltrAuFoil grids and a Chameleon[55] (SPT Labtech) with self-wicking nanowire Cu R1.2/0.8 holey carbon grids. Data were acquired using an FEI Titan Krios transmission electron microscope operated at 300 kV and equipped with a Gatan K3 direct detector and Gatan Quantum GIF energy filter operated in zero-loss mode with a slit width of 20 eV. Automated data collection was carried out using Leginon[56] at a nominal magnification of 105,000 with a pixel size of 0.835 Å and total exposure dose of 58 e/A^2. 13,767 micrographs from UltrAuFoil[57] grids and 13,733 micrographs from chameleon grids were collected with a defocus range between -0.2 and -3.0 μm. Each movie was fractionated in 100 frames of 40 ms each.

Cryo-EM grids of 1.5 μM PDCoV S SD2018/300 complexed with 4.5 μM of PD41 Fab for 1 hour at 4°C were added to glow discharged 300 1.2/1.3 grids. The grids were blotted with a blot force

of -1, 6 second blot time and 10 second wait time before plunge freezing using a vitrobot MarkIV (ThermoFisher Scientific) set at 100% humidity and 4 °C. Data were acquired using an FEI Titan Krios transmission electron microscope operated at 300 kV and equipped with a Gatan K3 direct detector and Gatan Quantum GIF energy filter operated in zero-loss mode with a slit width of 20 eV. Automated data collection was carried out using SerialEM[58] at a nominal magnification of 105,000 with a pixel size of 0.835 Å in defocus range between -1.8 to -0.8 μm. Total exposure dose of 44.5 e/A^2. Each movie was fractionated in 79 frames of 40 ms each. A total of 19,556 micrographs were collected.

Cryo-EM data processing, model building and refinement

The raw movie data of PDCoV RBD complexed with PD33 Fab and anti-human kappa light chain nanobody were processed using motion correction, contrast-transfer function (CTF) parameter estimation, automatic particle picking, and extraction using Warp[45]. Particles were extracted with a box size of 168 pixels with a pixel size of 1.67Å. After two rounds of 2D classification using cryoSPARC[46], well-defined particles were selected and particles from each dataset were combined. Initial models were generated with ab-initio reconstruction in cryoSPARC. The initial models were used as references for a heterogenous refinement. The Topaz models were trained on a Warp particle set which did not yield a high-resolution reconstruction. The particles picked using Topaz were extracted and particles were subjected to 2D-classification, ab-initio reconstruction and heterogenous 3D refinement in cryoSPARC. Particle picking with Topaz improved the number of unique 2D views. The two different particle sets from the Warp and Topaz strategies were merged and duplicates were removed. After two rounds of 3D heterogeneous refinements and removal of junk particles, 3D refinements were carried out using non-uniform refinement. Particle data sets transfer between RELION and cryoSPARC was performed by the pyem program package[47]. Selected particle images were subjected to the Bayesian polishing procedure implemented in RELION[48]. To further improve the density of the PD33 Fab and RBD, the resulting particle sets were subjected to cryoSPARC 2D-classification, ab-initio reconstruction and 3D heterogeneous refinement. Particles belonging to classes with the best resolved PD33 Fab and RBD density were selected and subjected to final 3D non-uniform refinement using cryoSPARC to yield the final reconstruction at 2.9 Å resolution constituting 564,616 particles.

PDCoV SD2018/300 with PD41 Fab data was processed using RELION motion correction, contrast-transfer function (CTF) parameter estimation, particle picking, and extraction using cryoSPARC. Particle images were extracted with a box size of 512 downsampled to 256 pixels and a pixel size of 0.828Å (longest axis for S with Fab is 206 Å). After two rounds of 2D classification using cryoSPARC, well-defined 465,175 particles were selected and processed through non-uniform refinement (NUR). Particles were separated into different 3D classes using 3D classification in RELION with 50 iterations (angular sampling of 7.5 angular sampling 7.5˚for 25 iterations and 1.8˚ with local search for 25 iterations). Particles were grouped into four 3D

classes; Class I) apo II) one RBD bound to PD41 III) two RBDs bound to PD41 and IV) three RBDs bound to PD41. Class I, II, IV particles individually were imported into cryoSPARC and refined using NUR in cryoSPARC. Imported particles from class I, II, III, IV were combined for solving a higher resolution structure of the RBD:PD41 and subjected to NUR in cryoSPARC. Local refinement was performed with a mask around the RBD: PD41 region generated from a volume with a threshold of 0.01 and soft padding width of 17 pixels.

Reported resolutions are based on the gold-standard Fourier shell correlation (FSC) of 0.143 criterion. Local resolution estimation, filtering, and sharpening were carried out using cryoSPARC. The resulting map showed clear density for the overall quaternary architecture and side chains of the interface of PDCoV RBD and PD33 Fab complex. Chimera, ChimeraX and Coot were used to fit atomic models into the cryo-EM maps[49-51]. Structure was refined and relaxed using Rosetta using sharpened and unsharpened maps and validated using Phenix and Molprobity[52-53]. Analysis of interface residues was assisted by PISA.

Constructs and sequences of PDCoV Spike, RBD and APN receptor

A.

Recombinant DNA	Plasmid	Source	NCBI/Genebank ID	Tag
PDCoV RBD USA_IL121_2014	pcDNA3.1 (+)	This study	KJ481931.1	AVI-His
PDCoV RBD HKU15 SD2018_300			MN200481.1	AVI-His
PDCoV RBD HKD_JPN_2016			LC260045.1	AVI-His
PDCoV RBD 110_1197_TW			MZ712033.1	AVI-His
PDCoV RBD Thai_S5011_2015			KU051641.1	AVI-His
PDCoV Spike Full length USA_IL121_2014			KJ481931.1	Flag
PDCoV Spike Full length with RBD mutations from SD2018_300			MN200481.1	Flag
PDCoV Spike Full length with RBD mutations from HKD_JPN_2016			LC260045.1	Flag

PDCoV Spike Full length with RBD mutations from 110_1197_TW			MZ712033.1	Flag
PDCoV Spike Full length with RBD mutations from Thai_S5011_2015			KU051641.1	Flag
PDCoV Spike Haiti_2022 with two consenus mutations amongst three strains P38L V550A			MW685623	Flag
PDCoV Spike Ectodomain IL121_2014 Foldon			KJ481931.1	AVI-His
PDCoV Spike Ectodomain SD2018_300 Foldon			MN200481.1	AVI-His
galline APN full length			ACZ95799.1	Flag
galline APN ecto			ACZ95799.1	Fc
human APN full length			NP_001141.2	Flag
human APN ecto			NP_001141.2	Fc

B

Recombinant DNA	**RBD Mutations Relative to IL121_2014**
PDCoV RBD USA_IL121_2014	N/A
PDCoV RBD HKU15 SD2018_300	M354I, I391V, N397K
PDCoV RBD HKD_JPN_2016	V326I, R342K

PDCoV RBD 110_1197_TW	V326I, T338S
PDCoV RBD Thai_S5011_2015	M349L, T351R

Table 4.10.1. Table of the sequence information of PDCoV S variants as full length, ectodomain and RBD along with hAPN and gAPN sequences as full length and ectodomain constructs. A, List of PDCoV variants used in the study and the genebank ID associated for those variants. The table includes information for the APN constructs used in the study and the genebank ID corresponding to those constructs. **B,** List of the PDCoV variants tested in the study and the RBD mutations found in these variants relative to $PDCoV_{IL121\_2014}$.

Chapter 4: Development of a vaccine for the emerging delta-coronaviruses

4.1. Abstract

There are currently no vaccines for PDCoV. Efforts to make such a vaccine entail selecting the right antigen to immunize. The S glycoprotein and specifically the RBD is the main target of neutralizing antibodies, as seen in Chapter 3 where the identified PD33 and PD41 mAbs competed for host receptor binding and neutralized VSV pseudotyped with PDCoV S. While the RBD is antigenic, it is a relatively small protein and if presented by itself low antibody titers are observed. Multivalent display of the RBD using computationally designed self-assembling nanoparticles would circumvent this problem as multiple copies of the RBD would be presented leading to high antibody titers, as observed for the SARS-CoV-2 Skycovione vaccine. In this study, a PDCoV RBD nanoparticle was produced and Balb/c mice were immunized with the vaccine. We observed that PDCoV RBD nanoparticle neutralized VSV pseudotyped with PDCoV S on Hek293T cells transfected with host human APN (hAPN) receptor.

4.2. Introduction

PDCoV is an emerging enteric virus with no approved vaccines. The virus primarily infects porcine causes gastrointestinal illness and death in piglets. In 2022, the virus infected children in Haiti. The SARS-CoV 2 pandemic taught the world a valuable lesson in underestimating the damage and challenge of neutralizing and protecting animal and human health from coronaviruses. Since the pandemic a plethora of vaccines against SARS-CoV 2 were brought forth all using the spike glycoprotein as the major immunogen. While the spike protein is the major target of neutralizing antibodies from this pool of antibodies, the majority are targeting the RBD. However, small molecular size antigens are not sufficient in eliciting a robust immune response. A multivalent nanoparticle displaying 60 copies of the small RBD antigen was shown to elicit high antibody titers for SARS-CoV-2 and provided protection. In this study, the PDCoV RBD shown to be the target of neutralizing antibodies in Chapter 3 was fused to a using the computationally designed I53-50A component from the King Lab at the University of Washington was assessed as a countermeasure against PDCoV. The two components RBD-I53-50A and I53-50B were mixed and purified using size exclusion chromatography to yield an icosahedral nanoparticle displaying 60 copies of the RBD (Figure 4.2.1.). Negative stain electron microscopy and dynamic light scattering (DLS) were used to assess the integrity of the nanoparticles formed. The PDCoV RBD nanoparticles were analyzed for binding to the host APN receptor using enzyme-linked immunosorbent assay (ELISA).

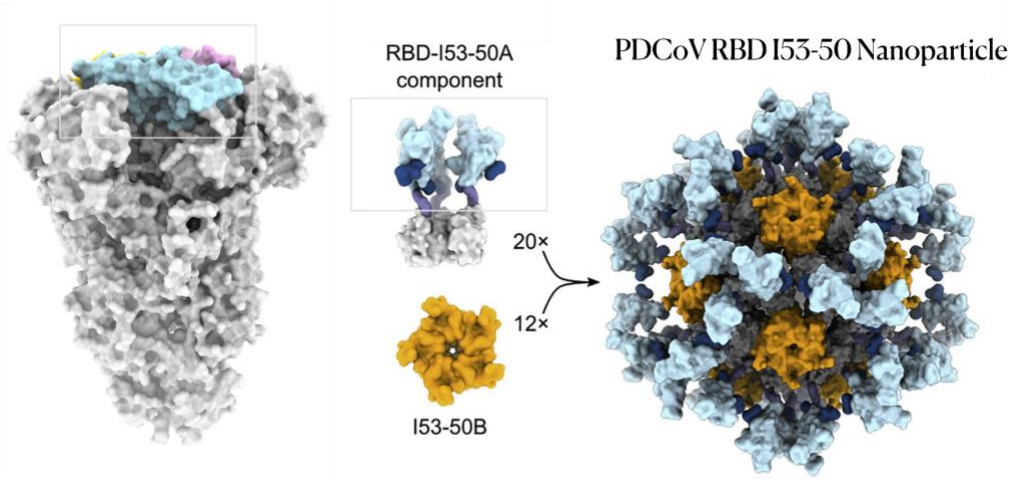

Figure 4.2.1. Schematic overview of the design and assembly of the PDCoV RBD-nanoparticle.

To evaluate the immunogenicity of the PDCoV RBD nanoparticle a vaccine study was initiated where BALB/c mice were immunized twice with three groups 1) PDCoV RBD 2) PDCoV S glycoprotein 3) PDCoV RBD-nanoparticle I53A-B. Sera was analyzed for neutralization of VSV pseudotyped with PDCoV S using HEK293-T target cells transiently transfected with gAPN.

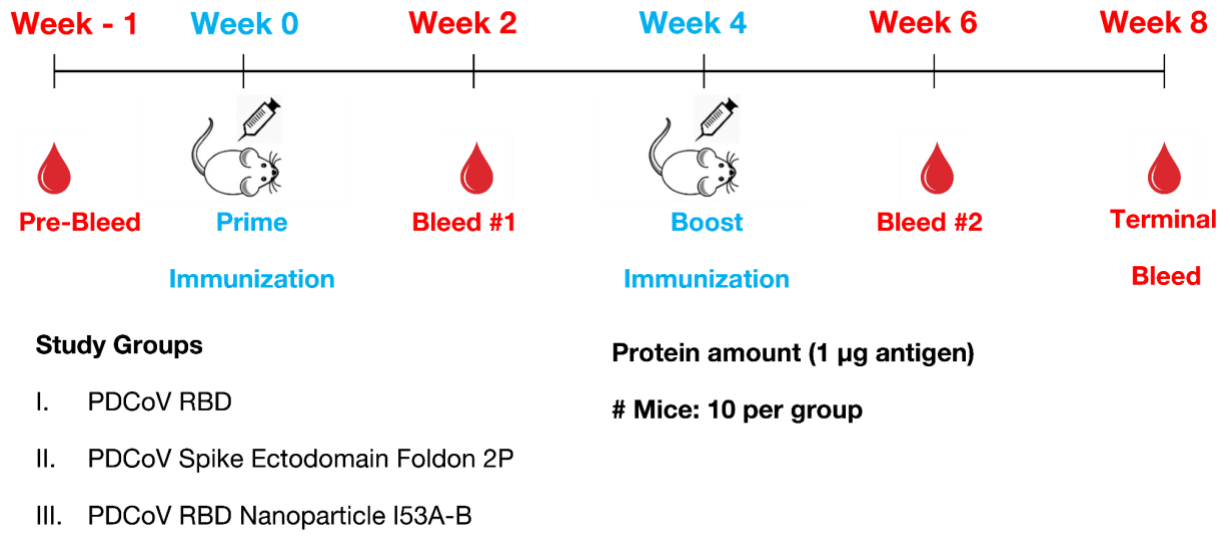

Figure 4.1.2. Vaccine study plan for PDCoV.

4.3. Generation of a delta-coronavirus nanoparticle vaccine

PDCoV RBD, S glycoprotein, and the RBD nanoparticle were successfully purified and characterized. The RBD nanoparticle was well assembled with a monodisperse peak observed using DLS and single particles in a non-aggregated state were seen using negative stain-EM

(Figure 4.3.1B-E). The RBD nanoparticle bound to gAPN-Fc and outcompeted the RBD antigen alone as observed using ELISA (Figure 4.3.1A).

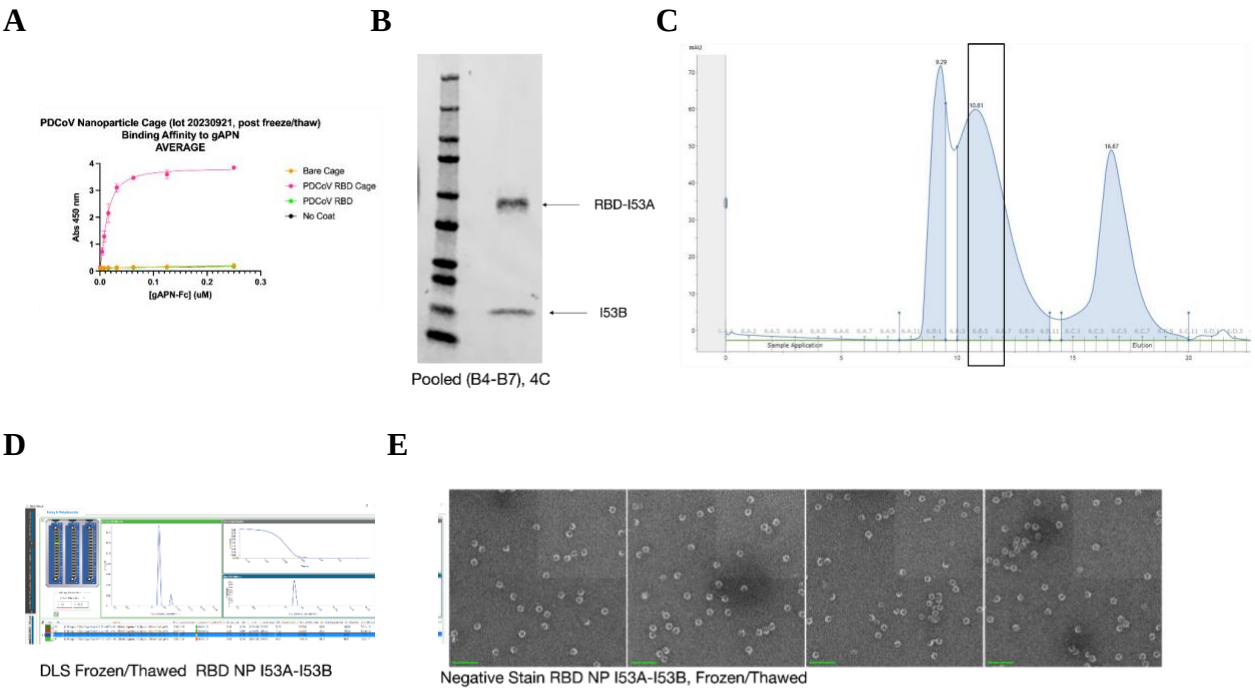

Figure 4.3.1. Characterization of PDCoV RBD nanoparticle. **A,** ELISA of PDCoV RBD, nanoparticle top left. **B,** SDS-PAGE gel showing expression and purification of the two-component system (middle). **C,** Size exclusion chromatography (SEC) UV trace for PDCoV RBD nanoparticle with the final fractions pooled boxed (top right). **D,** DLS profile for PDCoV RBD nanoparticle (bottom left). **E,** Negative stain EM images of the nanoparticles (bottom right).

4.4. Neutralization of viral entry through a delta-coronavirus nanoparticle vaccine

The sera from mice immunized with PDCoV RBD nanoparticle vaccine was tested for the ability to neutralize VSV pseudotyped with PDCoV S on Hek293-T cells transfected with hAPN. We observed that the pre-bleed group showed limited neutralization capability as this is the control prior to vaccination. Bleed 1 post immunization with one round of PDCoV RBD nanoparticle vaccine showed neutralizing activity. Bleed 2 and terminal bleed groups neutralized with a higher potency than bleed 1 (Figure 4.4.1).

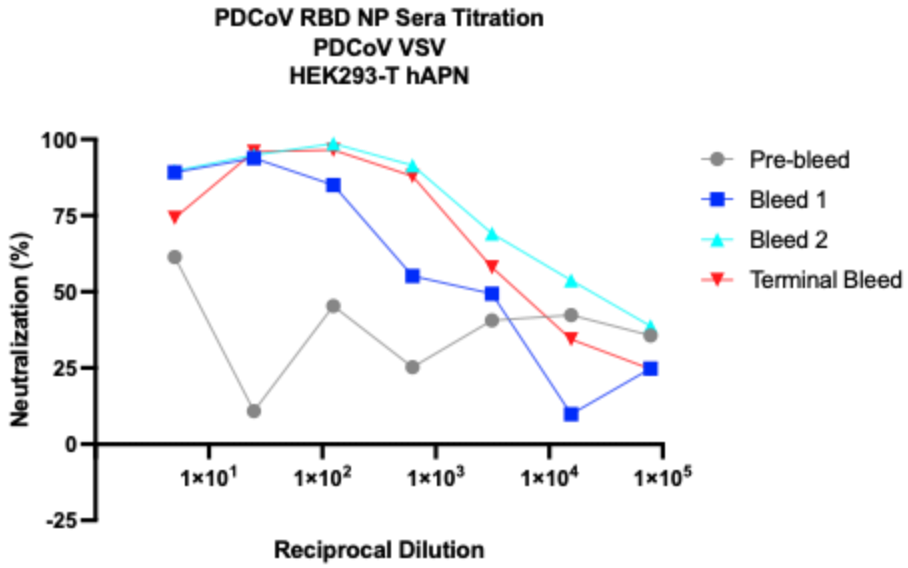

Figure 4.4.1. Neutralization of VSV-PDCoV S by PDCoV RBD nanoparticle. Neutralization of PDCoV VSV on Hek293-T cells transfected with hAPN with Pre-bleed, Bleed 1, 2 and terminal bleed of mice immunized with PDCoV RBD nanoparticle.

4.5. Discussion

A computationally designed nanoparticle displaying 60 copies of the RBD from PDCoV S glycoprotein was generated and tested for the ability to neutralize VSV pseudotyped with PDCoV S. The PDCoV RBD nanoparticle was able to bind to host APN and neutralize PDCoV VSV on Hek293-T cells transfected with hAPN. A two-dose regimen appeared to elicit higher titers as evidenced by a higher IC50 for bleed 2 vs bleed 1. The levels of antibodies in the two groups would need to be measured to confirm this hypothesis. Furthermore, it is not unknown whether the PDCoV RBD nanoparticle outcompetes immunogenicity observed with RBD and PDCoV S antigens. Neutralization potency may likely, would be higher due to higher antibody titers thereby producing an overall stronger and desired immune response with the PDCoV RBD nanoparticle.

4.6. Methods

Production of recombinant PDCoV S glycoprotein

The $PDCoV_{IL121\_2014}$ S glycoprotein ectodomain (Genbank KJ481931.1) were cloned into pcDNA3.1+ plasmid by GenScript with the host N-terminal signal peptide sequence, C-terminal foldon domain, thrombin cleavage sequence, short linker of GSG, AVI tag and 8 x His tag. The DNA constructs were expanded using DH5α cells and purified using Qiagen MegaPrep Kit. Protein was expressed using ExpiFectamine 293 Transfection Kit (Thermo Fisher Scientific). Expi293F cells were grown at 37℃ with 8% CO_2 to 3E6 cells and transfected with 100µg of DNA. Cell culture supernatants were harvested four days post-transfection. Protein was purified using HisTrap^{Tm} High Performance column (Cytiva). Protein was bound to HisTrap resin in 50mM Tris-HCl, 150mM NaCl, 10mM Imidazole at pH 8.0. Unbound proteins were washed in 10 column volumes of 50mM Tris-HCl, 150mM NaCl, 10mM Imidazole at pH 8.0. Eluted with 50mM Tris, 150mM NaCl, 250 mM Imidazole at pH 8.0. The eluted S protein was concentrated using Amicon Ultra-15 Centrifugal Filter Unit (100kDa) and buffer exchanged into 50mM Tris, 150mM NaCl pH 8.0. Endotoxin levels were assessed using Charles River Limulus Amebocyte Lysate (LAL) cartridges. Proteins were snap frozen in liquid nitrogen and stored at -80℃.

Production of recombinant PDCoV RBD

The $PDCoV_{IL121\_2014}$ RBD (Genbank KJ481931.1) spanning residues 303-415 were cloned into pcDNA3.1+ plasmid by GenScript with an N-terminal mu-phosphatase signal peptide sequence and C-terminal short linker GSG, AVI tag and 8 x His tag. The DNA constructs were expanded using DH5α cells and purified using Qiagen MegaPrep Kit. Protein was expressed using ExpiFectamine 293 Transfection Kit (Thermo Fisher Scientific). Expi293F cells were grown at 37℃ with 8% CO_2 to 3E6 cells and transfected with 100 µg of DNA. Cell culture supernatants were harvested four days post-transfection. Protein was purified using HisTrap^{Tm} High Performance column (Cytiva). Protein was bound to HisTrap resin in 50mM Tris-HCl, 150mM NaCl, 10mM Imidazole at pH 8.0. Unbound proteins were washed in 10 column volumes of 50mM Tris-HCl, 150mM NaCl, 10mM Imidazole at pH 8.0. Eluted with 50mM Tris-HCl, 150mM NaCl, 250 mM Imidazole at pH 8.0. The eluted RBD was concentrated using Amicon Ultra-15 Centrifugal Filter Unit (10 kDa) and buffer exchanged into 50mM Tris, 150mM NaCl pH 8.0 and further purified using size exclusion chromatography Superdex 200 10/300. Endotoxin levels were assessed using Charles River Limulus Amebocyte Lysate (LAL) cartridges. Proteins were snap frozen in liquid nitrogen and stored at -80℃.

Production of PDCoV RBD nanoparticle

100ml of expi293 cells at 3E6 cell P19 cells at 95% viability were transfected with 100 ug of DNA. 320 ul of transfection reagent 6 ml of optimem were mixed for 5 minutes at romm temp. 6 ml of optimum and 100 ug of DNA were mixed for 5 minutes at room temp. Transfection mixture and DNA were mixed for 15 minutes at room temp and added drop wise to 3E6 cells. Next day enhancer mixture of 1 and 2 were added at a ratio of 6ml to 600ul for 100ml of cells. 4 days post enhancer addition the cells were harvested (D0 transfection, D1 enhancer, D4 harvest). Cells were harvested and 25 ml of 5x binding buffer to cells dropwise. Cells were centrifuge at 3500 rpm for 20 minutes at 4 C. Supernatant was collected and filtered using .25-micron disposable filter. PDCoV RBD-I53A component was run through His HisTrap Excel Cytivia 1ml column. Purified using a gradient of imidazole from 10-500mM. Fractions were pooled and concentrated at 2500 rpm 10 minutes at 4 C using a 10Kda concentrator. Protein was filtered using .25 micron filter then loaded on size Exclusion Column (superose 6 column) at .3ml/min. Post SEC fractions were pooled and concentrated to 50uM at 2500 rpm 10 minutes at 4 C using a 10Kda concentrator. The PDCoV RBD-I53A component was mixed with 55uM of component B and incubated at room temperature for 30 minutes with gentle spin. The mixture was loaded onto S6 column.

Production of VSV pseudoviruses

PDCoV S glycoprotein constructs containing a C-terminal deletion of 21 residues to improve exportation to the membrane followed by a Flag tag were cloned into pcDNA3.1+ by GenScript. HEK293T cells were seeded at 16E6 cells in 100 mm dishes (Corning) poly-D-Lysine coated. Cells were transfected with 24 μg of DNA and 60 μL of Lipofectamine 2000 (Thermo Fisher Scientific) in Opti-MEM transfection medium. Post 5 hour incubation DMEM containing 20% FBS and 2% PenStrep was added to the cells. After 21 hours at 37 °C with 5% CO_2 the cells are washed 1x with DMEM and infected with VSV (G∗ΔG-luciferase) in DMEM for 2 hours. The cells are washed 2x with DMEM and anti-VSV G antibody (I1-mouse hybridoma supernatant diluted 1:40 in DMEM, ATCC CRL-2700) is added and incubated for 24 hours at 37 °C with 5% CO_2. Pseudovirus is harvested and collected by centrifugation at 3,000xg for 10 min. Supernatant containing the pseudovirus is filtered using a 0.45 μm syringe filter and concentrated 5x prior to storage at -80°C. Mock VSV pseudoviruses were prepared as above but without S glycoprotein transfection.

Cell entry assays

HEK293T cells were transiently transfected with human APN (hAPN). hAPN with a C-terminal Flag tag was cloned into pcDNA3.1+ by GenScript. HEK293T cells seeded at 16E6 cells in 100 mm dishes coated with poly-D-Lysine and incubated overnight at 37 °C with 5% CO_2. The following day cells were transfected with 8 μg of DNA using 30 μL of Lipofectamine 2000 transfection kit in Opti-MEM. Post 5 hours of incubation with transfection reagent, cells were trypsinized with 0.05% Trypsin EDTA for 3 minutes and neutralized with DMEM with 10% FBS

1% penicillin–streptomycin. 40,000 cells were seeded in 96-well plates (Corning 3610) coated with poly-lysine (Sigma P4707) and allowed to incubate at 37 °C with 5% CO_2. Following day, media was removed and 20 μL of DMEM was added followed by 20 μL of VSV pseudotyped with PDCoV S variants for 2 hours at 37 °C with 5% CO_2. Cells were supplemented with 40 μL of DMEM containing 20% FBS and 2% PenStrep and incubated for 22 hours at 37 °C with 5% CO_2. 40 μL of One-Glo-EX substrate (Promega) was added and cells were incubated at 37 °C for 10 minutes with shaking. Luminescence was read using BioTek Neo2 plate reader. Technical replicates of three were run for three different lots of pseudovirus for each variant. Luciferase units were plotted using Graphpad Prism.

Neutralization assays

HEK293T cells were transfected with hAPN as described in the cell entry assay. 40,000 cells/well were seeded into 96-well plates coated with poly-lysine and incubated overnight at 37°C. Sera titration series was performed in a half-area 96-well plate (Greiner) starting at a 1/10 dilution preceded by 1:4 dilution. Equal volume of pseudovirus was added and incubated at room temperature for 30 minutes and 40 μL was transferred to cells and incubated for 2 hours at 37 °C with 5% CO_2. Cells were supplemented with 40 μL of DMEM with 20% FBS and 2% PenStrep and incubated for 22 hours at 37 °C with 5% CO_2. After 22 hrs, 40 μL of One-Glo-EX substrate (Promega) was added to each well and incubated on a plate shaker in the dark for 5 min before reading the relative luciferase units using a BioTek Neo2 plate reader. Relative luciferase units were used to determine (%) neutralization in Prism (GraphPad). Nonlinear regression curve fit and sigmoidal 4PL where x is the concentration was run to determine IC50 values for 3 biological replicates of pseudovirus and three technical replicates for each titration series.

References

1. Hamre, D., and Procknow, J.J. (1966). A new virus isolated from the human respiratory tract. Proc. Soc. Exp. Biol. Med. *121*, 190–193.

2. van der Hoek, L., Pyrc, K., Jebbink, M.F., Vermeulen-Oost, W., Berkhout, R.J.M., Wolthers, K.C., Wertheim-van Dillen, P.M.E., Kaandorp, J., Spaargaren, J., and Berkhout, B. (2004). Identification of a new human coronavirus. Nat. Med. *10*, 368–373.

3. Woo, P.C.Y., Lau, S.K.P., Chu, C.-M., Chan, K.-H., Tsoi, H.-W., Huang, Y., Wong, B.H.L., Poon, R.W.S., Cai, J.J., Luk, W.-K., et al. (2005). Characterization and complete genome sequence of a novel coronavirus, coronavirus HKU1, from patients with pneumonia. J. Virol. *79*, 884–895.

4. Vijgen, L., Keyaerts, E., Moes, E., Thoelen, I., Wollants, E., Lemey, P., Vandamme, A.M., and Van Ranst, M. (2005). Complete genomic sequence of human coronavirus OC43: molecular clock analysis suggests a relatively recent zoonotic coronavirus transmission event. J. Virol. *79*, 1595–1604.

5. Drosten, C., Gunther, S., Preiser, W., van der Werf, S., Brodt, H.R., Becker, S., Rabenau, H., Panning, M., Kolesnikova, L., Fouchier, R.A., et al. (2003). Identification of a novel coronavirus in patients with severe acute respiratory syndrome. N. Engl. J. Med. *348*, 1967–1976.

6. Marra, M.A., Jones, S.J.M., Astell, C.R., Holt, R.A., Brooks-Wilson, A., Butterfield, Y.S.N., Khattra, J., Asano, J.K., Barber, S.A., Chan, S.Y., et al. (2003). The Genome sequence of the SARS-associated coronavirus. Science *300*, 1399–1404.

7. Rota, P.A., Oberste, M.S., Monroe, S.S., Nix, W.A., Campagnoli, R., Icenogle, J.P., Peñaranda, S., Bankamp, B., Maher, K., Chen, M.-H., et al. (2003). Characterization of a novel coronavirus associated with severe acute respiratory syndrome. Science *300*, 1394–1399.

8. Ksiazek, T.G., Erdman, D., Goldsmith, C.S., Zaki, S.R., Peret, T., Emery, S., Tong, S., Urbani, C., Comer, J.A., Lim, W., et al. (2003). A novel coronavirus associated with severe acute respiratory syndrome. N. Engl. J. Med. *348*, 1953–1966.

9. Zaki, A.M., van Boheemen, S., Bestebroer, T.M., Osterhaus, A.D., and Fouchier, R.A. (2012). Isolation of a novel coronavirus from a man with pneumonia in Saudi Arabia. N. Engl. J. Med. *367*, 1814–1820.

10. Zhou, P., Yang, X.L., Wang, X.G., Hu, B., Zhang, L., Zhang, W., Si, H.R., Zhu, Y., Li, B., Huang, C.L., et al. (2020). A pneumonia outbreak associated with a new coronavirus of probable bat origin. Nature. 10.1038/s41586-020-2012-7.

11. Zhu, N., Zhang, D., Wang, W., Li, X., Yang, B., Song, J., Zhao, X., Huang, B., Shi, W., Lu, R., et al. (2020). A Novel Coronavirus from Patients with Pneumonia in China, 2019. N. Engl. J. Med. 10.1056/NEJMoa2001017.

12. Vlasova, A.N., Diaz, A., Damtie, D., Xiu, L., Toh, T.-H., Lee, J.S.-Y., Saif, L.J., and Gray,

G.C. (2021). Novel Canine Coronavirus Isolated from a Hospitalized Pneumonia Patient, East Malaysia. Clin. Infect. Dis. 10.1093/cid/ciab456.

13. Tortorici, M.A., Walls, A.C., Joshi, A., Park, Y.-J., Eguia, R.T., Miranda, M.C., Kepl, E., Dosey, A., Stevens-Ayers, T., Boeckh, M.J., et al. (2022). Structure, receptor recognition, and antigenicity of the human coronavirus CCoV-HuPn-2018 spike glycoprotein. Cell *185*, 2279–2291.e17.

14. Lednicky, J.A., Tagliamonte, M.S., White, S.K., Blohm, G.M., Alam, M.M., Iovine, N.M., Salemi, M., Mavian, C., and Morris, J.G. (2021). Isolation of a novel recombinant canine Coronavirus from a visitor to Haiti: Further evidence of transmission of coronaviruses of zoonotic origin to humans. Clin. Infect. Dis. 10.1093/cid/ciab924.

15. Li, W., Hulswit, R.J.G., Kenney, S.P., Widjaja, I., Jung, K., Alhamo, M.A., van Dieren, B., van Kuppeveld, F.J.M., Saif, L.J., and Bosch, B.J. (2018). Broad receptor engagement of an emerging global coronavirus may potentiate its diverse cross-species transmissibility. Proc. Natl. Acad. Sci. U. S. A. *115*, E5135–E5143.

16. Lednicky, J.A., Tagliamonte, M.S., White, S.K., Elbadry, M.A., Alam, M.M., Stephenson, C.J., Bonny, T.S., Loeb, J.C., Telisma, T., Chavannes, S., et al. (2021). Independent infections of porcine deltacoronavirus among Haitian children. Nature *600*, 133–137.

17. Walls, A.C., Tortorici, M.A., Snijder, J., Xiong, X., Bosch, B.J., Rey, F.A., and Veesler, D. (2017). Tectonic conformational changes of a coronavirus spike glycoprotein promote membrane fusion. Proc. Natl. Acad. Sci. U. S. A. *114*, 11157–11162.

18. Walls, A.C., Tortorici, M.A., Bosch, B.J., Frenz, B., Rottier, P.J.M., DiMaio, F., Rey, F.A., and Veesler, D. (2016). Cryo-electron microscopy structure of a coronavirus spike glycoprotein trimer. Nature *531*, 114–117.

19. Tortorici, M.A., and Veesler, D. (2019). Structural insights into coronavirus entry. Adv. Virus Res. *105*, 93–116.

20. Walls, A.C., Park, Y.-J., Tortorici, M.A., Wall, A., McGuire, A.T., and Veesler, D. (2020). Structure, Function, and Antigenicity of the SARS-CoV-2 Spike Glycoprotein. Cell *181*, 281–292.e6.

21. Menachery, V.D., Yount, B.L., Jr., Sims, A.C., Debbink, K., Agnihothram, S.S., Gralinski, L.E., Graham, R.L., Scobey, T., Plante, J.A., Royal, S. R., et al. (2016). SARS-like WIV1-CoV poised for human emergence. Proc. Natl. Acad. Sci. U. S. A. *113*, 3048–3053.

22. Menachery, V.D., Yount, B.L., Jr., Debbink, K., Agnihothram, S., Gralinski, L.E., Plante, J.A., Graham, R.L., Scobey, T., Ge, X.Y., Donaldson, E.F., et al. (2015). A SARS-like cluster of circulating bat coronaviruses shows potential for human emergence. Nat. Med. *21*, 1508–1513.

23. Johnson, B.A., Xie, X., Bailey, A.L., Kalveram, B., Lokugamage, K.G., Muruato, A., Zou, J., Zhang, X., Juelich, T., Smith, J.K., et al. (2021). Loss of furin cleavage site attenuates SARS-CoV-2 pathogenesis. Nature *591*, 293–299.

24. Arunachalam, P.S., Walls, A.C., Golden, N., Atyeo, C., Fischinger, S., Li, C., Aye, P., Navarro, M.J., Lai, L., Edara, V.V., et al. (2021). Adjuvanting a subunit COVID-19 vaccine to induce protective immunity. Nature. 10.1038/s41586-021-03530-2.

25. Corbett, K.S., Nason, M.C., Flach, B., Gagne, M., O'Connell, S., Johnston, T.S., Shah, S.N., Edara, V.V., Floyd, K., Lai, L., et al. (2021). Immune correlates of protection by mRNA-1273 vaccine against SARS-CoV-2 in nonhuman primates. Science. 10.1126/science.abj0299.

26. Piccoli, L., Park, Y.J., Tortorici, M.A., Czudnochowski, N., Walls, A.C., Beltramello, M., Silacci-Fregni, C., Pinto, D., Rosen, L.E., Bowen, J.E., et al. (2020). Mapping Neutralizing and Immunodominant Sites on the SARS-CoV-2 Spike Receptor-Binding Domain by Structure-Guided High-Resolution Serology. Cell *183*, 1024–1042.e21.

27. McCallum, M., De Marco, A., Lempp, F.A., Tortorici, M.A., Pinto, D., Walls, A.C., Beltramello, M., Chen, A., Liu, Z., Zatta, F., et al. (2021). N-terminal domain antigenic mapping reveals a site of vulnerability for SARS-CoV-2. Cell *184*, 2332–2347.e16.

28. Barnes, C.O., West, A.P., Jr, Huey-Tubman, K.E., Hoffmann, M.A.G., Sharaf, N.G., Hoffman, P.R., Koranda, N., Gristick, H.B., Gaebler, C., Muecksch, F., et al. (2020). Structures of Human Antibodies Bound to SARS-CoV-2 Spike Reveal Common Epitopes and Recurrent Features of Antibodies. Cell *182*, 828–842.e16.

29. Ereño-Orbea, J., Sicard, T., Cui, H., Carson, J., Hermans, P., and Julien, J.-P. (2018). Structural Basis of Enhanced Crystallizability Induced by a Molecular Chaperone for Antibody Antigen-Binding Fragments. J. Mol. Biol. *430*, 322–336.

30. Walls, A.C., Xiong, X., Park, Y.J., Tortorici, M.A., Snijder, J., Quispe, J., Cameroni, E., Gopal, R., Dai, M., Lanzavecchia, A., et al. (2019). Unexpected Receptor Functional Mimicry Elucidates Activation of Coronavirus Fusion. Cell *176*, 1026–1039.e15.

31. Starr, T.N., Czudnochowski, N., Liu, Z., Zatta, F., Park, Y.-J., Addetia, A., Pinto, D., Beltramello, M., Hernandez, P., Greaney, A.J., et al. (2021). SARS-CoV-2 RBD antibodies that maximize breadth and resistance to escape. Nature. 10.1038/s41586-021-03807-6.

32. Lempp, F.A., Soriaga, L., Montiel-Ruiz, M., Benigni, F., Noack, J., Park, Y.-J., Bianchi, S., Walls, A.C., Bowen, J.E., Zhou, J., et al. (2021). Lectins enhance SARS-CoV-2 infection and influence neutralizing antibodies. Nature. 10.1038/s41586-021-03925-1.

33. Huo, J., Zhao, Y., Ren, J., Zhou, D., Duyvesteyn, H.M.E., Ginn, H.M., Carrique, L., Malinauskas, T., Ruza, R.R., Shah, P.N.M., et al. (2020). Neutralisation of SARS-CoV-2 by destruction of the prefusion Spike. Cell Host Microbe. 10.1016/j.chom.2020.06.010.

34. Wrobel, A.G., Benton, D.J., Hussain, S., Harvey, R., Martin, S.R., Roustan, C., Rosenthal, P.B., Skehel, J.J., and Gamblin, S.J. (2020). Antibody-mediated disruption of the SARS-CoV-2 spike glycoprotein. Nat. Commun. *11*, 5337.

35. Xiong, X., Tortorici, M.A., Snijder, J., Yoshioka, C., Walls, A.C., Li, W., McGuire, A.T., Rey, F.A., Bosch, B.J., and Veesler, D. (2018). Glycan Shield and Fusion Activation of a

Deltacoronavirus Spike Glycoprotein Fine-Tuned for Enteric Infections. J. Virol. *92*. 10.1128/JVI.01628-17.

36. Addetia, A., Piccoli, L., Case, J.B., Park, Y.-J., Beltramello, M., Guarino, B., Dang, H., de Melo, G.D., Pinto, D., Sprouse, K., et al. (2023). Neutralization, effector function and immune imprinting of Omicron variants. Nature *621*, 592–601.

37. McCallum, M., Walls, A.C., Sprouse, K.R., Bowen, J.E., Rosen, L.E., Dang, H.V., De Marco, A., Franko, N., Tilles, S.W., Logue, J., et al. (2021). Molecular basis of immune evasion by the Delta and Kappa SARS-CoV-2 variants. Science, eabl8506.

38. Starr, T.N., Greaney, A.J., Hilton, S.K., Ellis, D., Crawford, K.H.D., Dingens, A.S., Navarro, M.J., Bowen, J.E., Tortorici, M.A., Walls, A.C., et al. (2020). Deep Mutational Scanning of SARS-CoV-2 Receptor Binding Domain Reveals Constraints on Folding and ACE2 Binding. Cell *182*, 1295–1310.e20.

39. McCallum, M., Czudnochowski, N., Rosen, L.E., Zepeda, S.K., Bowen, J.E., Walls, A.C., Hauser, K., Joshi, A., Stewart, C., Dillen, J.R., et al. (2022). Structural basis of SARS-CoV-2 Omicron immune evasion and receptor engagement. Science, eabn8652.

40. Bowen, J.E., Park, Y.-J., Stewart, C., Brown, J.T., Sharkey, W.K., Walls, A.C., Joshi, A., Sprouse, K.R., McCallum, M., Tortorici, M.A., et al. (2022). SARS-CoV-2 spike conformation determines plasma neutralizing activity elicited by a wide panel of human vaccines. Sci Immunol *7*, eadf1421.

41. Greaney, A.J., Loes, A.N., Gentles, L.E., Crawford, K.H.D., Starr, T.N., Malone, K.D., Chu, H.Y., and Bloom, J.D. (2021). Antibodies elicited by mRNA-1273 vaccination bind more broadly to the receptor binding domain than do those from SARS-CoV-2 infection. Sci. Transl. Med. *13*. 10.1126/scitranslmed.abi9915.

42. Stamatatos, L., Czartoski, J., Wan, Y.-H., Homad, L.J., Rubin, V., Glantz, H., Neradilek, M., Seydoux, E., Jennewein, M.F., MacCamy, A.J., et al. (2021). mRNA vaccination boosts cross-variant neutralizing antibodies elicited by SARS-CoV-2 infection. Science. 10.1126/science.abg9175.

43. Wrapp, D., Wang, N., Corbett, K.S., Goldsmith, J.A., Hsieh, C.L., Abiona, O., Graham, B.S., and McLellan, J.S. (2020). Cryo-EM structure of the 2019-nCoV spike in the prefusion conformation. Science *367*, 1260–1263.

44. Pallesen, J., Wang, N., Corbett, K.S., Wrapp, D., Kirchdoerfer, R.N., Turner, H.L., Cottrell, C.A., Becker, M.M., Wang, L., Shi, W., et al. (2017). Immunogenicity and structures of a rationally designed prefusion MERS-CoV spike antigen. Proc. Natl. Acad. Sci. U. S. A. *114*, E7348–E7357.

45. Yuan, Y., Cao, D., Zhang, Y., Ma, J., Qi, J., Wang, Q., Lu, G., Wu, Y., Yan, J., Shi, Y., et al. (2017). Cryo-EM structures of MERS-CoV and SARS-CoV spike glycoproteins reveal the dynamic receptor binding domains. Nat. Commun. *8*, 15092.

46. Song, W., Gui, M., Wang, X., and Xiang, Y. (2018). Cryo-EM structure of the SARS

coronavirus spike glycoprotein in complex with its host cell receptor ACE2. PLoS Pathog. *14*, e1007236.

47. Kirchdoerfer, R.N., Cottrell, C.A., Wang, N., Pallesen, J., Yassine, H.M., Turner, H.L., Corbett, K.S., Graham, B.S., McLellan, J.S., and Ward, A.B. (2016). Pre-fusion structure of a human coronavirus spike protein. Nature *531*, 118–121.

48. Tortorici, M.A., Walls, A.C., Lang, Y., Wang, C., Li, Z., Koerhuis, D., Boons, G.J., Bosch, B.J., Rey, F.A., de Groot, R.J., et al. (2019). Structural basis for human coronavirus attachment to sialic acid receptors. Nat. Struct. Mol. Biol. *26*, 481–489.

49. Li, Z., Tomlinson, A.C., Wong, A.H., Zhou, D., Desforges, M., Talbot, P.J., Benlekbir, S., Rubinstein, J.L., and Rini, J.M. (2019). The human coronavirus HCoV-229E S-protein structure and receptor binding. Elife *8*. 10.7554/eLife.51230.

50. Wrobel, A.G., Benton, D.J., Xu, P., Calder, L.J., Borg, A., Roustan, C., Martin, S.R., Rosenthal, P.B., Skehel, J.J., and Gamblin, S.J. (2021). Structure and binding properties of Pangolin-CoV spike glycoprotein inform the evolution of SARS-CoV-2. Nat. Commun. *12*, 837.

51. Wrobel, A.G., Benton, D.J., Xu, P., Roustan, C., Martin, S.R., Rosenthal, P.B., Skehel, J.J., and Gamblin, S.J. (2020). SARS-CoV-2 and bat RaTG13 spike glycoprotein structures inform on virus evolution and furin-cleavage effects. Nat. Struct. Mol. Biol. *27*, 763–767.

52. Walls, A.C., Tortorici, M.A., Frenz, B., Snijder, J., Li, W., Rey, F.A., DiMaio, F., Bosch, B.-J., and Veesler, D. (2016). Glycan shield and epitope masking of a coronavirus spike protein observed by cryo-electron microscopy. Nat. Struct. Mol. Biol. *23*, 899–905.

53. Pronker, M.F., Creutznacher, R., Drulyte, I., Hulswit, R.J.G., Li, Z., van Kuppeveld, F.J.M., Snijder, J., Lang, Y., Bosch, B.-J., Boons, G.-J., et al. (2023). Sialoglycan binding triggers spike opening in a human coronavirus. Nature. 10.1038/s41586-023-06599-z.

54. Saunders, N., Fernandez, I., Planchais, C., Michel, V., Rajah, M.M., Baquero Salazar, E., Postal, J., Porrot, F., Guivel-Benhassine, F., Blanc, C., et al. (2023). TMPRSS2 is a functional receptor for human coronavirus HKU1. Nature. 10.1038/s41586-023-06761-7.

55. Wei, H., Kurti, D., Budell, W.C., Dandey, V.P., Potter, C.S., and Carragher, B. (2020). Optimizing Self-wicking Grids for Chameleon. Microsc. Microanal. *26*, 334–335.

56. Suloway, C., Pulokas, J., Fellmann, D., Cheng, A., Guerra, F., Quispe, J., Stagg, S., Potter, C.S., and Carragher, B. (2005). Automated molecular microscopy: the new Leginon system. J. Struct. Biol. *151*, 41–60.

57. Russo, C.J., and Passmore, L.A. (2014). Electron microscopy: Ultrastable gold substrates for electron cryomicroscopy. Science *346*, 1377–1380.

58. Mastronarde, D.N. (2005). Automated electron microscope tomography using robust prediction of specimen movements. J. Struct. Biol. *152*, 36–51.

60. David N Mastronarde, SerialEM: A Program for Automated Tilt Series Acquisition on Tecnai Microscopes Using Prediction of Specimen Position, Microscopy and Microanalysis, Volume 9, Issue S02, 1 August 2003, Pages 1182–1183.

61. D. Tegunov, P. Cramer. Real-time cryo-electron microscopy data preprocessing with Warp. Nat. Methods, 16 (2019), pp. 1146-1152.

62. A. Punjani, J.L. Rubinstein, D.J. Fleet, M.A. Brubaker. cryoSPARC: algorithms for rapid unsupervised cryo-EM structure determination. Nat. Methods, 14 (2017), pp. 290-296.

63. Asarnow, D., Palovcak, E., Cheng, Y. UCSF pyem v0.5. Zenodo https://doi.org/10.5281/zenodo.3576630 (2019).

64. J. Zivanov, T. Nakane, B.O. Forsberg, D. Kimanius, W.J. Hagen, E. Lindahl, S.H. Scheres. New tools for automated high-resolution cryo-EM structure determination in RELION-3.

65. T.D. Goddard, C.C. Huang, E.C. Meng, E.F. Pettersen, G.S. Couch, J.H. Morris, T.E. Ferrin. UCSF ChimeraX: meeting modern challenges in visualization and analysis. Protein Sci., 27 (2018), pp. 14-25.

66. E.F. Pettersen, T.D. Goddard, C.C. Huang, G.S. Couch, D.M. Greenblatt, E.C. Meng, T.E. Ferrin. UCSF Chimera--a visualization system for exploratory research and analysis. J. Comput. Chem., 25 (2004), pp. 1605-1612.

67. D. Liebschner, P.V. Afonine, M.L. Baker, G. Bunkóczi, V.B. Chen, T.I. Croll, B. Hintze, L.W. Hung, S. Jain, A.J. McCoy, et al. Macromolecular structure determination using X-rays, neutrons and electrons: recent developments in Phenix. Acta Crystallogr. D Struct. Biol., 75 (2019), pp. 861-877.

68. P. Emsley, B. Lohkamp, W.G. Scott, K. Cowtan. Features and development of coot. Acta Crystallogr. D Biol. Crystallogr., 66 (2010), pp. 486-501.

69. V.B. Chen, W.B. Arendall, J.J. Headd, D.A. Keedy, R.M. Immormino, G.J. Kapral, L.W. Murray, J.S. Richardson, D.C. Richardson. MolProbity: all-atom structure validation for macromolecular crystallography. Acta Crystallogr. D Biol. Crystallogr., 66 (2010), pp. 12-21.